SIZE AND NITROGEN CATALYTIC EFFECTS ON THE MAGNETIC PROPERTIES OF FE THHIN FILMS

ZHONG WEI HUA

SCHOOL OF ELECTRICAL & ELECTRONIC ENGINEERING NANGYANG
TECHNOLOGICAL UNIVERSITY

2005

Size and Nitrogen Catalytic Effects On the Magnetic Properties of Fe Thin Films

Zhong Wei Hua

School of Electrical & Electronic Engineering

A thesis submitted to the Nanyang Technological University
in fulfillment of the requirement for the degree of
Doctor of Philosophy

2005

Acknowledgments

First of all, I would like to express my deepest gratitude to my supervisor, Prof. Sun Chang Qing, for his patient guidance, encouragement, and advice throughout this study, and especially his detailed instructions and comments through all the articles and thesis writing during the last three years.

I am also grateful to Prof. Li Suixiang, Sean for the ExtMagLab characterization, Prof. Ding Jun of the National University of Singapore for allowing me to use the VSM system, and Mr. Chen Qun for his training and instruction in regard to the VSM system. I am also grateful for the help from Dr. Fu Yong Qing with the XPS characterization, and from Mr. Kappaganthu Sri Ramakanth with the SEM characterization. My discussions with them were much appreciated.

I would like to express my sincere thanks to Prof. Tay Beng Kang, Prof. Lau Shu Ping, Daniel, and Prof. Sun Xiao Wei at the Ion Beam Processing Lab for their kind assistance, encouragement, and instruction – especially their financial assistance in regard to the magnetic characterization.

I would like to thank all of the staff and students at the Ion Beam Processing Lab, especially Dr. Yu Guo Qing, Dr. Zhang Yue Bin, Dr. Gan Zhen Hao, Mr. Yu Liujiang, Mr. Li Junfeng, Mr. Pan Li Kun, Miss Sze Jia Yin, and Miss Zhao Zhi Wei, for their encouragement, inspirational discussions, and all the different kinds of assistance they gave me.

Finally, I wish to take this opportunity to express my profound gratitude to my beloved parents, and my younger brother for their moral support and patience during my studies at NTU.

Dedicated to my beloved family: my parents, Zhong Jinlong and Yuan Guanxiu, and my younger brother, Zhong Weiwen.

Summary

The effects of physical size reduction and catalytic nitridation on the ferromagnetic behavior of Fe films were investigated using three approaches: (i) a theoretical study was conducted that involved incorporating the bond-order-length-strength (BOLS) and bond-band-barrier (BBB) correlations [C. Q. Sun, Prog. Mater. Sci. 48(6), 521 (2003)] in the Ising model premise and Brillouin functions to predict the magnetic performance at different temperatures; (ii) Monte Carlo simulations were carried out on the spin system with various cluster sizes and geometric shapes to verify the BOLS predictions; and (iii) nickel, iron, and iron nitride films were deposited using the filtered cathodic vacuum arc technique and were characterized to confirm the predictions and Monte Carlo simulations.

It was found that when a solid (particle or film) forms at a nanometer scale, the effect of atomic coordination number (CN) imperfection and the following effect on the bond-length-strength dominate, which localize the charges that contribute to the angular momentum (J) and hence the magnetic moment (μ) of the system. The CN imperfection also affects the atomic cohesion, or the spin-spin exchange interaction, of the lower-coordinated atoms, which determine the phase stability, or Curie temperature (T_C) suppression. The competition between charge localization and atomic cohesive energy reduction determines the magnetic behavior of a nanosolid at various temperatures. The coercivity (H_C), however, increases with the increase of size due to the rise of intergrain interaction. Understanding of the size-induced phase stability was extended to

the ferroelectric and superconductive nanosolid with consideration of the high-order exchange interaction.

It was also found that nitrogen addition affects the μ of an iron atom by changing its valence states from Fe to $\mathrm{Fe}^{\mathrm{dipole}}$, which possesses higher J and hence μ compared with pure Fe. A small amount (~10 at%) of nitrogen in the iron films enhances the M_S, which can be even larger than the value of bulk iron, while excess nitrogen decreases the M_S. The excess nitrogen-lowered M_S was attributed to the reduction of $\mathrm{Fe}^{\mathrm{dipole}}$ due to the polarized electron's being captured by the excess nitrogen atom.

Consistency between theory predictions and the simulative/experimental results shows that the saturation magnetization M_S and T_C relate to spin-spin exchange energy or the cohesive energy, while the H_C relates to the intergrain exchange energy. The M_S also relates to the μ of individual atoms, which is affected both by the charge localization due to bond contraction and by nitrogen addition that alters the valence value of the Fe atoms. The findings should find applications in designing nanomagnetic devices such as magnetic sensors and magnetic storage media. The study may allow us a more feasible mechanism for adjusting the magnetic behavior of the films by means of both the physical shape and size, and the chemical reaction.

Table of Contents

List of Figures

List of Tables

ABBREVIATIONS

AFM	Atomic Force Microscopy
BBB	Bond-band-barrier
bcc	Body-centered cubic
BOLS	Bond-order-length-strength
CN	Coordination number
DOS	Density of state
fcc	Face-centered cubic
FWHM	Full width at half maximum
H_C	Coercivity
MBE	Molecular beam epitaxy
MC	Monte Carlo
RF	Radio frequency
RMS	Root mean square
M_S	Saturation magnetization
S/V	Surface-to-volume
SSCL	Spin-spin correlation length
T_C	Curie temperature
T_S	Substrate temperature
VSM	Vibrating Sample Magnetometer
XPS	X-ray photoelectron diffraction
XRD	X-ray diffraction

CHAPTER 1 INTRODUCTION

1.1 Motivation

Nanostructured magnetic materials have attracted a great deal of attention because of their potential applications in areas such as high-density magnetic data storage,[1] magnetic sensors,[2,3] color imaging,[4] bioprocessing,[5] and magnetic refrigeration,[6] as well as their significance in fundamental understandings.[7,8] Properties of very small metal particles have been extensively studied in the past 50 years,[9] and much is known about their electronic and geometrical structure. The magnetic properties of nanosize particles differ from those of bulk in two aspects. One is that the large surface-to-volume ratio (S/V ratio) results in a different local environment for the surface atoms in their magnetic coupling/interaction with neighboring atoms, leading to the mixed volume and surface magnetic characteristics; the other is that, unlike bulk ferromagnetic materials, which usually form multiple magnetic domains, several small ferromagnetic particles could consist of only a single magnetic domain. In the case of a single particle being a single domain, superparamagnetism occurs. There are several distinct phenomena for magnetic nanomaterials with the decrease in size; for example, the Curie temperature (T_C) drops with size.[10 - 19] The T_C suppression is a critical problem for magnetic material application in nanometer scales because it may cause structural failure with loss of the ferromagnetic properties. On the other hand, the tunable T_C would be an advantage for magnetic sensors or switches that can function in an expected temperature range. The saturation magnetization (M_S) also varies with decreasing size. There are two opposite trends of observation. One is that the

M_S decreases with size; [20 - 23] the other, however, is that the M_S increases inversely with size.[24 - 27]

Several models have been proposed to explain the size-induced T_C suppression, including the spin-spin correlation length (SSCL) limitation.[28,29] More recently, Nikolaev and Shipilin[30] proposed that the ferromagnetic T_C suppression results from the surface layer that contains atoms with only half the number of exchange bonds per unit volume compared with the bulk. However, the understanding of the underlying mechanism of T_C suppression is under debate. A number of theoretical models have been developed to explain the size-enhanced or tailored magnetization. However, discrepancy remains. A shell model,[21] which calculates the average magnetic moment of the system by considering the different magnetic moments in the surface layers, suggested that the average M_S is enhanced, as the magnetic moment of the surface layer is higher than the bulk value. On the other hand, Monte Carlo simulation[31] based on the Ising model showed that even at temperatures well below the T_C of the bulk, the M_S of the small clusters is lower than the bulk value. Hence, a consistent model is highly desirable to explain the size- induced T_C suppression and M_S tailoring/enhancement.

Introducing atoms of an electronegative element and/or changing the distances of the interacting moments can be realized in the iron-nitrogen (Fe-N) system. The magnetic properties of the nitrogen-poor phases from this system are of interest from the magnetic point of view;[32] for example, the γ'-Fe_4N and in particular the highly metastable α''-$Fe_{16}N_2$, which was first described by Jack[33] in 1953. The first report of a giant magnetic moment of the α''-$Fe_{16}N_2$ film was made by Kim and Takahashi[34] in 1972($4\pi M_S$ = 26.4 kG). The value is even higher than the greatest saturation magnetization that has been achieved in iron-based substitutional alloys in $Fe_{65}Co_{35}$, namely $4\pi M_S$ = 24.5 kG.[35] Since then, much research has been carried out on the Fe-N films. The nitrogen-poor phases with large M_S, high corrosion resistance, and good mechanical properties facilitate applications of these great potential materials such as magnetic recording heads and magnetic recording media.[36] Most theoretical calculations on the crystal of α''-$Fe_{16}N_2$ phase verify its giant magnetic moment. However, the high-magnetization iron nitride films are still far from real applications because of the difficulty in the phase purity and their metastable character.[37] Experimental observations also vary. Morisako[38] and Bobo[39] suggested that the nitrogen could not enhance the M_S, while the work done by Sun *et al*[40] even showed a decrease of M_S of the film when nitrogen atoms were introduced into the iron film, though α''-$Fe_{16}N_2$ was detected. An understanding of the nitrogen-induced magnetization enhancement is thus needed.

Size-induced magnetization deviation contributes to the physical effect, while the nitrogen catalytic-induced magnetization deviation attributes to the chemical effect. At room temperature, the M_S may decrease for nanoferromagnetic materials, while nitrogen catalysis may enhance the M_S. A study of the joint effect of the physical size and nitrogen catalysis is therefore highly desirable.

1.2 Objectives

The aforementioned discrepancy in experimental and theoretical observations demands further investigation of the physical mechanism behind the size dependency. Understanding the mechanism behind the effect of nitrogen catalysis on the magnetization of iron is also important. A study of the combining effect of the physical size and nitrogen catalysis on the magnetization is highly desirable. Two correlation mechanisms provide an opportunity for this kind of further study concerning size and the effect of nitrogen catalysis on the magnetic properties of nanosolids. They are the bond-order-length-strength (BOLS) correlation mechanism for CN imperfection-induced properties variation, and the bond-band-barrier (*BBB*) correlation mechanism for catalysis-induced properties variation. Monte Carlo simulation, which is facilitated by great improvements in the computing speed and experimental facilities of ion beam processing laboratories, provides the simulational and experimental support for the concepts. The main objectives of this work are as follows:

(1) To study the physical mechanism behind the M_S variation together with the T_C suppression and coercivity (H_C) deviation of a ferromagnetic nanosolid.

(2) To investigate the nitrogen catalytic effect on the M_S of iron thin films.

(3) To study the combining effect of the physical size and the nitrogen catalytic effect on the M_S of iron films.

(4) To study the deposition of magnetic materials using the FCVA technique.

Theoretically, analytical solutions to the physical size and nitrogen catalytic effect on the magnetic properties based on the BOLS and BBB correlation mechanism will be derived. The discrepancy of the observations is expected to be reconciled by the model and to be verified by Monte Carlo simulation on the M_S as a function of size and temperature. Experimentally, the problem of the FCVA system when it is used to deposit magnetic films will be solved. Magnetic films of various crystalline sizes will be deposited to study the size effect. Fe-N films with various nitrogen contents will be deposited to investigate the nitrogen catalytic effect on the M_S, and the Fe-N films with various crystalline sizes and nitrogen concentrations will be deposited to investigate the joint effect of physical size and nitrogen catalysis.

1.3 Major contributions

(i). Providing a model that incorporates the BOLS and BBB correlation mechanism into the Brillouin equation and using the "molecular field" concept, this thesis gives a basic and clear explanation for the physical size-induced M_S deviations. The thesis presents the M_S as a function of size and temperature, which is evidenced using Monte Carlo simulation on the spin systems of various physical sizes and geometrical shapes. It shows that, with a decrease in size, the M_S of a nanosolid enhances at low temperature and decreases at temperature below T_C. This reconciles the discrepancy of the observations at different temperatures.

(ii). The model provides a basic understanding of the T_C suppression of the ferromagnetic nanosolid by incorporating the BOLS premise into the Ising model. The same idea can also be applied to and explain well the

T_C suppression of the ferroelectric and superconductive nanosolid by considering a high-order of CN imperfection.

(iii). The nitrogen catalytic effect on the magnetization of iron films shows that a small amount of nitrogen improves the magnetization of iron while too much nitrogen decreases it. This reconciles the conflicting observations. For some specimens, it is even higher than the bulk value.

(iv). The joint effects of physical size and nitridation on the M_S of iron films reveal that the M_S of nitrogen-poor Fe-N films is higher than that of pure iron films, while the M_S of nitrogen-rich Fe-N films is lower. When the grain size is larger than 8 nm, the enhancement of M_S using nitriding can overcome the size-induced reduction of M_S. This is the first contribution in the research of nanomagnetism. It provides further understanding of nanomagnetism and offers guidelines for further study of ferromagnetic nanostructures for high-density data storage and sensor applications.

(v). The FCVA technique has many advantages and it has been applied to produce good quality and dense carbon coatings as well as metal oxide films. This thesis is the first to research the deposition of Fe-N magnetic films using the FCVA technique. The handicap of an unstable arc when depositing ferromagnetic films using FCVA has been overcome by using a unique shield for the ferromagnetic target. Various approaches to nitrogen gas introduction have been adopted, and the bias effects on surface morphology, microstructure, and magnetic properties have been studied. The work opens up avenues for further study of the magnetic films and nitriding films based on the FCVA technique.

1.4 Organization

The thesis starts, in chapter 1, by describing the motivation and the objectives of the research with a brief overview of the studies of physical size and nitrogen catalytic effects on the magnetic properties of ferromagnetic nanosolids. The main contributions of the thesis are also presented in this chapter.

Chapter 2 reviews the literature on the studies of physical size and nitrogen catalytic effects on the magnetic properties of ferromagnetic nanosolids of the past few decades. In accordance with the objectives of the thesis, the survey focuses on magnetization and the Curie temperature. The discrepancies in the various observations on the size effect of M_S, the physical and chemical mechanism behind the T_C suppression of magnetic nanosolids, and the nitrogen catalytic effect on the M_S of iron nanosolids are summarized.

Chapter 3 describes the three types of approaches adopted in this project, namely the theoretical, simulative, and experimental approaches. The theoretical approaches, including the BOLS, the BBB correlation mechanism, and the Ising model, are introduced. The Monte Carlo simulation method together with the simulated spins system (physical size and geometrical shapes) are also introduced in this chapter, as is the experimental FCVA technique together with the sample preparation and characterization.

In chapter 4, the physical size effects on the magnetization and T_C suppression are presented in terms of the aspects of theoretical prediction, simulation, and experimentation. Several concepts are proposed for the size-induced magnetism:

(i) The magnetic moment of a surface atom is enhanced more than that of the center atoms. Electrons surrounding the lower-CN surface atoms are more localized due to the CN imperfection deepened atomic potential (V_{atom}) that confines electrons, which contributes to the magnetic momentum.

(ii) The exchange energy/cohesive energy (atomic *CN* multiplies the single-bond energy) for the lower-CN atom decreases as a result of the reduction in the number of exchange bonds; though for a single bond, the bond length is reduced and the cohesive energy per bond is enhanced.

(iii) The M_S of a solid is affected by both the magnetic moment of an individual atom and the exchange energy that determines the alignment of the spin system. At a very low temperature when the vibrational energy can be neglected, the M_S of a magnetic nanosolid increases compared with the bulk value, while at a high temperature below T_C, the M_S decreases.

(iv) The coercivity (H_C) of thin films increases with a decrease in grain size due to the enhancement of intergrain interaction.

(v) The decrease in the exchange energy with the size reduction contributes to the thermodynamic behavior: the T_C suppression of a ferromagnetic (ferroelectric and superconductive) nanosolid.

Chapter 5 describes the nitrogen catalytic effect on the M_S of Fe films. The chemical reaction between N and Fe transports electrons from the less electronegative Fe to the higher N, which enhances the magnetic moment of Fe due to the altered atomic states and hence increases the M_S of the material. However, excess nitrogen decreases the M_S.

The joint effects of physical size and nitridation on the M_S of iron films are presented in chapter 6. It is found that, in general, the M_S decrease with size. With the same grain size, the M_S of nitrogen-poor Fe-N films are higher than those of pure iron, while the M_S of nitrogen-rich Fe-N films are lower than those of pure iron.

The thesis ends in chapter 7 with a summary of the main conclusions that are reached from having addressed the objectives outlined in chapter 1, and recommendations for further research.

CHAPTER 2 LITERATURE SURVEY

2.1 Physical size effect

2.1.1 M_S suppression or elevation

Two distinguishing trends of the M_S as a function of size have been reported. Some researchers observed that the M_S of a ferromagnetic nanosolid decreases with the size, while other researchers, measuring the enhanced magnetic moment of a ferromagnetic nanosolid, concluded that M_S enhances with the decrease in size.

2.1.1.1 Experimental observations-M_S suppression

In 1976, Sumiyama *et al*[41] reported a remarkable reduction of M_S at room temperature for Fe-Ni invar alloy thin films (<40 nm). Wedler and Schneck[42] also reported a reduced M_S value (1.8 kG) for very thin Ni films (<7 nm). Ohta *et al*[43] studied the M_S for Fe_3O_4 thin films and found a rapid decrease when the film is thinner than 70 nm.

Many studies have reported a decrease in M_S with size. Using the Stern-Gerlach deflections of cold iron clusters in a molecular beam, Heer *et al* [20] found a decrease of measured M_S for small iron clusters (50~230 atoms). Bucher *et al*[44] used the same instrument and measured clusters in a beam as a function of cluster size (N = 20~200) and temperature (T = 82~267 K). They also found a decrease in the measured M_S. The same trends hold for Gd, Tb, and Dy clusters,[45] $Pd_{97.1}Fe_{2.9}$,[22] $NiFe_2O_4$,[70,71] Ni_3Fe,[23] Co,[23] and $Pd_{96}Fe_4$[21] nanocrystals.

Figure 2.1, for example, shows the magnetic moment of Co cluster as a function of size.[69]

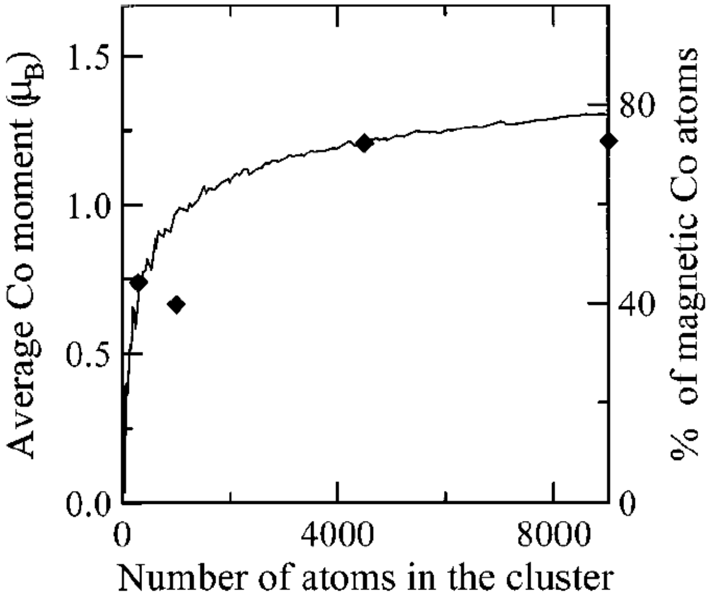

Figure 2.1 The average magnetic moment per Co atom and the percentage of magnetic Co atoms as a function of the cluster size.[69]

2.1.1.2 Experimental observations-M_S elevation

However, opposite trends have also been observed. In 1980, Konno[46] reported an opposite, anomalous result for Fe-Ni films. The measured M_S, in a temperature range from 77 K to 570 K, showed that when the film thickness is decreased from about 75 nm to 35 nm, the M_S tends to increase gradually.

In 1985, using the laser vaporization of an iron rod inside the throat of a high-pressure pulsed nozzle, Cox *et al*[10] were the first to measure the magnetic properties of isolated iron-atom clusters ranging from 2 to 17 atoms as well as the magnetic behavior of the monoxides and dioxides of (2~7) atom iron clusters. The neutral metal cluster beam passed through a Stern-Gerlach magnet and the deflected beam was detected using spatially resolved time-of-flight photo ionization mass spectrometry. The estimated temperature was about 22 K. They concluded that the spin per atom in the iron clusters was larger than that of bulk iron. Billas *et al*[67,50,68] measured the molecular beam deflection of small iron, cobalt, and nickel clusters, and also found that the magnetic moment of the small cluster was larger than that of the bulk value. For clusters with fewer than 30 atoms, the magnetic moment is atom-like; as the size is increased up to 700 atoms, the magnetic moment approaches the bulk limit. It was then concluded that the M_S of the small particle is larger than that of the bulk value. The experiments by Chen *et al*[47] on Co_n particles in the range of 1.8-4.4 nm showed that the magnetic moment of a 1.8 nm size particle is about 30% higher than that of the bulk. Figure 2.2 shows the measured magnetic moments of Ni_n clusters. With oscillation features, the M_S increases with the inverse of size.[48]

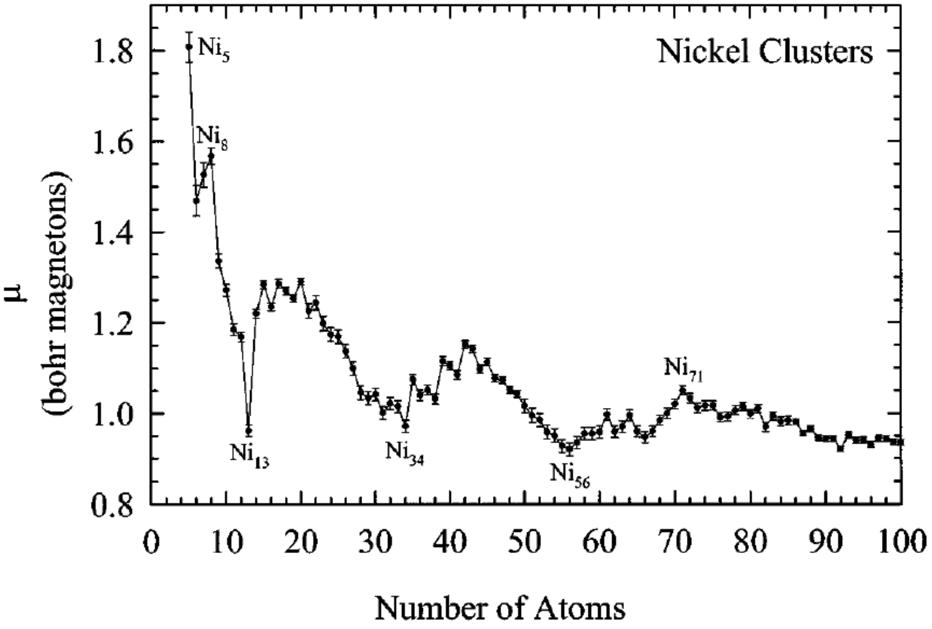

Figure 2.2 Magnetic moments of Ni_n particles as a function of size, at temperatures between 73 and 198 K.[48]

2.1.1.3 Theories and explanations-M_S suppression

Theoretically, the M_S suppression at ambient temperature has been explained[49] as the higher-spin temperatures of the surface spins that are weakly coupled and are more disordered at the measurement temperatures compared to the bulk spins. The M_S is then dominated by the interior bulk spins that drop in number when the solid size is decreased. Alternatively, the M_S suppression has been explained as a result of the T_C suppression of the nanosolid. In a shell structure, the surface layer is magnetically melted and contributes little to the M_S of the system.[31] An empirical linear dependence[49] of the specific $M_S(K_j)$ on the specific surface area $S(K_j)$ of the fine crystallites has been proposed in the form of:

$$\Delta M_S(K_j)/M_S(\infty) = -A \times S(K_j) \tag{2.1}$$

where K_j is the diameter of the grain and A is a constant. Bucher *et al*[44] attributed the decrease of magnetization of Co clusters to the operating temperature. The effective magnetic moment at temperature T can be expressed as:

$$\mu_{eff} = \mu_T[\coth(\frac{N\mu_T H}{k_B T}) - \frac{k_B T}{N\mu_T H}] \tag{2.2}$$

where μ_T is the true magnetic moment per atom of the particle, where N is the atom number and H is the applied magnetic field.

Merikoski *et al*[31] have also carried out Monte Carlo simulations on the magnetization of small ferromagnetic clusters at finite temperatures based on the Ising model. The simulation results showed that even at very low temperature, the M_S decreases with the decrease in size. The experimental observed M_S reduction for isolated ferromagnetic clusters was then believed to arise from the increase of spin temperature as it was observed in the simulation.

2.1.1.4 Theories and explanations-M_S elevation

For the enhancement observations at low temperature, Billas *et al*[50] used a shell model and explained that the M_S is enhanced as the magnetic moment of the surface layer is higher than the bulk value, which agrees with experimental observations.[51,52,53,54,55] For example, Ney *et al*[53] showed that the Co surface atoms carry a moment of 2.28 μ_B per atom enhanced by 32% compared to the bulk value of 1.73 μ_B per atom. Compared to the Fe bcc bulk moment of 2.2μ_B, the magnetic moment for the surface layer of Fe has been found to enhance (i) by 15% to 2.54μ_B for 1 ML Fe/5 ML W (110), and (ii) by 29% to 2.84μ_B for 2 ML Fe/5 ML W (110). The significant surface relaxation of Fe (310)(-12%)[56]

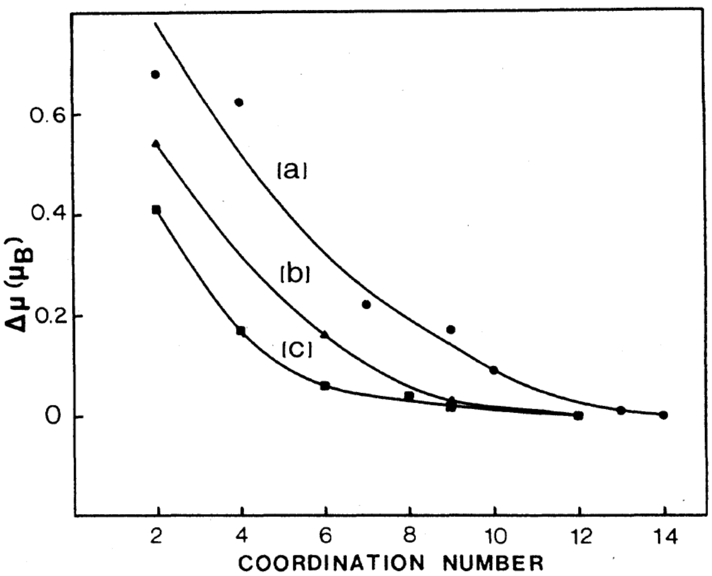

Figure 2.3 Deviation from the bulk magnetic moment in (a) Fe, (b) Co, and (c) Ni as a function of nearest neighbor coordination (in various structures).[58]

and Ni (210)(-12%)[57] has also been found to enhance the atomic magnetic momentum by up to 27%. The magnetic moment of the surface atom was considered to be primarily determined by the local CN. Figure 2.3 shows the calculated dependence of the magnetic moment on the nearest CN using an *ab initio* tight-binding theory. It is clear that as the CN decreases, the moment increases toward the atomic value.[58] Table 2.1 summarizes both the experimental and the theoretical or simulating research on the size dependence of the M_S of magnetic nanosolid.

The magnetic moment of ferromagnetic nanosolid as a function of size was also found to possess an oscillation with some magic numbers at which the cluster shows a particularly low magnetic moment,[67,25,26,27] as shown in the Ni clusters in Figure 2.2 for example. From a theoretical point of view and with the aim to understand the oscillatory magnetic behavior of the transition metal clusters, several geometrical shell models have been proposed.[25,26,27,59] In particular, in the model developed by Jensen and Bennemann,[59] the individual magnetic moments of the different atoms are determined by their local atomic coordination. By assuming bulk-like structures (fcc and bcc) and different global cluster shapes (cube, octahedron, and cube octahedron), these authors found that the average magnetic moment oscillates with the cluster size, and that this magnetic "shell structure" reflects the progressive formation of concentric atomic layers. Fridel [60] considers a simple rectangular d-band approximation together with the second moment approximation,[61] and the assumption that the d-band splitting between the major and the minor spin caused by the exchanged interaction is invariant for the cluster to the bulk solid leads to the following expression[62] for the magnetic moment as a function of the local CN in a step function:

$$\mu_i/\mu_b = \begin{cases} \mu_{\text{dim}}/\mu_b\,, & if \quad z_i \le z_b\left(\mu_b/\mu_{\text{dim}}\right)^2 \\ \left(z_b/z_i\right)^{1/2}, & \qquad otherwise \end{cases} \tag{2.3}$$

where μ_b, μ_{dim}, and μ_i are the magnetic moment of an atom in the bulk, a dimmer, and the *i*th atomic layer, respectively. In the case of Fe, $\mu_b = 2.22\ \mu_B$ and $\mu_{dim} = 3.2\ \mu_B$,[63] where μ_B is the Bohr magneton. For $z_b = 12$, the step function transits at $z_i = 5.75$. Corresponding shell structures have been developed for various crystal structures.[64] Considering the geometrical

Table 2.1 Discrepancy in the M_S as a function of size.

Approach	Experimental material / theoretical approach	M_S increase (↑) inversely with size	M_S decrease (↓) with size	Temperature
Experiment	MnBi films	M_S has no dependence on thickness [65]		Room temperature(RT)
	Fe-Ni films	↑[46]	↓[41]	RT[41] 77 to 570 K[46]
	Ni films		↓[42]	RT
	Fe_3O_4 films		↓[43] [66]	RT
	Fe, Co, Ni cluster	↑[10][67][50][68][48]	↓[20][48][45][69][44]	78~120K 73,198K
	$NiFe_2O_4$ nanoparticles		↓[70,71]	4.2~100K
	$Pd_{97.1}Fe_{2.9}$ particles		↓[22]	5 K
	Ni_3Fe nanocrystalline		↓[23]	<150 K
	$Pd_{96}Fe_4$ particles		↓[21]	4.2,100,295K
Theory	Self-consist-field Xα-scattered-wave molecular-orbital calculations	↑[25]		All temperature
	Films, all-electron self-consistent semi-relativistic full-potential linearized augmented-plane-wave local density and local-spin-density	↑[27]		RT
	Tight-binding Hubbard Hamiltonian in the unrestricted Hartree-Fock approximation	↑[26]		0 K
	Monte Carlo simulation, Ising model		↓[31]	$< T_C$
	Shell model	↑[50]		78~120K
	Surface model		↓[70,72]	<5 K

arrangement of atoms in different lattice structures of various solid shapes, the oscillation features could be generated using the shell model.[62]

2.1.2 T_C suppression

In 1969, Morita and Taniyama[73] found a drop in the T_C when the evaporated nickel films were thinner than 30 nm. T_C suppression has also been found to happen to Fe, [10,74,75] Ni, [14-16, 76,77] Co, [11,12] and Gd, [17,78] thin films and Fe_4O_3 particles,[79] as well as the nanocrystalline Gd[80] and $GdFe_{11}Re$.[81,82] The tunable T_C will be an advantage for magnetic sensors or switches that can function in a given temperature range. However, the understanding of the underlying mechanism for T_C-tunability is still primitive, though models based on the criterion of SSCL limitation have been developed.[28,29]

According to the scaling theory,[28] the correlation length is defined as the distance from a point beyond which there is no further correlation of a physical property associated with that point. Values for a given property at distances beyond the correlation length can be considered purely random. The SSCL, ξ, depends functionally on temperature as $\xi = \xi_0 (1 - T / T_C)^{-v}$, where v is a universal critical exponent. The SSCL limitation premise indicates that ξ is limited by the film thickness. If the ξ exceeds the film thickness D, $\xi > K_j = D / d$, the T_C will be lower than the bulk value. d is the atomic diameter of the ferromagnetic element concerned. The SSCL mechanism gives rise to the power-law form of the $T_C - K_j$ relation, which involves two freely adjustable parameters, λ and C (or C_0), for data simulation. The λ-value is in the range of

1 for the mean-field approximation to 1.59 for the three-dimensional Ising model:[13,28,29,83,84]

$$\frac{\Delta T_C(K_j)}{T_C(\infty)} = \frac{T_C(K_j) - T_C(\infty)}{T_C(\infty)} = (C_0 K_j)^{-\lambda} \tag{2.4}$$

In order to converge the numerical simulation with the measured data of ultra-thin films ($K_j \rightarrow 0$), Binder, Hohenberg,[84] and Huang *et al*[85] revised Eq (2.4) by replacing the reference $T_C(\infty)$ with the K_j-dependence $T_C(K_j)$ for normalization. With the revised premise, numerical fit could be improved for ultra-thin films:

$$\frac{\Delta T_C(K_j)}{T_C(K_j)} = \frac{T_C(K_j) - T_C(\infty)}{T_C(K_j)} = (C' K_j)^{-\lambda'} \tag{2.5}$$

Based on the mean field approximation, Zhang and Willis[86] proposed an alternative to fit both the thinner and the thicker films with a step function:

$$\frac{\Delta T_C(K_j)}{T_C(\infty)} = \frac{T_C(K_j) - T_C(\infty)}{T_C(\infty)} = \begin{cases} -(\dfrac{\xi + 1}{2K_j})^{\lambda}, & (K_j > \xi) \\ \dfrac{K_j - 1}{2\xi} - 1, & (K_j < \xi) \end{cases} \tag{2.6}$$

Eq. (2.6) shows that, for $K_j < \xi$, T_C varies linearly with K_j and if $\lambda \neq 1$, there is a discontinuity at $K_j = \xi$.

More recently, Nikolaev and Shipilin[30] proposed that the ferromagnetic T_C suppression results from nothing more than the surface layer that contains atoms with only half the number of exchange bonds (CN imperfection, as termed in this presentation) per unit volume compared with the bulk. By defining a critical thickness ΔR, the T_C suppression of a ferromagnetic spherical dot can be expressed as follows:[30]

$$\frac{\Delta T_C(R)}{T_C(\infty)} = -\frac{3\Delta R}{2R} \tag{2.7}$$

The quantity ΔR was used as a parameter to characterize the number deficiency of exchange bonds for atoms at the surface region of a nanosolid. However, fitting experiment data for Fe_3O_4 nanosolids of different sizes with a constant ΔR was unsuccessful, and hence, it is suggested that the ΔR varies with the solid size, but the R dependence of ΔR is yet to be established.[30]

2.1.3 H_C and μ_p

Coercivity: For a freestanding nanosolid, or a single domain, the coercivity approaches zero when the size is decreased to a certain size.[87,88] For example, $Fe_{69}Ni_9Co_2$ powders having grain sizes of 10-15 nm show almost no hysteresis, which is suggested to be superparamagnetic,[89] due to the long-range interaction that involves the high-order atomic CN imperfection.[90] However, for polycrystalline magnetic materials, the superparamagnetic behavior vanishes and the coercivity appears.[87,91] The coercivity increases with size in a D^6 pattern until a critical size of 10s nm and then the H_C drops in a D^{-1} fashion when the solid grows from atomic scale to micrometer scale, and eventually approaches the bulk value.[92] The D^{-1} fashion of H_C variation was explained by the authors as domain-wall pinning at grain boundaries. Investigation of the $Fe_{74.5-x}Cu_xNb_3Si_{13.5}B_9$ (x = 0~1 at%) ribbons with grain sizes between 10 nm and 300 nm has shown that the $H_C(D)$ transition from D^6 to D^{-1} happens at 50 nm.[92] Similar trends hold for Fe, Ni, and Co metal films,[93] and the respective transition sizes are 20, 40, and 30 nm. The behavior has been explained using the random anisotropy theory:[94]

$$H_C \sim \frac{1}{20}\frac{K_2^4 L^6}{B^3 M_0} \tag{2.8}$$

where K_2 is the strength of local uniaxial anisotropy and M_0 is the magnitude of the local magnetization vector; B is the exchange stiffness parameter and L is the structural correlation length. Eq (2.8) applies when the magnetic scale length greatly exceeds the structural scale length. Recently, the H_C of antiferromagnetic-ferromagnetic nanostructures have also been reported to increase inversely with size.[95]

Permeability: The initial permeability has been found to increase with decreasing gain size for several kinds of materials. For example, a study on the polycrystalline $Ni_{0.34}Cu_{0.12}Zn_{0.56}Fe_{1.98}O_4$ with different grain sizes up to 39 μm found an increase of initial permeability when the grain size was reduced.[96] Similarly, the initial permeability of nanocrystalline $Fe_{86}Zr_7B_6Cu_1$ ribbons with grain sizes from 13.2 to 7.3 nm was found to increase from 1.2×10^4 to 6.3×10^4.[97] The same tendency was found with the NiFe permalloy, as reported by See *et al.*[98] The results were interpreted in terms of the contribution of grain boundaries and pores inside the grains to the domain wall pinning.[99] However, reverse trends have also been reported.[100] The changes has been modeled using the nonmagnetic grain boundary model (NMGB), which assumes a regular simple cubic distribution of cubic particles of size D separated by a gap δ,[101]

$$\mu_{p-eff} = \frac{D\mu_{p-i}}{(D + \delta\mu_{p-i})} \tag{2.9}$$

where μ_{p-i} is the intrinsic permeability. This model is valid only if $D >> \delta$ since only the reluctance of the particles and the air gap between them are taken into account.

2.2 Nitridation effect

2.2.1 Iron-nitrogen system

As shown in Figure 2.4, the iron-nitrogen system consists of several interstitial solutions (α, γ, ε), chemical compounds (γ′-Fe_4N, ζ-Fe_2N), and metastable phases (α′, α″-$Fe_{16}N_2$) with various mechanical and magnetic properties.[102] The nitrogen-poor phases are ferromagnetic compounds. In particular, the α″-$Fe_{16}N_2$ has been reported to have a giant magnetic moment[34] with potential applications in high-density magnetic recording media.

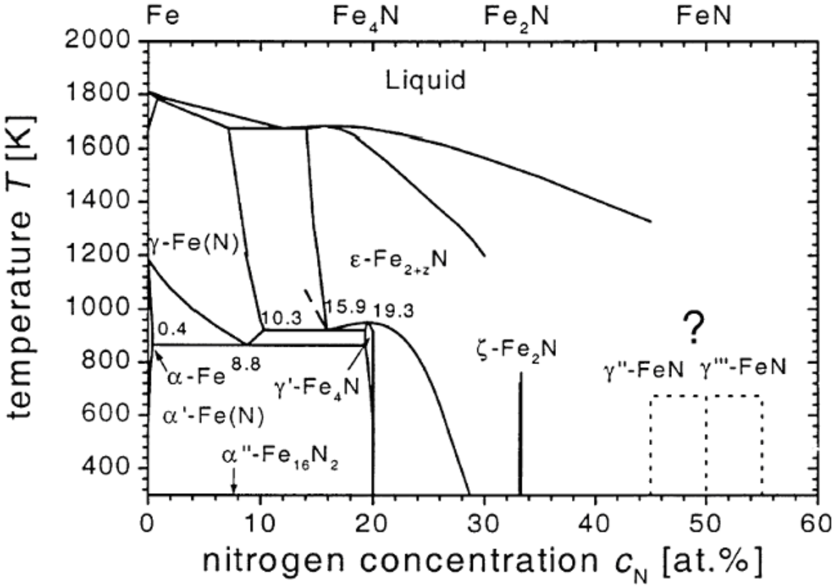

Figure 2.4 Phase diagram of the Fe-N system.[102]

The α iron phase with a small amount of nitrogen solute leads to the α-Fe(N) phase. It has a maximum equilibrium solubility of interstitial nitrogen in body center cubic (BCC) iron of just 0.4 at% at 860 K.[103] The lattice dilation in α-Fe(N) d(ln V)/dx is about 0.002,[33] where V is the unit volume of the lattice and x is the one-dimensional lattice parameter. More nitrogen can be incorporated into the BCC lattice of thin films prepared by reactive sputtering or ion implantation. The cubic films may accommodate up to 10 at% nitrogen, with a nonuniform profile across the film.[104] They have a microcrystalline structure with possible secondary γ′-Fe_4N and α″-$Fe_{16}N_2$ phases. Their $4\pi M_S$ has been reported to be similar to, or higher than, that of α-Fe.[104,105,106,107,108] Quenching γ-Fe(N) at 920 K will transform martensitically into the tetragonal α′ nitrogen martensite (α′-Fe(N)). The greatest solubility of nitrogen in γ-Fe is 10.5%. Typically, the martensitic transformation is incomplete, and the resulting bulk material is a mixture of tetragonal nitrogen martensite and γ-Fe(N). The nitrogen in the α′ phase is disordered, and it induces a lattice expansion d(ln V)/dx of 0.006. There is a continuous range of composition.[109] Epitaxial thin films of the α′ phase can be prepared directly by Molecular beam epitaxy (MBE),[110] reactive sputtering,[111] ion beam deposition,[112] or nitrogen ion implantation.[109]

Prolonged annealing (tempering) of the α′ phase at about 370-420 K leads to an ordering of the nitrogen to produce α″-$Fe_{16}N_2$. It was first described by Jack in the early 1950s.[33] The unit cell with $a = 0.572$ nm and $c = 0.629$ nm is doubled in all three directions. The structure was later refined by electron diffraction.[113] Prolonged annealing or higher temperature treatment leads to decomposition of the α'' compound into α-Fe and γ'-Fe_4N. The limited solubility of nitrogen in γ-Fe – at most, 10.5 at% – means that it is impossible to obtain a pure 16:2 phase (11.1 at%) by quenching and annealing. The giant magnetic moment of α''-$Fe_{16}N_2$ was first noted by Kim and Takahashi on iron films evaporated in nitrogen ambient.[34] Their films were a mixture of α-Fe and the α'' phase, and the $4\pi M_S$ of α''-$Fe_{16}N_2$ was estimated to be as high as 28 kG, corresponding to an average iron moment of 3.0 μ_B.

The face-centered cubic (FCC) γ'-Fe_4N lattice is expanded by 33% by interstitial nitrogen in the center position of FCC, giving a lattice parameter of 0.3795 nm, compared with 0.3450 nm for γ-Fe; $d(\ln V)/dx = 0.017$. The nitrogen-induced expansion stabilizes a ferromagnetic state for γ'-Fe_4N with a T_C of 767 K. At room temperature, the $4\pi M_S$ is 19 kG.

The hexagonal ε-Fe_3N has an extended homogeneity range, with a moment that decreases rapidly with increasing nitrogen content. The compound is ferromagnetic and the moment is 1.9 μ_B. Orthorhombic ζ-Fe_2N is a quasistable compound with a tiny hyperfine field of 8 kG, while metastable cubic nitrides, containing nearly 50 at% nitrogen, may have ZnS or NaCl structures.[114] The ZnS-type nitride has been shown to be a nonmagnetic metal, while the NaCl-type nitride is an antiferromagnet.[115] A schematic illustration of the crystal structure of α-Fe, α''-$Fe_{16}N_2$, γ'-Fe_4N,[32] FeN with ZnS and NaCl structures is given in Figure 2.5.

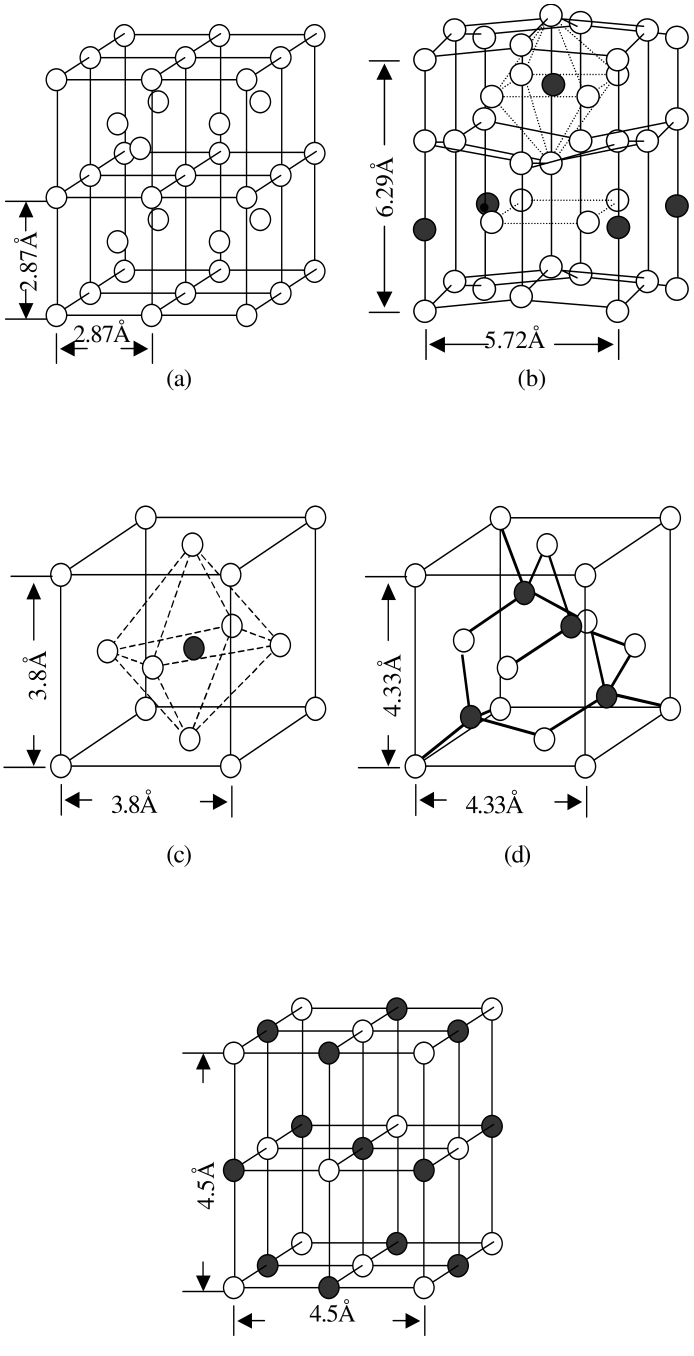

(a) (b)

(c) (d)

(e)

Figure 2.5 A schematic illustration of the crystal structure of (a) α-Fe; (b) α''-$Fe_{16}N_2$; (c) γ'-Fe_4N;[32] (d) FeN with ZnS structure; and (e) FeN with NaCl structure.[115] (O: Iron atom •: Nitrogen atom)

2.2.2 Synthesis of nitride films

Various deposition techniques have been used to deposit Fe-N films, such as MBE,[116] multishot implantation,[117] facing target sputtering,[38,40] and reactive radio frequency (RF) sputtering.[39] Table 2.2 summarizes the progress in the synthesis of Fe-N magnetic films or powder over recent decades. After Kim and Takahashi[34] reported the giant magnetic moment of $Fe_{16}N_2$ in 1972, much research has focused on its high magnetic momentum. Many experimental studies have been performed to confirm the giant magnetic moment.[118] The results, however, vary. Komuro,[144] Nakajima,[117,148] Jiang,[120] and Guibin[125] showed that the nitrogen could enhance magnetization by 16~28% regardless of the different deposition techniques. Wang and Zheng *et al*[135]recently confirmed that when little nitrogen was introduced into the iron films, magnetization increased. However, Morisako[38] and Bobo[39] suggested that the nitrogen could not enhance the M_S, while the work done by Sun[40] even showed a decrease of the M_S of the film when nitrogen atoms were introduced into the iron film, though α''-$Fe_{16}N_2$ was detected.

The theoretical studies support that nitrogen can enhance the magnetic moment of iron. Using the self-consistent linearized-augmented-plane-wave (LAPW) method within the framework of the LDA (local-density approximation), Nakajima *et al*[119] performed the band calculations for the $Fe_{16}N_2$ phase. The results showed that the calculated magnetic moment was much smaller than the giant value observed experimentally. The calculated average magnetic moment was 2.35 μ_B. The lattice constant dependence of the moment showed that a little

Table 2.2 Survey of Fe-N magnetic films and powders.

Year	Researchers	Method	Phases	$4\pi M_S$
1972	Kim and Takahashi[34]	Evaporated in nitrogen	α+α″	26.4 kG
1984	Terada *et al*[108]	Ion beam deposition	Multiphases	24 kG
1989	Nakajima and Okamoto[148]	Ion implantation	Multiphases	Increased
1989	Jiang *et al*[120]	Facing target sputtering	Multiphases	$\mu_S = 2.85\mu_B$
1990	Komura *et al*[144]	MBE	Multiphases	26.6 kG
1990	Wang *et al*[106]	RF-diode-sputtering	Multiphases	21 kG
1991	Morisako *et al*[38]	Facing target sputtering	α+γ′	21.36 kG
1993	Russak *et al*[104]	DC magnetron sputter	Multiphases	25 kG
1994	Xiao and Chien[121]	RF reactive sputtering	γ′, ε and ζ	-
1994	Huang *et al*[109]	Treating powder in NH_3 gas	α+α′+α″	(α″)26.6 kG
1994	Sugita *et al*[110]	MBE	α′+α″+γ	(α″)29 kG
1995	Bobo *et al*[39]	Reactive RF sputtering	Expanded α, γ′, ε, ζ	$M_S \sim M_S$(αFe)
1995	Sun *et al*[40]	Facing target sputtering	α+α″+ε+ζ	-
1995	Utsushikawa and Niizuma[122]	Ion nitriding in N_2 plasma	α+α″+γ+ε+ζ	(α″) 27.77 kG
1996	Okamoto *et al*[112]	Sputter beam method	α′ α′+α″	(α′)23.3 kG (α′+α″)24.7 kG
1996	Sugita *et al*[146]	MBE	α″	$\mu_S = 3.5\ \mu_B$
1996	Okamoto *et al*[149]	Sputter beam method	Multiphases	25 kG
1996	Niederdrenk[123]	Reactive magnetron sputtering	ε-Fe_2N_{1-z} ($0 \leq z \leq 0.33$)	-
1997	Takahashi *et al*[105]	Reactive sputtering	α+α′+α″	σ_S(α″) = 240 emu/g
1997	Ohagai *et al*[107]	RF reactive sputtering	α+γ-Fe_4N	24.4 kG
1997	Brewer *et al*[111]	Reactive sputtering	α′ (54%)+α″ (46%)	22.37 kG
1997	Alvarez-Fregoso[124]	Electron cyclotron resonance plasma system	Single ε-Fe_3N	Hardness presented
1997	Guibin[125]	Ion beam enhanced deposition (IBED)	α+α′+α″+γ′+ε	-
1997	Ding *et al*[126]	Reactive ion beam sputtering	Highest α′/α″ phase content	Did not exhibit largest σ_S
1998	Kiriake[35]	Magnetron sputtering	α+α′+α″	23.7 kG
1998	Ding *et al*[127]	Reactive ion beam sputtering	Multiphases	Enhanced but no directly related to α′+α″
1998	Paseka *et al*[128]	Ball milling in NH_3	α+α″+γ′	Enhanced
2000	Lančok *et al*[129]	Nitriding powder in H_2+NH_3	α+α′+α″+γ	-
2000	Yamaguchi *et al*[130]	Nitriding iron in ammonia-hydrogen gas at 500^{o}C	Fe_4N	σ_S =188 emu/g
2001	Jirásková *et al*[131]	Spark erosion, plasma nitriding, and plasma immersion ion implantation	α(50%)+α′&α″ (20%)+γ(30%), Fe_2N	-
2002	Iwatsubo *et al*[132]	Reactive ion beam sputtering	Multiphases	23.5 kG
2002	Grachev *et al*[133]	MBE in a flow of atomic nitrogen from an RF plasma source	γ′-Fe_4N	-
2003	Kappaganthu and Sun[134]	RF sputtering	Multiphases	-
2003	Wang *et al*[135]	Magnetron sputtering	FeN, ε, $FeN_{0.056}$	Enhanced
2003	Nie *et al* [136]	RF sputtering	α-Fe(N), prefer (110)	-

difference in the lattice constant did not cause a substantial change in the magnetic moment. He *et al*[137] calculated the electronic structure of $Fe_{16}N_2$ by the linear muffin-tin orbital method in the atomic-sphere approximation (LMTO-ASA). Sakuma,[138] Min,[139] and Ishida *et al*[140] also calculated the electronic and magnetic structure of $Fe_{16}N_2$ using the same method. All of these calculations obtained an average magnetic moment of 2.4~2.5 μ_B. Using the spin density functional theory, Sifkovits[141] studied the chemical bonding and magnetism of iron nitride and found the following magnetic moment for various Fe and Fe nitride films (see Table 2.3).

Table 2.3 Magnetic moment of Fe/Fe-N.[141]

Fe/Fe-N	Fe (fcc)	Fe_4N	Fe_3N	ζ-Fe_2N
Magnetic moment	2.7 μ_B	2.7 μ_B	1.99 μ_B	1.43 μ_B

Many studies have also been carried out to get a high percentage of α′ and α″ phases in the nitride films. Bulk samples containing 30-60% α″-$Fe_{16}N_2$ have been produced by the quench and anneal route.[109,142,143] A larger amount of α″ phase (≥ 80%) can be stabilized in thin films grown by MBE,[110,144,145,146] reactive sputtering,[105,111] ion implantation,[147,148] or ion beam deposition.[149,150]

Borsa *et al*[151] have developed an all-nitride magnetic tunnel junction. However, only the primary results of the growth and properties of γ′-Fe_4N, α″-$Fe_{16}N_2$, and Cu_3N were reported. Epitaxial γ′-Fe_4N films were grown by MBE of iron in the presence of atomic nitrogen from an RF atomic source. Layers of Cu_3N were grown in a similar fashion. The α″-$Fe_{16}N_2$ phase was synthesized by nitriding epitaxial iron layers. At that time, no pure Cu_3N or α''-$Fe_{16}N_2$ phase could be obtained.

From the above survey of the literature, it can be seen that further investigation of the size-induced magnetic properties of ferromagnetic nanosolids that could reconcile the discrepancy and provide a better basic understanding is highly desirable. The nitridation effect on the iron films also needs further investigation. In particular, the joint effect of physical size and nitridation should be examined. As the objectives listed in section 1.2, this thesis investigates these aspects.

CHAPTER 3 APPROACHES

Three approaches have been used in this study: theory/model, simulation, and experiment. The theories/models approach is based on the BOLS correlation mechanism, the BBB correlation mechanism, and the Ising model. The Monte Carlo simulation, which incorporates the BOLS correlation mechanism into the Ising model, is applied to study the size and temperature influence of the magnetic properties of a nanosolid. Experimentally, the FCVA technique is applied to deposited magnetic thin films of various grain sizes and Fe-N films with various nitrogen contents to investigate the physical size effect and the nitrogen catalytic effect on the magnetization, respectively.

3.1 Theory

3.1.1 BOLS correlation

The BOLS correlation mechanism[152,153] attributes the origin of the physical properties of a nanosolid to the CN imperfection of atoms at the surface or at the site surrounding defects. It is known that the CN imperfection at a surface site causes the remaining bonds of the atom to contract spontaneously corresponding with an enhancement of bond energy.[154,155] The bond energy rise contributes not only to the cohesive energy (E_{coh}) but also to the energy density in the relaxed surface region. The E_{coh} relates to thermodynamic properties such as self-assembly growth, diffusion, chemical reactivity,[156] melting,[157] and phase transition.[158,159] The energy density rise per unit volume in the relaxed region will contribute to the Hamiltonian, which determines such aspects as the entire band structure (band gap and core-level shift),[160,161,162] mechanical strength,[156] phonon frequency, and the dielectrics of a nanosolid of which the surface curvature and the portion of surface atoms vary with particle size.[163,160,161]

The CN imperfection-induced bond relaxation can be defined as $d_i = c_i d$ by introducing a coefficient $c_i < 1$ for bond contraction and $c_i > 1$ for bond expansion. The bond contraction and the response of bond energy can be expressed as:

$$\begin{cases} \dfrac{\Delta d_i}{d} = c_i - 1 < 0; \\ \dfrac{\Delta \varepsilon_i}{\varepsilon} = \dfrac{\varepsilon_i}{\varepsilon} - 1 = c_i^{-m} - 1 > 0 \\ c_i = \dfrac{2}{1 + \exp[(12 - z_i)/8z_i]} \end{cases} \tag{3.1}$$

where c_i is the bond contraction ratio that is a function of CN, z_i.[164] Subscript i denotes the ith atomic layer, which may be counted up to three from the outermost atomic layer to the center of the solid as no CN reduction is expected for $i > 3$. The m describes the bond-length dependence of the binding-energy change, $\varepsilon_i = c_i^{-m}\varepsilon$, at equilibrium atomic separation, as illustrated in Figure 3.1. The c_i^{-m} is independent of the types of interatomic potential. Previous research has revealed that for elemental solids, $m = 1$; for compounds and alloys, $m = 4$.[165,166] The d and ε are the corresponding bulk values.

The CN dependence of the reduced bond length is shown in Figure 3.2. The bond contraction is about 12%, 6%, and 3% when the CN of the atom is reduced from 12 to 4, 6, and 8, respectively. CN imperfection and bond contraction happen at any site where a structure defect exists such as an amorphous state. However, in a bulk crystal, this effect is negligible because of the small *S/V* ratio. With the size reduction, the *S/V* ratio increases. This causes the surface atoms to play an increasingly dominant role in the nanomaterial. The *S*/*V* ratio of the *i*th surface layer can be expressed as:[167]

$$\gamma_i = N_i / N_j = V_i / V = \frac{R^n_{i-out} - R^n_{i-in}}{R^n_{1-out}} \tag{3.2}$$

where n is the dimensionality of a nanosolid and $R = K_j d$ is the radius of a rod (n = 2) or a spherical dot (n = 3), or a thin plate (n = 1). The $R_{i\text{-}out}$ or $R_{i\text{-}in}$ corresponds to the outer or inner radius of the *i*th atomic layer with respect to the center of the solid. The N_i and V_i are the atom number and the volume of the *i*th surface layer, respectively. N_j and V are the whole atom number and the volume of the nanosolid, respectively.

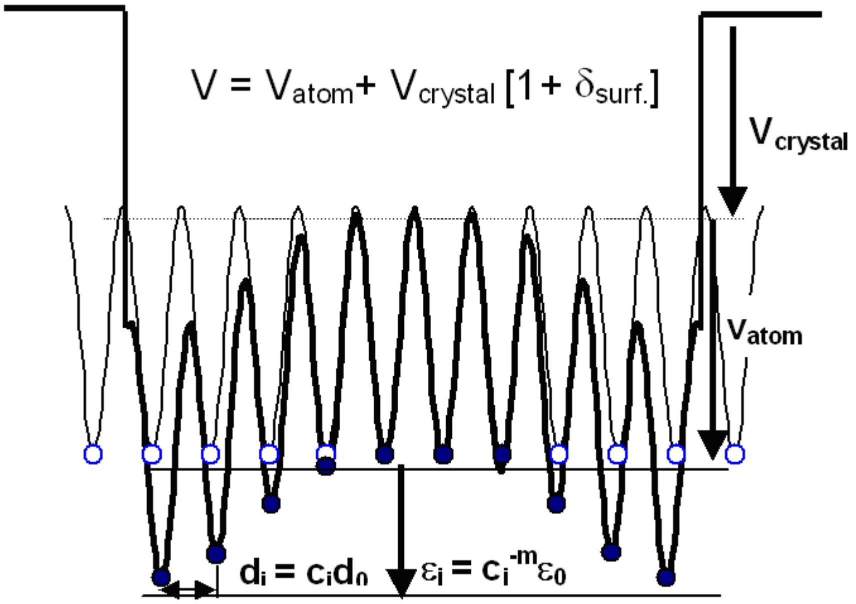

Figure 3.1 Schematic illustration of the effect of atomic CN imperfection on the bond length and atomic trapping potential well depth of the lower-coordinated atoms near the edge of a surface. The deepened atomic potential (V_{atom}) confines electrons that contribute to the magnetic momentum of the lower-CN atoms. δ_{surf} is the perturbation to the crystal potential (V_{crystal}) due to CN imperfection.[153]

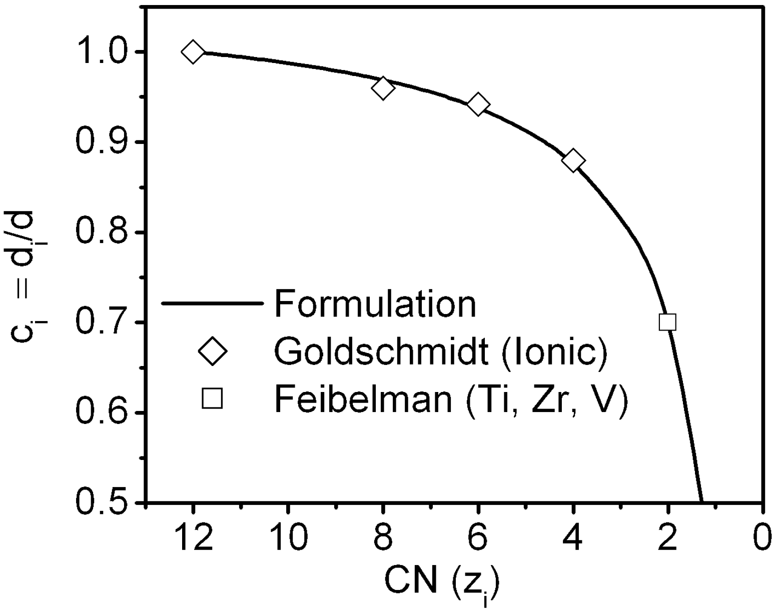

Figure 3.2 CN dependence of bond contraction derived from Goldschmidt's premise, and findings of Feibelman (open square)[164] in which CN = 12 is the standard.[165]

Generally, the mean relative change of a traditional quantity Q of a nanosolid containing N_j atoms, with dimension K_j, can be expressed as $Q(K_j)$, and as $Q(\infty)$ for the same solid without surface relaxation. The $Q(K_j)$ relates to $Q(\infty) = N_j q$ using a shell structure as follows:

$$Q(K_j) = (N_j - N_s)q + N_s q_s = N_j q + N_s (q_s - q) \tag{3.3}$$

The q and q_s correspond to the density of Q inside the bulk and in the surface region, respectively. $N_s = \sum N_i$ is the number of atoms in the surface atomic shells. Eq. (3.3) leads to the immediate general expression of size-induced change of physical properties Q:

$$\begin{aligned}\frac{\Delta Q(K_j)}{Q(\infty)} &= \frac{Q(K_j)-Q(\infty)}{Q(\infty)} = \frac{N_s}{N_j}\left(\frac{q_s}{q}-1\right) \\ &= \frac{\sum_{i\le 3} N_i(q_i-q)}{N_j q} = \sum_{i\le 3}\gamma_i(q_i/q-1) \\ &= \sum_{i\le 3}\gamma_i(\Delta q_i/q)\end{aligned} \tag{3.4}$$

The weighting factor, γ_i, is the S/V ratio (see Eq. (3.2)) that changes with the dimension (K_j) and dimensionality (n) of the solid.

3.1.2 BBB correlation

The details of the BBB correlation mechanism are described in reference [152]. Briefly, the BBB correlation mechanism initiated and verified that an oxygen or nitrogen atom hybridized its *sp* orbitals upon reacting with a solid surface. In the process of oxidation/nitridation, nonbonding lone pairs, antibonding dipoles, and hydrogen-like bonds are involved, which add corresponding density-of-states (DOS) features to the valence band of the host. The modified valence state should contribute to the magnetization of a ferromagnetic solid.

3.1.3 Ising model – exchange interaction

For a magnetic system, the Ising model[168] supposes that electron spins take up and down orientations. The model applies a simple classical assumption to an atomic or electronic magnetic moment, which can take two values:

$$s_i = \begin{cases} +1, & \text{spin up} \\ -1, & \text{spin down} \end{cases} \tag{3.5}$$

The force between two magnets falls inversely with the atomic distance. A reasonable approximation is to assume that any spin interacts only with its nearest neighbors. The interaction energy can be approximated by:

$$E = -\sum_{<i,j>} J_{exc} s_i s_j - H \sum_i s_i \tag{3.6}$$

If the interaction strength $J_{exc} > 0$, the system is ferromagnetic. The energy is minimized if the spins point in the same direction $s_i s_j = +1$. If $J_{exc} < 0$, the system is antiferromagnetic. H represents an external magnetic field which couples to the magnetization:

$$M = \sum_i s_i \tag{3.7}$$

3.2 Monte Carlo simulation

3.2.1 Introduction

Monte Carlo simulation is a stochastic technique used to solve mathematical problems. The word "stochastic" means that it uses random numbers and probability statistics to obtain an answer. Monte Carlo methods randomly select values to create scenarios of a problem. These values are taken from within a fixed range and selected to fit a probability distribution (e.g. bell curve, linear distribution, etc.). In Monte Carlo simulation, the random selection process is repeated many times to create multiple scenarios. Each time a value is randomly selected, it forms one possible scenario and solution to the problem. These scenarios give a range of possible solutions, some of which are more probable and some less. When repeated for many scenarios (10,000 or more), the average solution will give an approximate answer to the problem. The accuracy of this answer can be improved by simulating more scenarios. In fact, the accuracy of a Monte Carlo simulation is proportional to the square root of the number of scenarios used.

3.2.2 Methodology

Monte Carlo simulation of the magnetic system is based on the Ising spin system. Many interesting magnetic properties are related to the dynamics of the spin system.[169,170,171] At low temperatures, the magnetic moment (or total electronic spin) of the system may spontaneously change direction in a quantum process.[172,173] At higher temperatures, the spin direction will fluctuate due to thermal agitation. Meanwhile, the magnitude of the magnetic moment will decrease, and eventually vanish at the Curie temperature. However, spin dynamics in magnetic systems is still a topic of great theoretical interest and remains controversial.[169,170,171]

- **Configuration of sample**

One sample or configuration of the magnet is a particular assignment of spin values, say:

$$s_i = \pm 1 \tag{3.8}$$

in which each spin is set either "up" or "down." According to statistical mechanics, the average value of an observable is obtained by weighting each configuration with the Boltzmann factor, k_B. For example, the average magnetization at some fixed temperature T is given by:

$$\langle M \rangle = \frac{\sum_{configs} M e^{-E/k_B T}}{\sum_{configs} e^{-E/k_B T}} \tag{3.9}$$

- **Configuration space**

The total number of configurations of a system is enormous even for a small number of spins. For example, for a system with 20 shells, the layer number K_j (R / d) is about 5.0. The total spin number, N_j, is 555, and the

$$\text{No. of configs} = 2^{\mathrm{Nj}} = 2^{555} = 1.18 \times 10^{167} \tag{3.10}$$

If we enumerate the configurations at one billion per second on a very fast computer, it would take 1.18 × 10^{158} seconds, or 3.74 × 10^{150} years to compute the average magnetization exactly.

- **Probability distribution**

The basic idea of a Monte Carlo calculation is to generate a reasonable number of configurations at random. The Boltzmann factor is an exponential function of energy, which can vary enormously. The random configurations are therefore generated with probability determined by the following factor:

$$p(s_1, s_2, \ldots, s_{Ns}) = \frac{e^{-E(s_1, s_2, \ldots, s_{Nj})/k_B T}}{\sum_{configs} e^{-E/k_B T}} \tag{3.11}$$

- **Monte Carlo average**

The problem now is to generate N_j statistically independent configurations that are distributed according to the Boltzmann factor:

$$(s_1^{(i)}, s_2^{(i)}, \ldots, s_{Nj}^{(i)}), \qquad i = 1, 2, \ldots, N_j \tag{3.12}$$

The average magnetization and energy are given as:

$$\langle M \rangle = \frac{1}{N_j} \sum_{i=1}^{N_j} M\,(s_1^{(i)}, s_2^{(i)}, \ldots, s_{N_j}^{(i)}) \tag{3.13}$$

$$\langle E \rangle = \frac{1}{N_j} \sum_{i=1}^{N_j} E(s_1^{(i)}, s_2^{(i)}, \ldots, s_{N_j}^{(i)}) \tag{3.14}$$

3.2.3 The algorithm of Metropolis

For simplicity, the method to generate configurations distributed according to the Boltzmann factor that was proposed by Metropolis *et al*[174] was used in the simulation. According to this method, the algorithm generates the next configuration in the sequences as follows. Given a configuration, choose a spin s_i, let $s_{i,\text{trial}} = - s_i$, and compute the change in energy of the system:

$$\Delta E = E(s_1, s_2, \ldots, s_{i,trial}, \ldots, s_{N_j}) - E(s_1, s_2, \ldots, s_i, \ldots, s_{N_j}) \tag{3.15}$$

If

$$e^{-\Delta E / k_B T} > r \tag{3.16}$$

then flip this spin, let $s_i \leftarrow s_{i,trial}$, where r is a uniform random deviation. Repeating the above iteration for all N_S spins in the configuration, from a certain initial configuration, after a suitable number of Monte Carlo steps, the system can reach a thermally stable state and the statistical averages can be obtained. In this study, 5000 Monte Carlo steps are carried and it is enough to get the stable state.

3.2.4 Spin system

Six kinds of nanosolid systems have been employed to investigate the size and shape effect on the magnetization at various temperatures: fcc spherical particles, fcc rod, fcc plate, icosahedron particles, Marks decahedron particles, and fcc truncated octahedron particles.

The fcc spherical particles are formed such that layers of successive neighbors are added to an atom in the center. The example in Figure 3.3 shows two fcc spherical particles, N_{135} and N_{141}, with shell numbers $S = 8$ and 9 and diameters $K_j = 3.1$ and 3.3 in the unit of d, respectively. The oscillation of the number of atoms in the first out shell reflects the different degrees of structure openness. Here, only those clusters with complete shells were considered, as in Merikoski *et al.*[31] Table 3.1 shows the first 24 spherical particles.

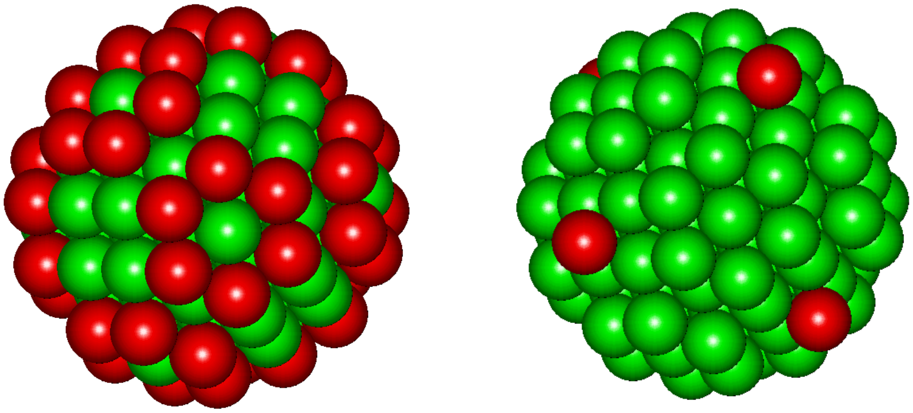

(a) N_{135}: $S = 8$, $K_j = 3.1$ (b) N_{141}: $S = 9$, $K_j = 3.3$

Figure 3.3 Example structure of fcc dot. The red atoms belong to the first out shell. The atoms in the first out layer of N_{141} are much fewer in number than those of particle N_{135}, indicating the oscillations of the surface state when a particle is growing up.

The rod and the plate spin systems are also formed based on the fcc lattice. The axis of the rod system is arbitrarily chosen <100> direction and the length is maintained at K_j = 28.3. The radius ranges from S = 1 to 11 (K_j = 0.5~3.66), as, for example, in Figure 3.4 (a), which shows an fcc rod with S = 3, K_j = 1.9. The orientation of the plate is also in <100> direction and the width and length are maintained at K_j = 28.3. The thickness ranges from S = 1 to 14 (K_j = 0.5~5.1), as shown in Figure 3.4 (b).

There are three main types of ordered structures: icosahedra, decahedra, and close-packed octahedra, which are favored by nanosolids from an energetic point of view (see Figure 3.5 (a)~(c) for N_{147}, N_{101}, and N_{201}). Icosahedra and decahedra are

Table 3.1 Magnetic nanoparticle systems for Monte Carlo simulation (R is the radius of the particle, N_i is the atomic number of ith shell, N_j is the atomic number of the whole particle, and z_i is the CN of the atoms in the ith shell).

Shell number	K_j (*R/d*)	N_i	$N_j = \sum N_i$	z_i(N_j=55)	z_i(N_j=135)	z_i(N_j=225)	z_i(N_j=683)
1	0.5	1	1	12	12	12	12
2	**1.49999**	**12**	**13**	12	12	12	12
3	1.914214	6	19	8	12	12	12
4	2.232058	24	43	7	12	12	12
5	**2.499981**	**12**	**55**	5	11	12	12
6	2.736084	24	79		8	12	12
7	2.949489	8	87		9	12	12
8	**3.145781**	**48**	**135**		6	10	12
9	3.328427	6	141			8	12
10	3.499971	36	177			7	12
11	3.662252	24	201			6	12
12	**3.816614**	**24**	**225**			5	12
16	4.500032	12	381				11
17	4.62314	48	429				11
18	4.742641	30	459				8
19	4.858889	72	531				8
20	4.972168	24	555				8
21	5.082547	48	603				7
22	5.190381	24	627				7
23	5.29581	48	675				6
24	**5.398977**	**8**	**683**				3

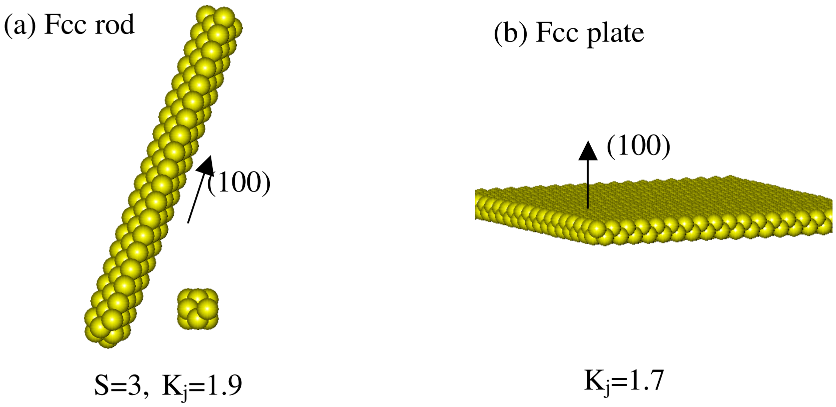

(a) Fcc rod

S=3, K_j=1.9

(b) Fcc plate

K_j=1.7

Figure 3.4 Fcc rod and fcc plate spin system.[175]

noncrystalline structures that cannot be found in bulk crystal because of their fivefold symmetry. Icosahedra are quasispherical structures, where atoms are arranged in concentric shells. They present six fivefold symmetry axes and have only (111) facets. Decahedra, which have a single fivefold axis, are less spherical than icosahedra. Their standard form contains a large amount of atoms set in (100) facets whose energy is higher than those set in (111) facets, and thus is not favored. The much more optimized form is Marks-truncated decahedra, where reentrant (111) facets are introduced via a modified-Wulff construction to optimize the nanosolids' energetic stability.

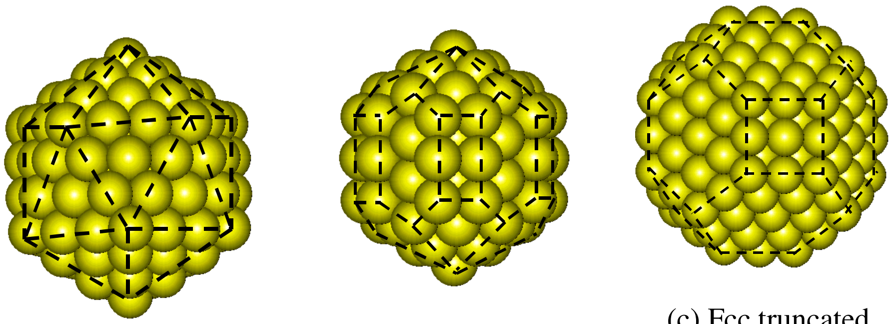

(a) Icosahedron N_{147}

(b) Marks decahedron N_{101}

(c) Fcc truncated octahedron N_{201}

Figure 3.5 The illustration of (a) Icosahedron N_{147}, (b) Marks decahedron N_{101}, and (c) fcc truncated octahedron N_{201}.[175]

Close-packed nanosolids, which own the crystalline structure, have even larger surface energy because of the wide-open (100) facets that are necessary to build up a quasispherical structure. In addition to the fcc spherical dot, three kinds of particles were used for MC simulations, as listed in Table 3.2. Appendix I is the Monte Carlo calculation code for simulating the size and temperature effect on the magnetic behavior of ferromagnetic nanosolids.

Table 3.2 Icosahedron, Marks decahedron, and fcc truncated octahedron particles used in MC simulation.

Icosahedron	Marks decahedron	Fcc truncated octahedron
N_{13}	N_{75}	N_{19}^{*}
N_{55}	N_{101}	N_{38}
N_{147}	$N_{318}^{\#}$	N_{79}
N_{309}	$N_{389}^{\#}$	N_{201}
		N_{225}
		N_{260}
		N_{314}
		N_{405}

Decahedron; * Fcc octahedron

3.3 Experimental details

3.3.1 Filtered Cathodic Vacuum Arc (FCVA) system

Figure 3.6 shows the FCVA system used for the film deposition. Figure 3.7 provides a schematic illustration of the off-plane double bend (OPDB) FCVA. The system mainly consists of three parts: a cathodic arc source, a plasma-filtering duct, and a deposition chamber. A rotary-cryogenic pump system is connected to the chamber for pumping down to the desired pressure during the deposition. The cathodic vacuum arc source has five main parts: the anode wall, the power supply, the arc trigger, the target, and the target cooling system. Before deposition, the

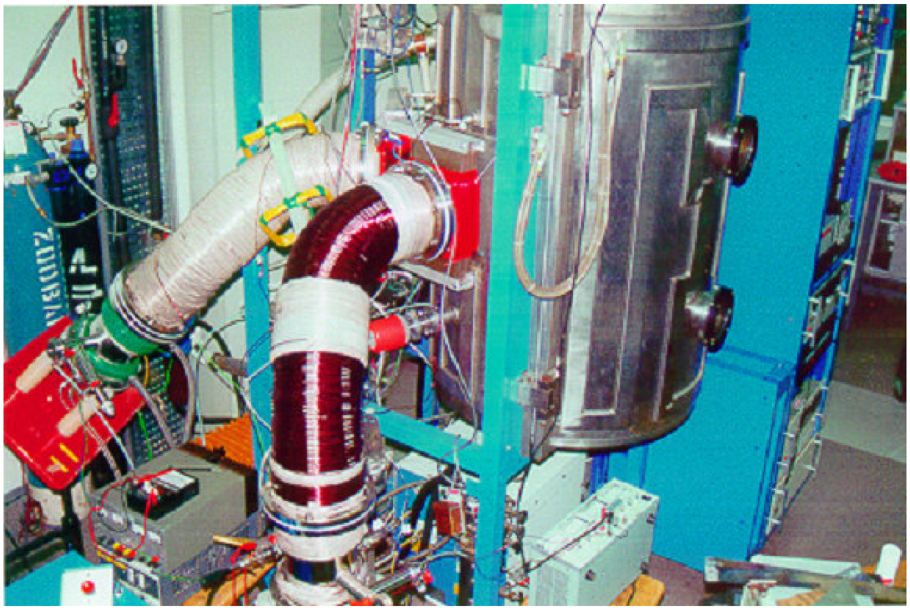

Figure 3.6 The FCVA system with two six-inch diameter OPDB filters (R&D)

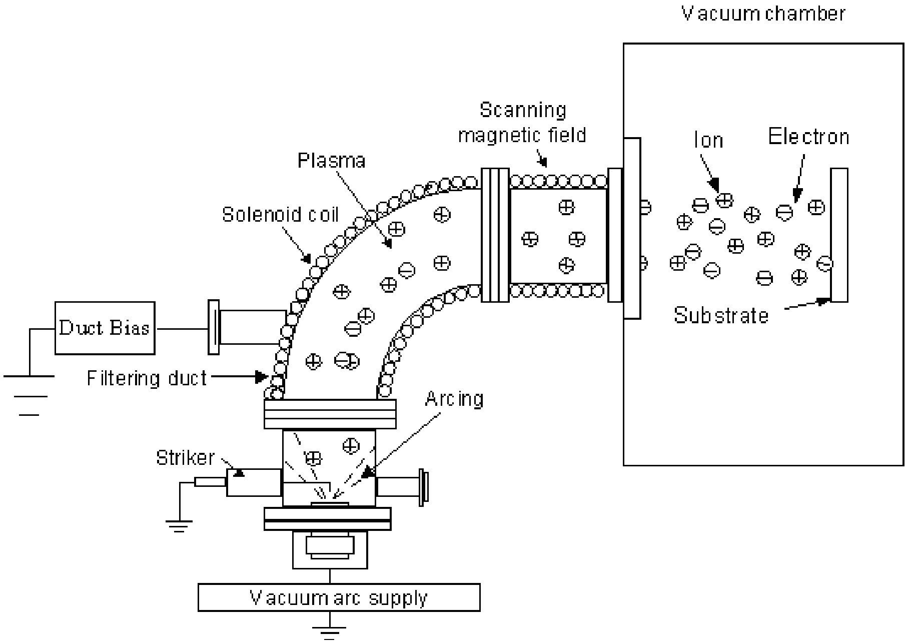

Figure 3.7 Schematic illustration of the FCVA system

chamber is prepumped down to a pressure less than 10^{-5} torr. The power supply is an electrical welding machine with a maximum current of 250 A. The anode is grounded (deposition chamber) and the cathode is connected to the target. A radial

electric field is formed via the toroidal duct, coupled with a curvilinear axial magnetic field on the curved toroidal duct that forms a crossed electric-magnetic field filtering assembly. The plasma, which is steered by the field, passes through the duct to the substrate and results in the deposition of films free from any unwanted macroparticles and neutral atoms. The ions are highly energetic, with kinetic energies typically of 50-150 eV, which is considerably higher than those of the evaporated or sputtered atoms, even though the discharge voltage is only around 20 V. The high ionization facilitates controlling the energy of the depositing ions by biasing the substrate which has a strong influence on the microstructure of the coating, while the high energy results in self-cleaning of the substrates of contaminants by ion sputtering. The high flux results in a high deposition rate which is economically favorable. The FCVA technique combined with an OPDB filter has the following advantages over other deposition techniques:

a) The working pressure is very low (below 1×10^{-5}), which results in a clean deposition.
b) The OPDB filter enables high-quality, macroparticle-free film deposition.
c) The ion energy is high and adjustable.
d) The deposition rate is high.

3.3.2 Shield for magnetic target

Generally, for nonferromagnetic metal and carbon targets, the arc is easy to be maintained in a stable state, while for the ferromagnetic metal target, the arc is unstable because the high permeability of the target changes the distribution of the magnetic field around the cathode. When the ferromagnetic target is used, the magnetic flux concentration at the edge of the target is high, resulting in the arc point's running around the edge of the target during sputtering. This extinguishes the arc after a short time. To solve this problem, a shield is designed and applied around the target,[176] as shown in Figure 3.8. The shield for the cathode consists of

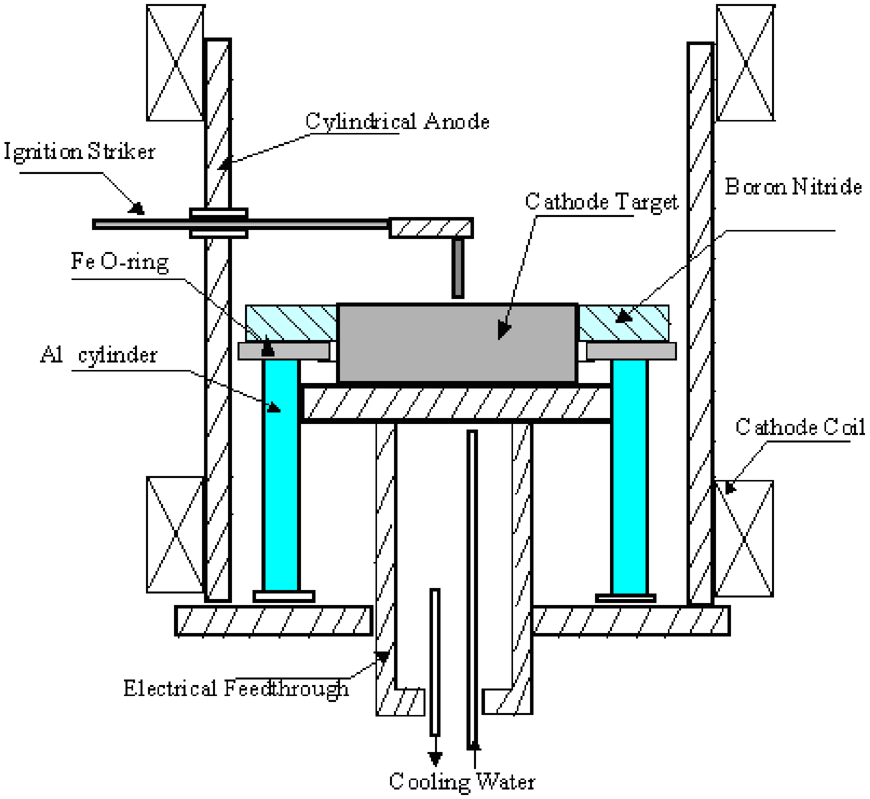

Figure 3.8 Schematic illustration of the modified cathode for the magnetic target. The cathode consists of the target and its supporter with a water-cooling system. The shield consists of three main parts: the aluminum cylinder, the pure iron O-ring, and the BN O-ring.[177]

three main parts: the aluminum cylinder, the pure iron ring, and the BN O-ring. The metal cylinder covers the cathode target and the copper supporter near the cooling water systems. The outer bend wall is connected to the anode. The shield is in a floating potential that separates the electrical field between the cathode and the anode into two parts. The configuration prevents the plasma from being formed in this area. The ring of pure iron provides a larger virtual target surface, which results in a stable arc spot. The BN O-ring is set on top of the aluminum cylinder. The inner diameter of the BN O-ring is 60 mm, which can shield the target well and stop the arc from being extinguished. Furthermore, the BN O-ring possesses very low surface energy that facilitates the erasure of the residua after deposition.

The target surface that does not have the shield is consumed at the edge, while the target surface with the shield is consumed from the center of the top surface, indicating the effectiveness of the shield, as shown in Figure 3.9.

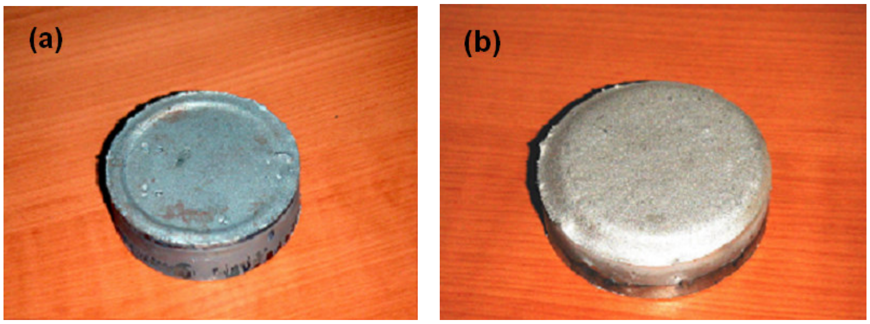

Figure 3.9 Magnetic targets (a) with and (b) without using the designed shield.

3.3.3 Sample preparation

- Nickel thin films

Ni thin films with different thickness and grain sizes were deposited on Si(001) substrates using the FCVA technique by controlling the substrate temperature from 100 to 400°C. The magnetic properties were studied to verify the size effect on the magnetization at room temperature. Ni was chosen instead of Fe because Ni has relatively high oxidation resistance compared with Fe. A pure nickel cylinder (99.9%) with dimensions of $\phi 60 \times 20$ mm was mounted on the water-cooled copper support as the cathode target. The arc current was maintained at 120 A. The basic vacuum was around 1×10^{-5} torr. The films thickness was below 124 nm.

- Fe-N thin films with various nitrogen concentrations

Fe-N films with various nitrogen concentrations were deposited to investigate the nitridation effect on the M_S of iron films. Three approaches were applied to obtain the nitrogen concentrations: (i) The nitrogen gas was input directly into the chamber. Experimental results showed that only α-Fe(N) phase was formed in the iron films with very low nitrogen concentration. (ii) Nitrogen was introduced into the plasma area on top of the iron target. Nitrogen-poor phases were formed in the films using this approach. (iii) A linear ion beam source (D.C. 2.5×20 cm^2) was introduced into the chamber to produce dense nitrogen ions. The nitrogen ions, together with the iron plasma produced by the cathode source, reached the substrate and formed the ion-assisted FCVA deposition. Nitrogen-rich phases such as FeN were obtained in the films. The details of the deposition conditions are listed in Table 3.3. The three aforementioned deposition methods are illustrated in Figure 3.10. Using these approaches, the nitrogen partial pressure (P_N) and the argon to nitrogen ratio (P_N : P_{Ar}) can be controlled, and hence Fe-N films with different nitrogen concentrations can be produced. During the deposition, the substrate temperature was maintained at around 150°C. The arc current was maintained at 120 A.

Table 3.3 Film deposited with various nitrogen concentrations.

Approach for N introduction	Sample No.	Working pressure (torr)	P_N : P_{Ar}
I: Deposition chamber	I-1	2.0×10^{-4}	100:0
II: Plasma area in cathode source	II-1	2.0×10^{-4}	100:0
	II-2	1.5×10^{-4}	100:0
	II-3	1.0×10^{-4}	100:0
	II-4	0.7×10^{-4}	100:0
III: Ion beam source	III-1	2.2×10^{-4}	100:7
	III-2	2.0×10^{-4}	80:7
	III-3	1.8×10^{-4}	50:7
	III-4	1.6×10^{-4}	40:7
	III-5	1.4×10^{-4}	30:7
	III-6	1.2×10^{-4}	20:7
	III-7	1.0×10^{-4}	10:7

- α-Fe(N) films under various bias voltages

For FCVA deposition, the plasma that reaches the substrate is highly ionized and free of macroparticles and neutral atoms, which facilitate a deposition with controllable ion energy. The intrinsic energy of ions emitted from a cathode source is considerably higher than that of evaporated or sputtered atoms. The energy of ions is a very important parameter during the deposition, which affects the films in terms of deposition rate, surface morphology, microstructure, magnetic properties, and so forth. To systematically study the bias effect on the properties of iron nitride films, α-Fe(N) films were deposited at bias voltages of 0, –50, –100, –200, and –400 V by maintaining the working pressure at 5 × 10^{-5} torr and P_{N2} : P_{Ar} = 100:0.

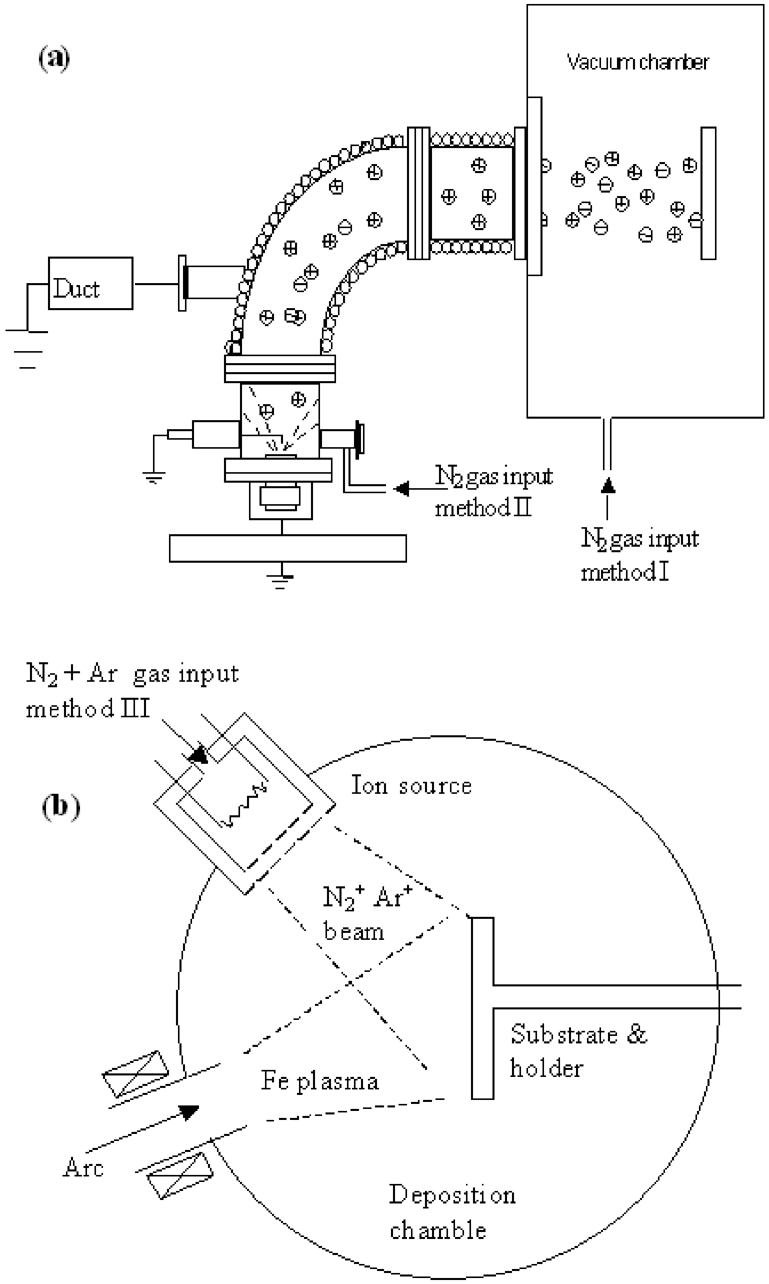

Figure 3.10 The three approaches introducing nitrogen gas: (I) nitrogen is introduced directly into the chamber; (II) nitrogen is introduced into the plasma region near the target; and (III) nitrogen is introduced into the linear ion beam source.[178]

- Fe-N films of various grain sizes

The combining effects of physical size and nitrogen catalysis were examined by introducing different nitrogen concentrations and controlling different grain sizes on the Fe-N films. The films with low nitrogen content were deposited using approach II at a nitrogen flow rate of 50 sccm. The films with high nitrogen content were deposited using approach III with N_2:Ar = 50:7 and a working pressure of 1.8×10^{-4} torr.

The substrate temperature varied from 100 to 400°C.

Table **3.4** summarizes the deposition conditions of the Fe-N samples together with the pure iron films. The films thickness is ~80 nm.

Table 3.4 Deposition conditions of Fe-N films at various substrate temperatures.

Series	Nitrogen introducing approaches	Working pressure	Substrate temperature (°C)
Pure iron (Fe)	-	1.0×10^{-5} torr	110 230 350
Nitrogen poor: Fe-(N-Poor)	Approach II	1.0×10^{-4} torr	110 170 230 290 350
Nitrogen rich: Fe-(N-Rich)	Approach III	1.8×10^{-4} torr	100 200 300 400

3.3.4 Characterization methods

- *Thickness*

The Surface Profile Measuring System (TENCOR P-10) was used to measure the thickness of the films. Before deposition, marks were made on the surface of the substrate by a sign pen. After deposition, film deposited on the marked part was removed, which formed a steep step for thickness measurement. The area of the sample for magnetic measurement was also obtained from the surface profile measuring system. The value of the rectangular coordinate for each point of the polygon was measured and the area was then calculated.

- *Surface morphology*

Atomic Force Microscopy (AFM) (Dimension 3000 Scanning Probe Microscope, Digital Instruments) was used to measure the surface morphology of the films. The Root Mean Square (RMS) roughness was obtained from the digital image-processing package of the AFM system.

- *Microstructure and grain size*

The microstructures of the films were characterized using the Siemens D5005 X-Ray diffraction (XRD) with a glancing incident mode by using CuKα (λ = 0.154 nm) radiation (40 kV, 40 mA). The incident angle was fixed at 1°, the 2θ scanning step size was set at 0.05°, and the counting time at each step was 2 s. The grain size was calculated from the full width at half maximum (FWHM) of the peak (radians) using Scherrer's equation: $t = C\lambda/B\cos\theta$, where λ is the x-ray wavelength (nm), B is the FWHM of the peak (radians) corrected for instrumental broadening, θ is the Bragg angle, C is a factor (typically 1.0) that depends on the crystallite shape, and t is the crystallite size (nm).

- *Binding energy and nitrogen concentration*

The binding energy and the nitrogen concentration were characterized by X-ray photoelectron spectroscopy (XPS). The XPS analysis was performed using a Kratos-Axis spectrometer with Dual-Anode Al Kα (1486.6 eV) X-ray radiation

(150W, 15 kV, and 10 mA) and a hemispherical electron energy analyzer. The base pressure of the chamber was 2 x 10^{-9} torr. The survey spectra in the range of 0-1100 eV were recorded in 1 eV step for each sample, followed by high-resolution spectra over different element peaks in 0.1 eV step, from which the detailed composition was calculated. Curve fitting was performed after a Shirley background subtraction by nonlinear least square fitting using a mixed Gauss/Lorentz function. To remove the surface contamination layer, Ar ion bombardment was carried out for 480 seconds using a differential pumping ion gun (Kratos MacroBeam) with an accelerating voltage of 4 keV and a gas pressure of 1 x 10^{-7} torr. The bombardment was performed at an angle of incidence of 45^{o} with respect to the surface normal.

- *Magnetic properties*

The Vibrating Sample Magnetometer (VSM) was used to measure the magnetic properties of the films. The output of the VSM is a hysteresis loop. The VSM measures the total magnetic moment, m_{emu}, of a sample in emu (electromagnetic unit), and this result may be related to the sample magnetization using the definition of the emu: 1 emu = 1 Gauss·cm^3. The magnetization, M, is determined by dividing the sample moment, m_{emu}, by the sample volume, V, as shown in: M (Gauss) = m_{emu} (emu = Gauss·cm^3) / V (cm^3).

CHAPTER 4 RESULTS AND DISCUSSION I: PHYSICAL SIZE EFFECT

In this chapter, the physical size effects are introduced in four sections. In the first section, theory analysis and prediction for the size-induced M_S shift and T_C suppression are presented by incorporating the BOLS correlation prediction into the Brillouin equation and Ising model. In the second section, simulation results obtained from the MC calculation on the spin systems with various physical sizes and geometrical shapes are shown. Both the M_S shift at various temperatures and the T_C shiftare exhibited. The third section describes how the Ni films with various grain sizes that are deposited using the FCVA technique. The size effects on the M_S and H_C at ambient are introduced. In the last section, the model of T_C suppression for ferromagnetic nanosolids is extended to ferroelectrical and superconductive nanosolids by considering the high order of CN imperfection in the BOLS correlation mechanism.

4.1 BOLS prediction

4.1.1 M_S variation

- **Enhancement of surface magnetic moment**

The spin distribution is based on the Hund's rules, which are a set of guidelines for finding the lowest energy state of an atom. The rules are empirical but have theoretical justification in quantum mechanics.

Hund's first rule asserts that the state with the highest spin has the lowest energy; when several states have the same spin, the state with the highest orbital angular momentum has the lowest energy. Hund's second rule is that, in the lowest energy state of a shell that is less than half full, J has its maximum value.[179] Hund's first rule requires that the spin is maximized, so that for an Fe atom ($3d^6 4s^2$), there are five electrons on the 3d spin-up levels, two occupying the 4s levels, and the rest on the 3d spin-down levels. The spin quantum number $S = 4 \times ½ = 2$. The angular momentum quantum number $L = 2 + 2 + 1 + 0 + (-1) + (-2) = 2$. Hence, the total angular momentum $J = S + L = 4$. The Lande's g-factor is calculated by the following expression:[179]

$$g_J = 1 + \frac{J(J+1) + S(S+1) - L(L+1)}{2J(J+1)} \tag{4.1}$$

For an Fe atom, it is easy to get $g_J = 3/2$. The magnetic moment can then be calculated as follows:[179]

$$\mu_J = g_J \sqrt{J(J+1)}\mu_B = 6.7\mu_B \tag{4.2}$$

The maximum magnetic moment in the direction (z axis) of the applied magnetic field is: $\mu_{Jz} = g_J J \mu_B = 6\mu_B$. However, in the bulk, the situation changes because the L-orbital is frozen, $L = 0$.[179] When the metal atoms come closer together, the discrete localized atomic orbitals become delocalized, resulting in cohesion of the atoms, and the discrete atomic levels disperse in energy, giving rise to energy bands. In the bulk, each atom contributes (essentially) one electron to the 4s band (in contrast to the atom). The 3d electrons remain reasonably localized and retain much of their atomic character. Following an approximation carried out by Billas *et al*,[50] we assume that the 3d orbitals are not delocalized at all and hence the 3d metals are atom-like. In that case, the 3d spin-up band is fully occupied (with five electrons per atom) and has two spin-down electrons per atom. The spin imbalance is simply the difference in the number of spin-up and spin-down 3d electrons per atom. Consequently, the magnetic moment per atom for Fe is 3 μ_B. This has been measured by Billas *et al.*[50]

Different from the bulk picture, clusters have a large portion of atoms on the surface where the electronic structure is different. This is due to the reduced number of nearest neighbors, which causes the 3d electron to be more localized.[180] The BOLS correlation mechanism, as described in section 3.1.1, indicates that the CN imperfection of an atom at the surface or at the site surrounding the defect causes the remaining bonds of the lower-coordinated atom to contract spontaneously, which is associated with a magnitude increase of the bond energy or potential well deepening. Consequently, the binding energy density in the relaxed region is higher than that in the bulk region, while the cohesive energy ($E_{coh,i} = z_i E_i$) of the lower-coordinated (z_i) atom is weakened, though the individual bond energy is increased. As illustrated in Figure 3.1, the CN imperfection-enhanced bond-energy deepens the atomic trapping potential well of the low-CN atom from E_b to $E_i = c_i^{-m} E_b$ compared with the bulk value. Electrons surrounding the lower-CN atom are more localized in the relaxed surface region and hence contribute to the J_i of the lower-coordinated atom. If the localization probability is proportional to the well depth, then the densely localized electrons contribute to the J_i in the following way:

$$\frac{J_i(z_i)}{J_b} \propto \frac{\mu_i(z_i)}{\mu_b} \propto \frac{E_i}{E_b} = c_i^{-m} \tag{4.3}$$

The magnetic momentum in the direction of the applied field is $\mu_{iz} = Jg_J\mu_B$, where $\mu_i(z_i)$ and μ_b represent the magnetic moment of an atom with z_i at surface sites and an atom in the bulk situation, respectively. Note that the Lande's *g*-factor (g_J = 1~2) is a function of the orbital and spin angular momentum, as shown in Eq (4.1), which is also affected by the CN imperfection. In the first-order approximation, this effect is neglected that may influence the precision of *m* parameterization. As such, for an atom on a flat surface with $z_i = 4(c_1 = 0.88)$, the μ_i increases by $1\text{-}0.88^{-1}$ = 12%, which is similar to the cases of Fe-W,[181] Fe-Fe, and Ni-Ni,[57] where the interlayer distance contracts by 10-12%, which is associated with a 15~29% enhancement of the μ_i. For a dimmer, $z_i = 2$, $c_i = 0.7$, the μ_i is enhanced by 40%, which agrees with the reported value of 3.2/2.22 for Fe, for example. If the effect of atomic CN imperfection and the pronounced portion of the lower-coordinated atoms in the nanosolid are taken into consideration, the magnetic properties of the ferromagnetic nanosolids should differ from those of the bulk.

For a spherical dot, $z_1 = 4(1 - 0.75/K_j)$, $z_2 = 6$, and $z_3 = 8$ for the first three surface layers worked sufficiently well in predicting the size dependence of a nanosolid.[182] The mean angular momentum $J(K_j)$ of an atom in the nanosolid and its relative change can be obtained by:

$$\begin{aligned} N_j J(K_j) &= N_j J + \sum_{i\le 3} N_i\left(J_i - J\right) \\ \frac{J\left(K_j\right) - J}{J} &= \sum_{i\le 3} r_i\left(c_i^{-m} - 1\right) \end{aligned} \tag{4.4}$$

The *i* is counted from the outermost layer to the center of the solid up to 3 as no CN imperfection is expected for *i* > 3.

- **Exchange energy weakening**

The M_S of the material is not only affected by the magnetic moment of an individual atom but also by the order of the spins, which depends on the vibrational energy and the exchange energy, H_{ex}, or the atomic cohesive energy, E_{coh}. The H_{ex} can be expressed using the Ising model under a zero magnetic field:[183]

$$H_{ex} = \sum_{<i,j>} J_{ij} S_i \cdot S_j \propto z_i r_{ij}^{-m} \tag{4.5}$$

S_i and S_j are the spin operator, or the total angular momentum, of atoms in site i and site j, respectively. $J_{ij} \propto r_{ij}^{-m}$ is the spin-spin exchange-coupling coefficient between the two sites. The H_{ex} is a sum of J_{ij} over all the possible z_i of the considered atom.

The reduction of size affects the exchange energy in two aspects: (1) the increase of exchange energy for a single exchange bond caused by the bond contraction; (2) the reduction of the number of exchange bonds. Based on the BOLS mechanism, the size-induced change of the H_{ex} is derived as:

$$\begin{aligned}\frac{H_{ex}(K_j) - H_{ex}(\infty)}{H_{ex}(\infty)} &= \sum\nolimits_{i\le 3} \frac{N_i}{N_j}\left(\frac{z_i d_i^{-m} - z_b d^{-m}}{z_b d^{-m}}\right) \\ &= \sum\nolimits_{i\le 3} \gamma_i (z_{ib} c_i^{-m} - 1)\end{aligned} \tag{4.6}$$

The interspin interaction controls the order of the spin system, which determines the M_S. At low temperatures, the magnetic moment (or total electronic spin) of the system may spontaneously change direction in a quantum tunneling process.[173] At higher temperatures, the spin direction will fluctuate due to thermal agitation. Meanwhile, the magnitude of the magnetic moment will decrease, and eventually vanishes at the Curie temperature (T_C). The M_S of the system is determined by the sum over states of the spins, or the order of the spins. It is easy to understand that if one needs to disorder the spin-spin interaction by applying thermal stimulus, one has to provide sufficient energy to loosen all the bonds of the atom and to promote the atomic vibration. The exchange energy, or the exchange interaction, of a specific atom with z_i coordinates is the sum of all the bond energy, as given in Eq (4.6).

- ***Brillouin function – Ms(T, K$_j$)***

It is common to use the concept of "molecular field" to approach the spontaneous magnetization at T in terms of the Brillouin function, $B_J(y)$, for a bulk:[179]

$$\begin{aligned} M(T) &= g_J J \mu_B B_J(y) \\ B_J(y) &= \frac{2J+1}{2J}\coth\frac{2J+1}{2J}y - \frac{1}{2J}\coth\frac{y}{2J} \\ y &= \frac{J g_J \mu_B}{k_B T} H_m \end{aligned} \tag{4.7}$$

where J is the mean angular momentum and H_m is the molecular/crystal field. When the temperature $T < 0.8T_C$, $M_S(T) \approx M(T)$.[179] The H_m is proportional to the exchange energy, $H_m = AE_{exc}$, or the cohesive energy, where A is a constant. Therefore, replacing the mean J in a bulk with the size-dependent $J(K_j)$, the temperature and size dependence of the $M_S(K_j, T)$ is derived as:

$$M_S(K_j,T) = N_j g_J J(K_j)\mu_B \left\{ \frac{2J(K_j)+1}{2J(K_j)} \coth\left[\frac{(2J(K_j)+1)g_J\mu_B}{2k_BT} AE_{exc}(K_j) \right] - \frac{1}{2J(K_j)} \coth\left[\frac{g_J\mu_B}{2k_BT} AE_{exc}(K_j) \right] \right\} \tag{4.8}$$

where:

$$E_{exc}(K_j) = E_{exc}(\infty)\left[1 + \sum_{i\le 3} \gamma_{ij}(z_{ib}c_i^{-m} - 1) \right] \tag{4.9}$$

$$J(K_j) = J\left[1 + \sum_{i\le 3} r_{ij}\left(c_i^{-m} - 1\right) \right] \tag{4.10}$$

$E_{exc}(K_j)$ and $J(K_j)$ are the size-dependent exchange energy and the mean angular momentum of the nanosolid. Note that Eq (4.8) does not apply to an isolated atom without exchange interaction, though an isolated atom possesses intrinsic magnetic momentum.

The temperature and size dependence of M_S expressed as in Eq (4.8) is illustrated in Figure 4.1, where M_S is normalized by $M_S(T = 0, K_j = \infty)$ and T is normalized by $AE_{exc}(\infty)$. No oscillatory features are given as a smooth function in Eq (4.8) for the S/V ratio is used. The figure shows that, with the decrease in size, the M_S increases at low temperature while decreasing at high temperature, which indicates that at low temperature, the enhancement of the surface magnetic moment exhibits a dominant contribution for the M_S, while at higher temperature, the reduction of exchange energy exhibits a dominant contribution for the M_S. Note that Figure 4.1 shows only the M_S behavior of spherical dots of different K_j. For those particles with more opening surface, especially for the

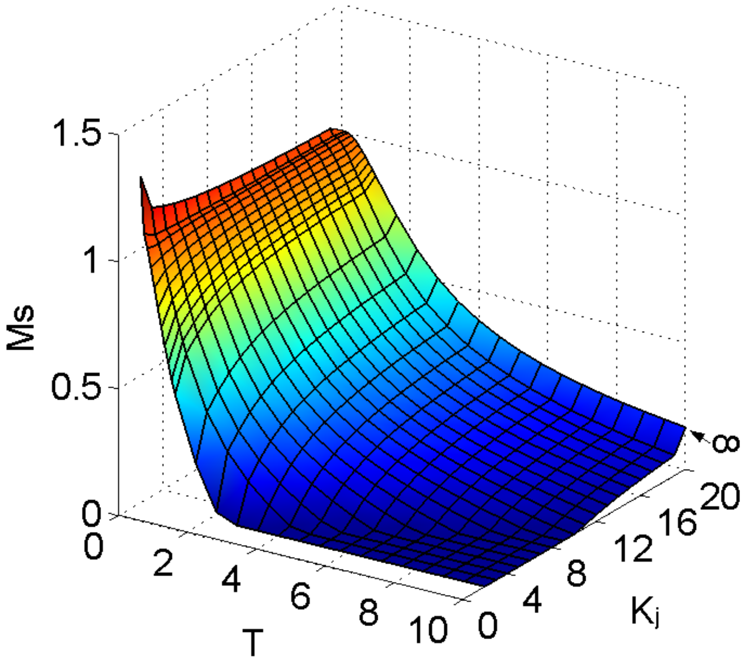

Figure 4.1 Counter plot of the BOLS predicted (see Eq (4.8)) M_S(T, K_j) for dot/particle, which shows that the M_S increases inversely with size at low temperature and decreases with size at mid-temperature. The M_S is normalized by $M_S(T = 0, K_j = \infty)$ and T is normalized by $AE_{exc}(\infty)$.[175]

dimmer structure, the CN of surface atoms is much lower and the magnetic moment is therefore much higher than that shown here. As a result, the M_S at low T should be higher than the result shown in Figure 4.1.

4.1.2 T_C suppression

The Curie temperature is the temperature point at which the thermal vibrational energy overcomes the exchange energy. It is understandable that the total energy of a single bond is composed of two parts:

$$E_{total}(d, T_C) = E_b(d) + E_V(T_C) = E_C \tag{4.11}$$

The $E_b(d)$ is the binding energy at equilibrium atomic separation that is independent of the particular forms of the pair-wise interatomic potential. The $E_V(T)$ is the thermal vibrational energy. At the Curie point, the thermal vibration energy required to disorder the spin-spin exchange interaction is close to the exchange energy. Taking $E_{\text{total}}(d, T) = E_C$ as the reference point (= 0), we have:

$$E_b(d) + E_V(T_C) = 0 \tag{4.12}$$

Figure 4.2 illustrates the BOLS correlation mechanism for T_C suppression. The separation between E = 0 and E_C may vary from material to material, but it is constant for all bonds of a specific material. The distance between E_C and the minimal bond energy at equilibrium atomic separation ($E_b(d_i)$, $E_b(d)$) determines the thermal energy that causes the order-disorder transition. Based on the mean field approximation and Einstein's relation,[86,184] Eq. (4.12) leads to

$$\begin{aligned} & -J_{ij} \times S \times (S+1) + k_B T_c = 0, \\ & and, \\ & T_C \propto J_{ij} \propto d_i^{-1} \end{aligned} \tag{4.13}$$

where S is the spin momentum. J_{ij} relates to the inverse equilibrium atomic separation. The atomic cohesive energy is given as in equation (4.14):

$$E_{coh,i} = \sum J_{ij} \propto z_i d_i^{-1} \tag{4.14}$$

Considering the BOLS correlation in the surface region of a nanosolid containing a total atom number of N_j with radius R, the total cohesive energy (exchange energy) of the entire nanosolid is the sum over all the atoms. A shell structure is used to incorporate the CN imperfection in the first three atomic layers:

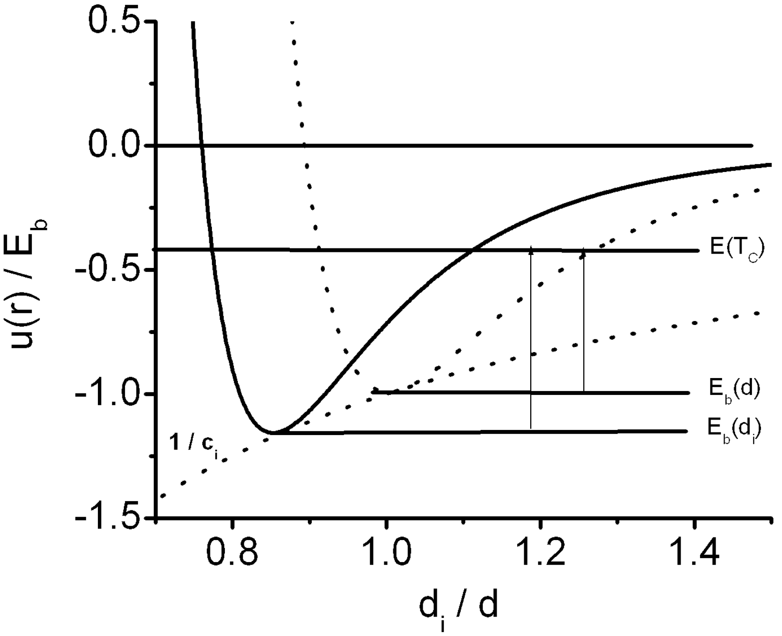

Figure 4.2 The typical pair-wise potential for interatomic interaction. The BOLS correlation mechanism indicates that the bond length decreases with the CN of an atom at the surface with a response of a bond energy rise (in absolute value). The $E(T_C)$ corresponds to the total energy at T_C. The separation between E_b = 0 and $E(T_C)$ is constant for all the bonds for a specific material and the separation between $E_b(d)$ at the equilibrium atomic distance and $E(T_C)$ is the thermal energy required to disorder the spin-spin interaction.[158]

$$E_{coh}(D) = N_j z E_b + \sum_{i\le 3} N_i \left(z_i E_i - z E_b\right) \tag{4.15}$$

where N_i is the atom number of the ith surface layer, which contributes to the S/V ratio: $\gamma_i = N_i/N_j$. The term $N_j z E_b$ is the cohesive energy of the entire solid without the effect of CN imperfection being involved. The relative change of the cohesive energy of a nanosolid, or the mean value change of a single atom, follows:

$$\frac{\Delta E_{coh}(R)}{E_{coh}(\infty)} = \sum_{i\le 3} \frac{N_i}{N_j}\left(\frac{z_i E_i - z E_b}{z E_b}\right) = \sum_{i\le 3} \gamma_i \left(z_{ib} c_i^{-1} - 1\right) \tag{4.16}$$

Eq. (4.16) indicates that the relative change of the cohesive energy of a nanosolid originates from the difference in the E_{coh} between a surface atom and a bulk atom, $z_{ib}c_i^{-1}$-1, due to the BOLS correlation. The trend of the change depends on the portion of surface atoms, γ_i, in the first three atomic layers with an appreciable degree of CN imperfection.

A calculation based on Eq (4.16) was carried out with the following parameters:[165] z_{1b} = 1/3, z_{2b} = 1/2; d_{Co} = 0.125 nm, d_{Fe} = 0.126 nm, d_{Ni} = 0.124 nm. $T_{C,Fe}(\infty)$ = 1043 K, $T_{C,Co}(\infty)$ = 1395 K, $T_{C,Ni}(\infty)$ = 631 K, respectively.[158]

Figure 4.3 compares the predicted with the experimentally observed T_C suppression of Fe, Co, and Ni thin films. Figure 4.4 shows the results for Fe_3O_4 nanoparticles.[79] The model prediction matches well with the measurements. For ultra-thin films, the measured data are closer to the predicted curve for the spherical dot. This indicates that at the beginning of film growth, the films prefer to grow in an island pattern and transform gradually into a continuous plate. The slight difference between predictions and observations at small K_j values can be minimized by adjusting the c_i value. In the calculation, z_{1b} = 1/3 is used as a standard, corresponding to c_1 = 0.88. In fact, the z_{ib} should decrease with the particle size as the curvature of the surface increases. On the other hand, the bond contraction coefficient also varies from source to source. For instance, the bond length between Ag, Cu, Ni, and Fe atoms and their neighbors were found to decrease with decreasing coordination. The bond lengths of the dimmer (2.53, 2.22, 2.15, and 2.02 Å, for Ag, Cu, Ni, and Fe, respectively[164]) are shorter than the

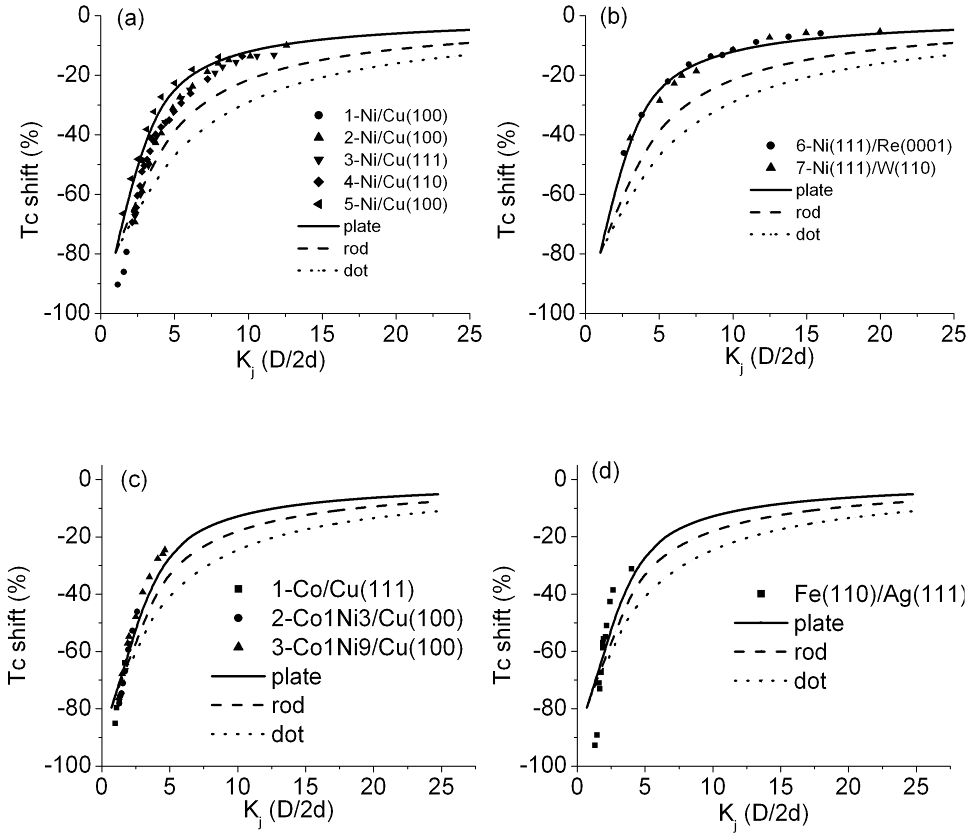

Figure 4.3 Comparison of the predicted T_C suppression (solid, dash and dot line) with observations (sporadic symbol) of (a) Ni thin films: data 1,[15] data 2, 3, 4,[86] data 5,[85] data 6,[76] and data 7[14]; (b) Co films;[12] and (c) Fe films.[10]

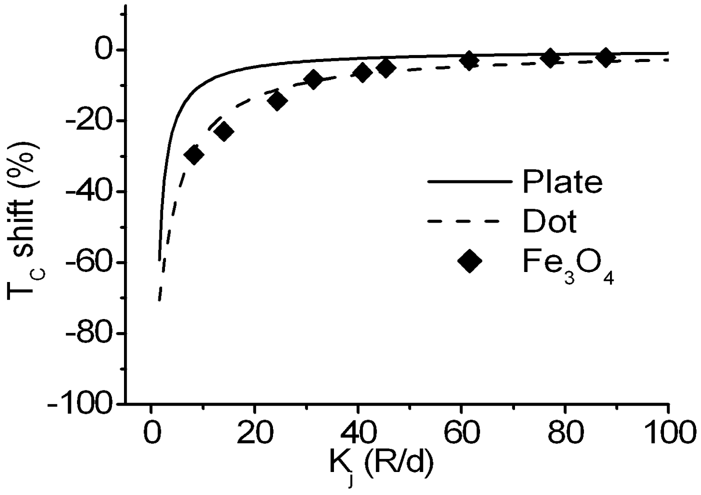

Figure 4.4 Comparison of the predicted (solid and dash line) and the measured T_C suppression of Fe_3O_4 nanoparticle (square symbol).[79]

nearest-neighboring distance in their respective bulk values by 12.5% for Ag, 13.2% for Cu, 13.6% for Ni, and 18.6% for Fe.[185] Therefore, a decrease of exchange energy at a surface has an enormous effect not only on the magnetization but also on the transition of a ferromagnetic nanosolid. It is our opinion that knowing the origin of the T_C suppression is much more important than getting the precise fitting of the experimental data, which can easily be reached by adjusting the parameters.

4.2 Monte Carlo simulation

In order to examine the model consideration described above, MC simulation was carried out based on the BOLS-incorporated Ising convention. The enhanced surface magnetic moment was taken into consideration by varying the spin value, S_i, for each atom. Six kinds of nanosolids, as described in section 3.2.4, were considered in MC simulation to investigate the size, shape, and structure effect on the M_S at various temperatures.

Figure 4.5 shows the MC-simulated $M_S(K_j, T)$ curves at zero applied magnetic field for (a) fcc dot, (b) fcc rod, (c) fcc plate, and (d) Icosahedra spin systems. The figures exhibit three outstanding regions with the increase in temperature. Generally, in the low-T region ($k_BT/J_{exc} < 3$), the M_S increases when the solid size is reduced. In the mid-T region (k_BT/J_{exc} ~6), the M_S drops with the solid size. At high T ($k_BT/J_{exc}>9$), in the paramagnetic region, the residual M_S increases as the size is reduced. These features are intrinsically common and depend less on the shape and structure of a specific solid. Figure 4.6 shows the

$M_S(K_j, T)$ at k_BT/J_0 = 1, 6, and 12, which are the typical temperatures in the three regions.

4.2.1 $M_S(K_j, T)$ enhancement at Low T

It can be seen from Figure 4.6 (a) that for a specific size, K_j, the M_S of the fcc dot is higher than that of the fcc plate because an fcc dot has a higher γ_{ij} value than the fcc plate. In this region, the M_S increase inversely with size; the tendency is consistent with most of the experimental observations of size-induced enhancement of M_S at low temperatures.[10,44,50,67,68] It is understood that when the temperature is very low, $T \rightarrow 0$ K, $y \rightarrow \infty$, and then $B_J(y) \rightarrow 1$. Eq. (4.8) can then be approximated as: $M_S(T \rightarrow 0) = NJg_J\mu_B$. g_J and J follow Eqs (4.1) and (4.10), respectively. Using a shell structure in the BOLS correlation that calculates the magnetic moment of every atom layer by layer leads to the size-enhanced M_S for a nanosolid at very low temperature:

$$\frac{\Delta M\left(K_j, T \rightarrow 0\right)}{M_b} = \sum_{i \le 3} r_i \left(c_i^{-m} - 1\right) \tag{4.17}$$

Agreement of MC simulations and BOLS calculations as well as the observed trends confirms the validity of the BOLS consideration that the M_S enhancement is dominated by the strongly localized electrons in the relaxed surface region.

4.2.2 $M_S(K_j, T)$ tailoring at mid-T

In the second region, as shown in Figure 4.6 (b), the $M_S(K_j, T)$ decreases with particle size in the vicinity of T_C. In this region, the decrease of exchange energy overcomes the size effect on the surface magnetic moment. With the increase of temperature, the thermal vibrational energy increases. The magnetization is hence not only affected by the individual magnetic moment of each atom but also by the order of the spins. The exchange energy of a small spin system is lower than that

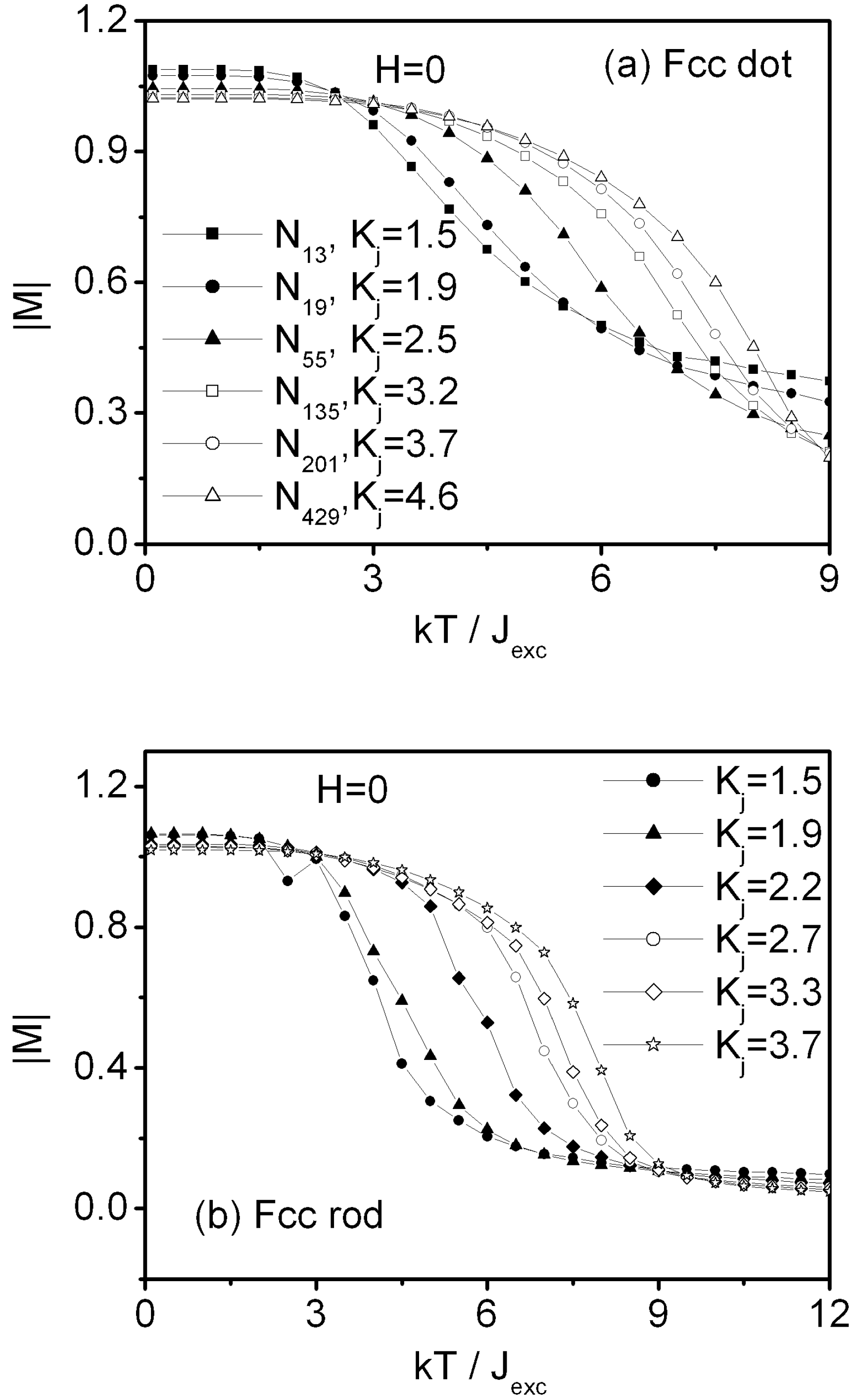

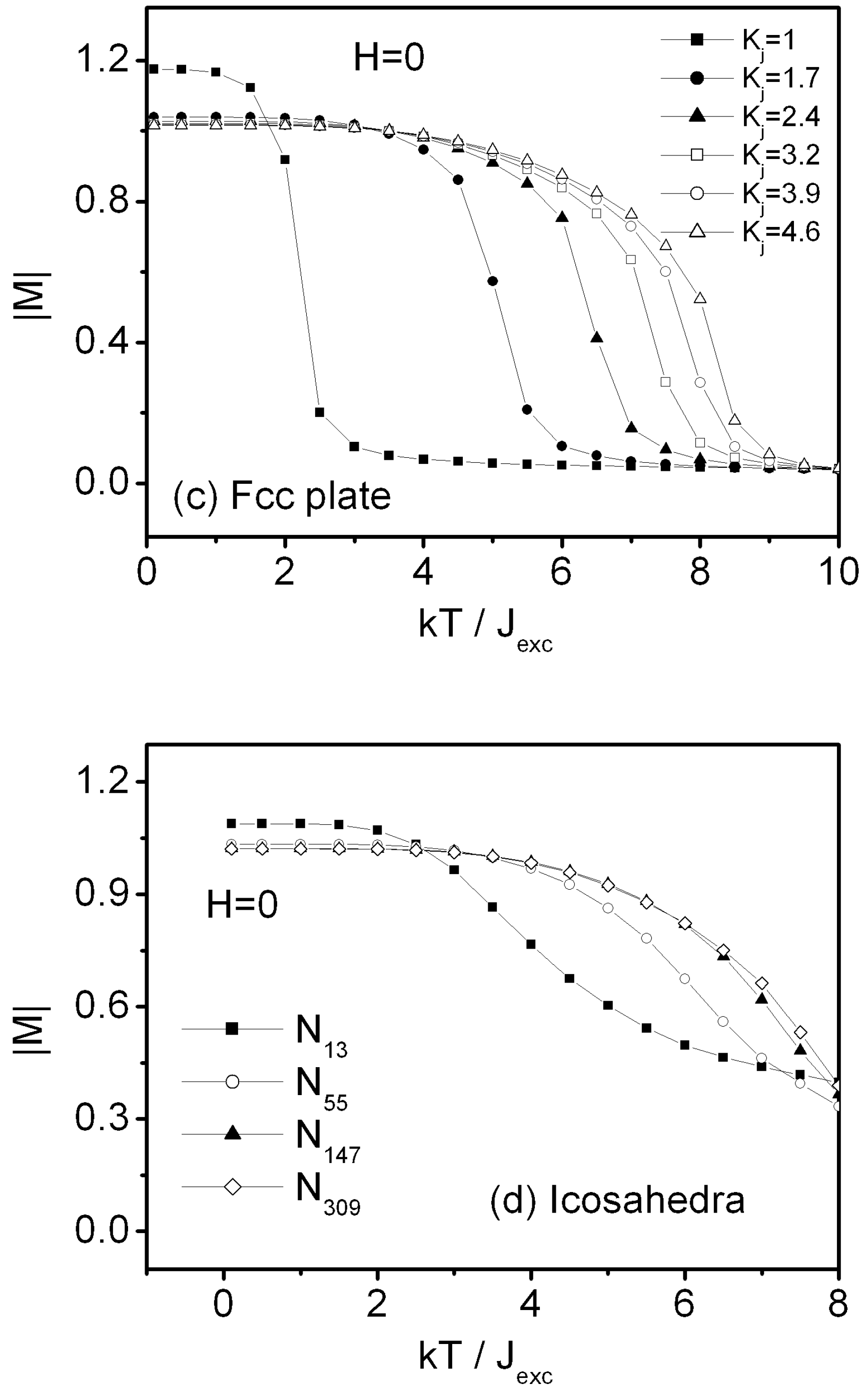

Figure 4.5 MC-simulated temperature and size dependence of the M_S for (a) fcc dot, (b) fcc rod, (c) fcc plate, and (d) Icosahedral spin systems.[175]

of a larger spin system. As a result, in the small spin system, the number of nonaligned spins (minority) decreases. Correspondingly, the magnetization is smaller than that of the larger system.

Differentiating Eq (4.8) against $E_{exc}(K_j)$ leads to the $M_S(K_j, T)$ in the mid-T region:

$$
\begin{aligned}
\frac{\Delta M_S(K_j,T)}{M_S(\infty,T)} &= \frac{E_{exc}(\infty)N_j {g_J}^2 {\mu_B}^2 A}{2k_B T M_S(\infty,T)}\left\{\csc h^2\left[\frac{g_J \mu_B}{k_B T} A E_{exc}(\infty)\right] - \right. \\
&\qquad \left. (2J+1)^2 \csc h^2\left[\frac{(2J+1)g_J \mu_B}{2k_B T} A E_{exc}(\infty)\right]\right\} \times \frac{\Delta E_{exc}(K_j)}{E_{exc}(\infty)} \\
&= \alpha(J,T)\sum\nolimits_{i\le 3}\gamma_i (z_{ib} {c_i}^{-m} - 1)
\end{aligned}
\tag{4.18}
$$

where parameter $\alpha(J, T)$ is temperature and material dependent. At mid-temperature, the size effect on the J becomes insignificant compared with the E_{exc}. Eq (4.18) indicates that the tailoring of M_S at a temperature close to T_C is dominated by the E_{exc}, which drops with solid size. The matching of predictions based on Eq (4.18) with $\alpha(J, T) = 1.4$ to the MC simulative results are shown in Figure 4.6 (b). The calculated trend is consistent with the measurement as well.

In the third region, at a temperature well above the T_C of the largest particle, or in the paramagnetic phase, the remnant magnetism is higher for smaller particles, which is attributed to the slower temperature decay in the Monte Carlo study and to the increasing fluctuations with a decrease in the cluster size.[31]

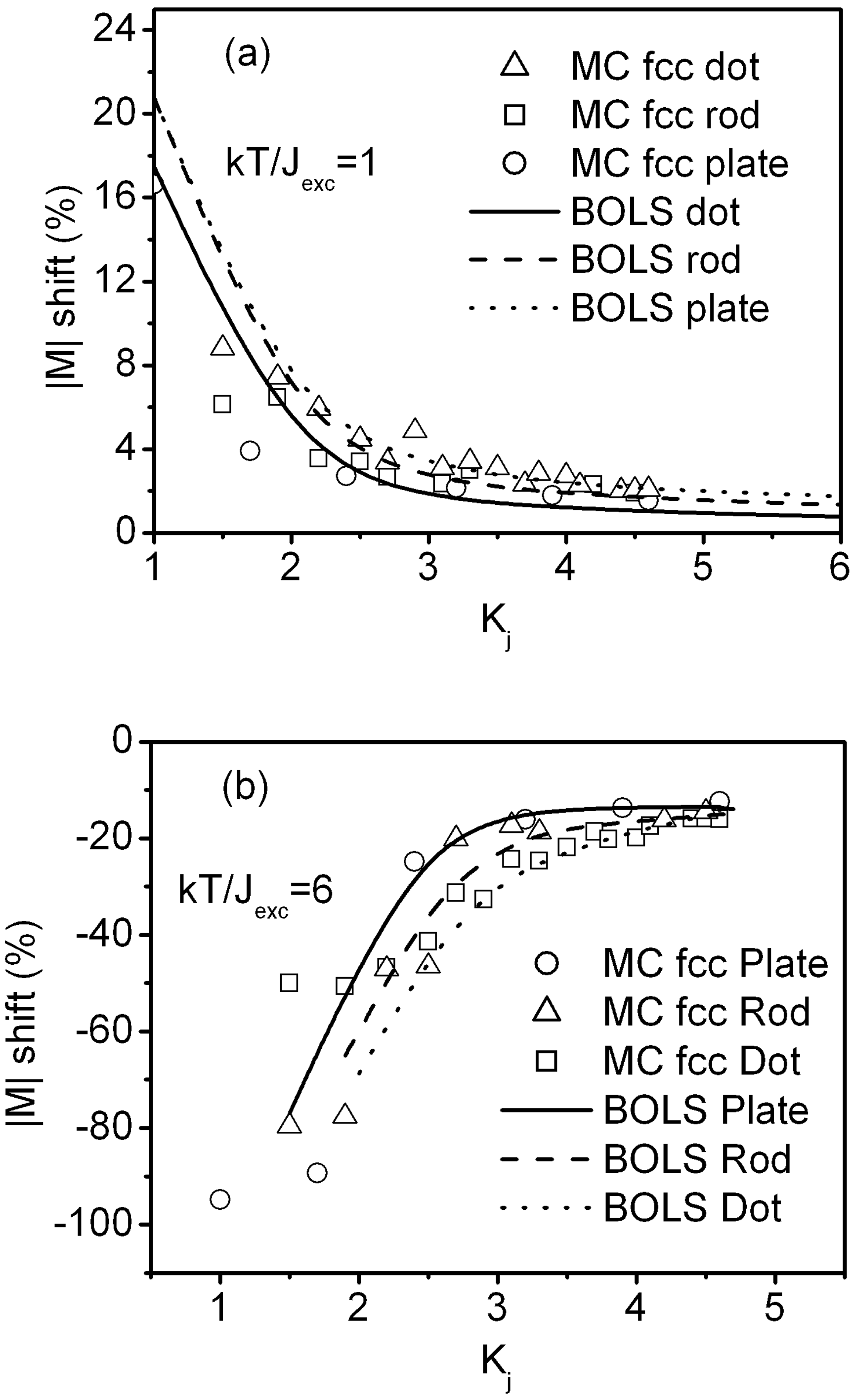

Figure 4.6 The two outstanding regions showing the size-dependent $M_S(K_j, T)$ derived by MC simulation: (a) k_BT/J_{exc} = 1 (*low-T*); (b) k_BT/J_{exc} = 6 (*mid-T*) $|M|$ shift = $[|M|(K_j)-|M|(\infty)]$ / $|M|(\infty) \times 100\%$.[175]

Compared with the $M_S(K_j, T\sim 0K)$ derived in Ref. [31] from the MC calculation, the current results show clear size dependence and the resonant features in region I, as experimentally observed by many researchers. The same trends of changes in regions II and III remain. In Ref. [31], the author assumed that even at very low temperature, the magnetization of a small particle is smaller than that of a large particle. The differences are due to the unawareness of the CN imperfection-enhanced atomic μ_{i} (or angular momentum $J(K_j)$) at that point of time. Without taking the enhanced surface μ_i into consideration, the magnetic moments for all the spins are equal, and the magnetization of the system is merely affected by the exchange energy and thermal vibrational energy. As a result, the enhancement of the magnetization at very low temperature for a nanosolid cannot be observed.

4.2.3 $M_S(K_j)$ oscillation and structural stability

Figure 4.7 (a) and (b) show the oscillation behavior of M_S at smaller sizes, which is common to various crystal structures. This suggests that the oscillation originates from the *S/V* ratio because some particles may have fewer surface atoms with a smaller γ_{ij} value than that of the adjacent larger or smaller particles. Figure 4.8 shows the *S/V* ratio of the first surface layer of fcc and body-centered cubic (bcc) spherical dots, which can be compared with the M_S behavior of the fcc spherical dot in Figure 4.7 (a). The behavior of the *S/V* ratio versus the atom number has the same tendency. Therefore, it is not surprising that the fraction of the lower-coordinated surface atoms causes such artifacts. The simulative oscillation behavior is consistent with that observed in Ni clusters by Apsel *et* *al*,[48] who found an oscillation behavior and the smallest magnetic moments for clusters N_{13}, N_{34}, and $N_{55\text{-}56}$ at low temperatures.

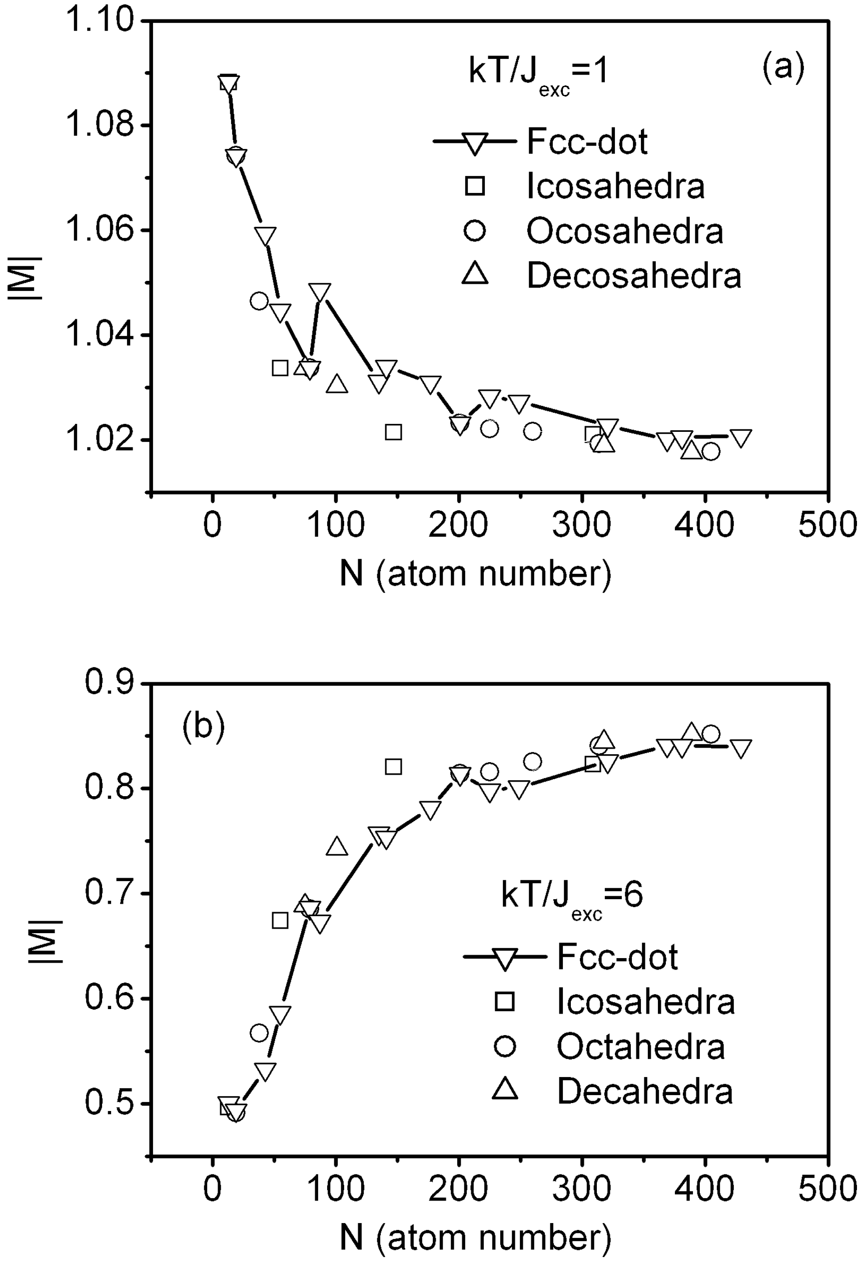

Figure 4.7 Comparison of the size dependence of the M_S of the fcc spherical particle, icosahedra, Marks decahedron (labeled as decahedron in the figure) and fcc truncated octahedron (labeled as octahedron in the figure) at temperature (a) k_BT/J_{exc} = 1 and (b) k_BT/J_{exc} = 6, showing the oscillation features and the structural stability. Lower M_S at low T indicates that fewer atoms are located at the surface, corresponding to a more stable structure.[175]

The physical properties of nanosolids in a molecular regime typically exhibit a very irregular dependence on their aggregate size, with certain sizes standing out in particular, namely “magic numbers.” In a mesoscale regime, on the other hand, they behave in a regular way. As can be seen, compared to other structures, the icosahedron, the Marks decahedron, and the fcc truncated octahedron have lower M_S in the low-T region and higher M_S in the mid-T region, especially the small icosahedral particles N_{55} and N_{147}. The mass spectra of nanosolids usually exhibit especially abundant sizes that often reflect particularly stable structures, especially reactive nanosolids, or closed electronic shells.[186] These “magic number” sizes are of great theoretical interest since many of them correspond to compact structures that are especially stable. The magnetic moment of ferromagnetic nanosolids has been reported to exhibit the same behavior.[25,67] The simulative results in this study show the same cases that N_{13}, N_{55}, and N_{147} are the magnetic number for small magnetic nanoparticles,

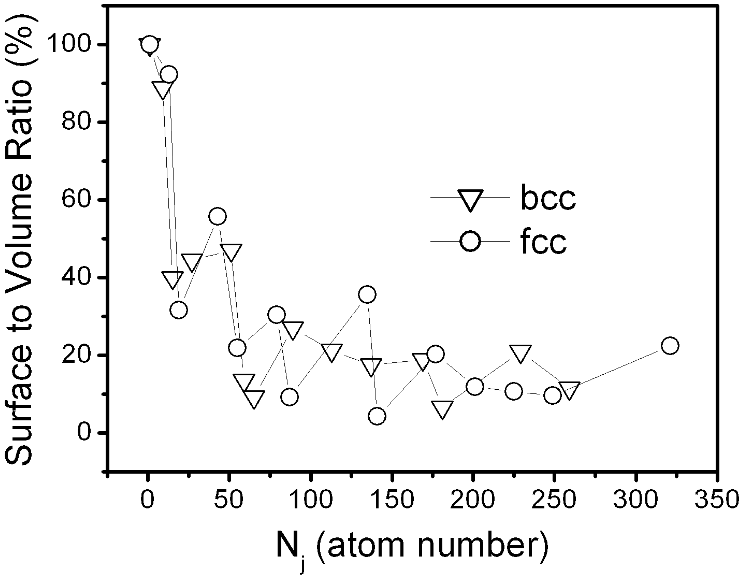

Figure 4.8 Shows the quantized S/V ratio γ of the first surface layer of fcc and bcc structures.[175]

confirming that the icosahedron is the most closed structure for small size.

However, when the atom number, N_j, is larger than 300, the fcc truncated octahedron exhibits the smallest M_S in the low-T region and the highest M_S in the mid-T region, indicating that it is the most compact structure when $N_j > 300$. The MC simulation results here are consistent with a recent experimental study on copper particles, in which Reinhard *et al*[187] showed that the icosahedral structure dominates at sizes well below a diameter of 3.8 nm, while the fcc structure is preferred at this size or above. This arises from the energy competition between reducing the surface energy and increasing the strain energy. It often happens that icosahedra are the most stable at small sizes due to their low surface energy and good quasispherical structures, decahedra are favorable at intermediate sizes, and crystalline structures are preferred in the limit of large objects.

4.2.4 T$_C$ suppression

The drop of exchange energy also determines the critical temperature of the melting and phase transition:

$$\frac{\Delta E_{exc}(K)}{E_{exc}(\infty)} = \frac{\Delta T_C(K)}{T_C(\infty)} = \frac{\Delta T_m(K)}{T_m(\infty)} = \sum_{i\leq 3} \gamma_i (z_{ib} c_i^{-m} - 1) \qquad (4.19)$$

The MC simulation also shows the T_C suppression, which is consistent with the BOLS predictions that have been discussed in detail in section 4.1.2. The BOLS predictive and simulative results are shown in Figure 4.9. When $K = 3.9$, T_C suppression of the films is about -40%. The bulk value of $kT_C/J_0 \approx 13$ is used during the normalization.

4.3 Experimental verification

- Magnetization

To investigate the size effect on the magnetization of the thin film, Ni films were deposited by the FCVA technique (100 ~ 124 nm). The grain size ranged from 3 to 10 nm. Figure 4.10 shows the typical 3D AFM morphology of the Ni film with roughness (RMS) of 0.8 nm. XRD profiles in Figure 4.11 show three strong peaks corresponding to the Ni(111), Ni(200), and Ni(220) faces. The two resolved small peaks belong to the silicon. The XRD profile for the bare silicon substrate was compared; the shift of Si peaks was due to the different rotation angle of silicon substrates in the plane of the sample holder. The stronger and sharper nickel peaks indicated a larger grain size according to Scherrer's equation. The grain sizes derived from the Scherrer equation were about 3.1, 3.2, 5.5, 7.9, and 10.0 nm.

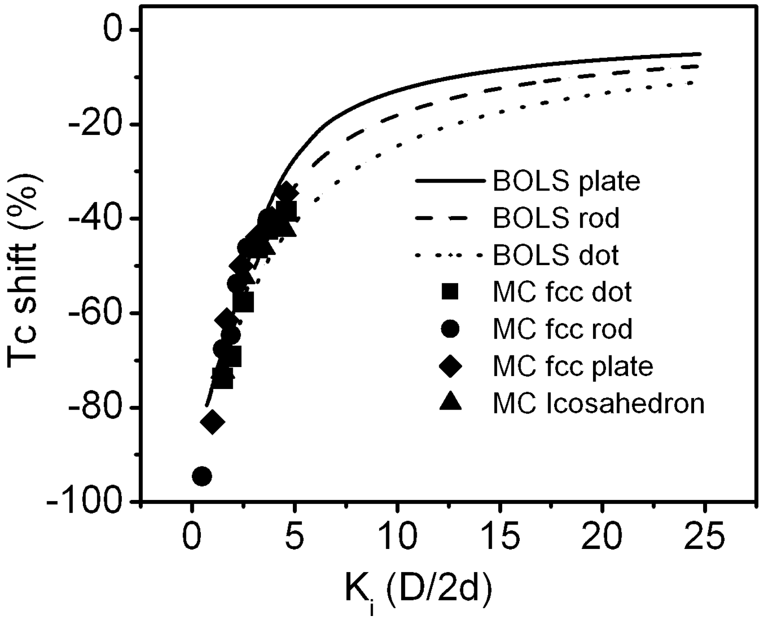

Figure 4.9 The size dependence of T_C shift by MC simulation together with the BOLS prediction.

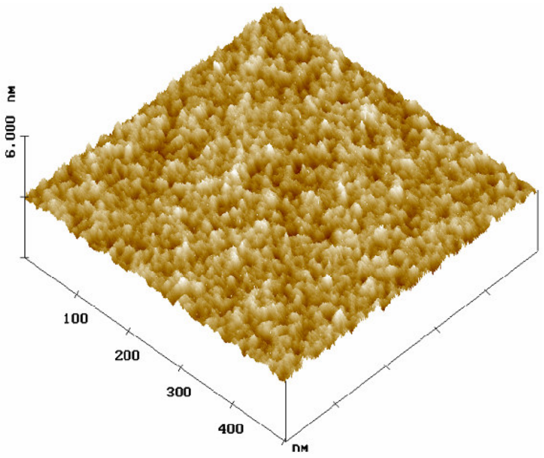

Figure 4.10 The typical surface morphology of Ni thin film deposited on silicon substrate using FCVA. The surface is smooth with a roughness (RMS) of about 0.8 nm.

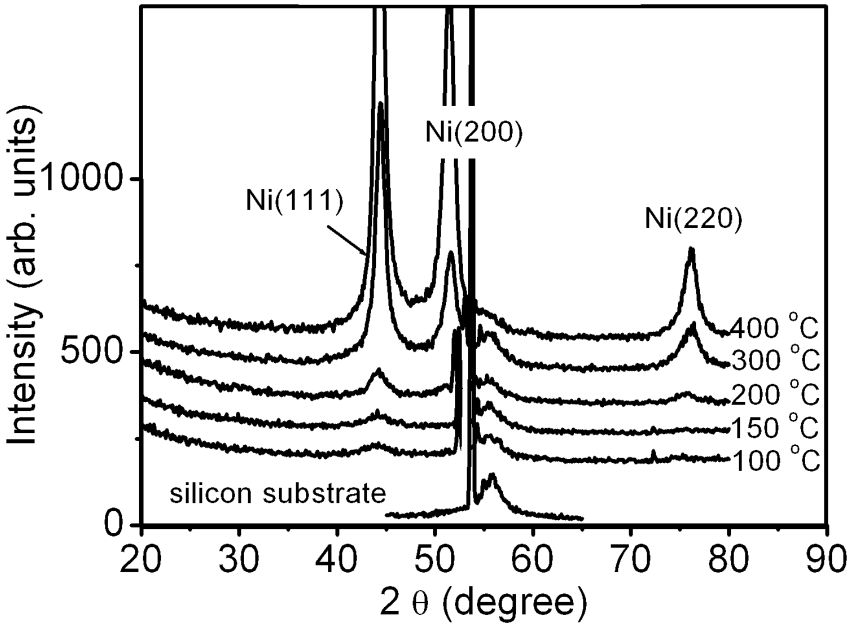

Figure 4.11 X-ray diffraction pattern of the Ni film at various substrate temperatures. The peak intensity decreases and the peaks become broader with the decrease of the substrate temperature, indicating a decrease in crystalline size.

Figure 4.12 shows the magnetization-hysteresis (M-H) loops of Ni films measured at room temperature, note that H=0 should be in the center of the loops, the shift of the loop is due to the reading shift of VSM. With the reduction in the grain size, the squareness and saturation magnetization decrease while the coercivity (H_C) increases. The size dependence of the M_S tailoring at room temperature is shown in Figure 4.13. The M_S drops with particle size, $K_j = D / 2d$, where $d = 0.2488$ nm is the diameter of the Ni atom and D is the diameter of the grain size. The M_S tailoring of films with $K_j \approx 6$ is about -83% compared with the bulk value (6.068 kG). Even for the film with $K_j = 20$, the M_S decreases by 31% compared with the bulk value. Theoretical fitting with $\alpha(J, T) = 4.0$ from Eq (4.18) is also shown in Figure 4.13. The tendency of the size dependence of M_S is consistent with most of the experimental observations[67-72] and agrees with the Monte Carlo simulations in region II. The dash line is the M_S prediction at a lower temperature with $\alpha(J, T) = 1.6$, which shows a higher M_S with the same size. It is interesting that when the particle size is reduced to $K_j = 5$ ($D = 2.5$ nm), $M_S = 0$. This means the Curie temperature decreases to near room temperature when K_j reaches 5. For an Ni particle of $K_j = 5$, the T_C drops by ~51% from 631 K to 309 K.[188] While at low temperature with $\alpha(J, T) = 1.6$, the M_S still remain around half of the bulk value.

One may wonder about the effect of impurities such as surface oxidation on the measurement. Although XRD and XPS revealed no impurities in the samples, we cannot exclude the existence of trace impurities. However, all the samples were prepared and measured under the same conditions and we used the relative change of the quantities, which should minimize the influence of such artifacts caused by impurities whether they exist or not, and the measured data should be purely size dependent.

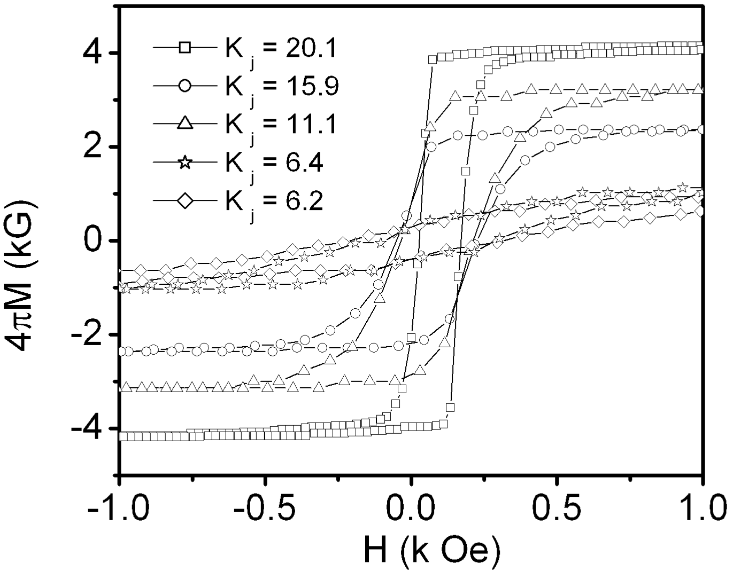

Figure 4.12 Size dependence of the M-H loops of Ni films.[188]

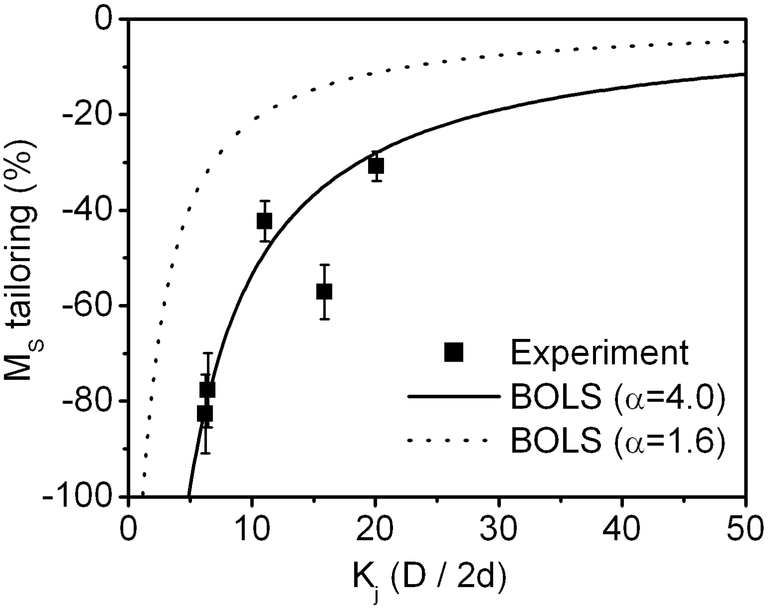

Figure 4.13 Crystalline size dependence of M_S under the maximum applied of 10 k Oe at ambient. The tendency agrees with most of the experiment observations and the Monte Carlo calculations in region II. The solid line and dot line are the theoretical prediction based on Eq. (4.18) with $\alpha(T)$ = 4.0 and lower temperature $\alpha(T)$ = 1.6 respectively.[188]

- Coercivity

Generally, in ferro- or ferrimagnets, magnetic particles consist of magnetic domains if the particle diameter exceeds several hundred nanometers.[189] In contrast, when the particle size decreases to tens of nanometer, the particles become a single magnetic domain. In that case, the magnetization process also changes from the domain-wall motion to a whole-spin rotation in the magnetic particle. Because the whole-spin rotation requires more energy than the domain-wall motion, it is hard to magnetize a single magnetic domain particle.[190]

It is known that both the interspin interaction within a domain (E_{exc}) and the intergrain interaction within a solid (E_{EXC}) composed of nanograins can be described using the Ising model. Considering a grain as a giant spinner, with a magnetic moment *S*, the exchange energy of the spinner interacting with its z_i nearest neighbors follows the Ising model, as shown in Eq (4.5). For intergrain interaction, the d_i is replaced with grain diameter, *D*, if a uniform grain size is assumed. The z_i is the number of neighboring grains of a specific grain. S_i and S_j are giant spins for a grain. For an isolated grain below a certain size (of the order of 15 nm, i.e. about 10^5 atoms per Fe cluster[191]), for an isolated grain below a certain size, the coercivity is zero (superparamagnetic), considering a grain as a giant spin, when may grains get closer, the intergrains' exchange energy increases, which dominates the anisotropy energy:[94]

$$H_C \propto \frac{1}{2} H_S \propto E_{EXC,i} \propto ZD^{-1} \tag{4.20}$$

where H_S is the field to uniformly rotate the moments into alignment that is proportional to the intergrain interaction. Z is the mean effective number of neighboring grains of the specific grain.

Figure 4.14 shows the measured grain size dependence of the coercivity together with the theoretical prediction. The prediction in Eq (4.20) fits well with the measured H_C with m = 1. The bulk value is 0.7 Oe. The size-enhanced H_C is consistent with other observations of soft magnetic materials such as Fe-Ni films[192] and Co-Fe-Ni films.[193]

- Other properties

Squareness: The M-H loop provides information about the squareness. The squareness factor is defined by the ratio of the reverse field required to reduce

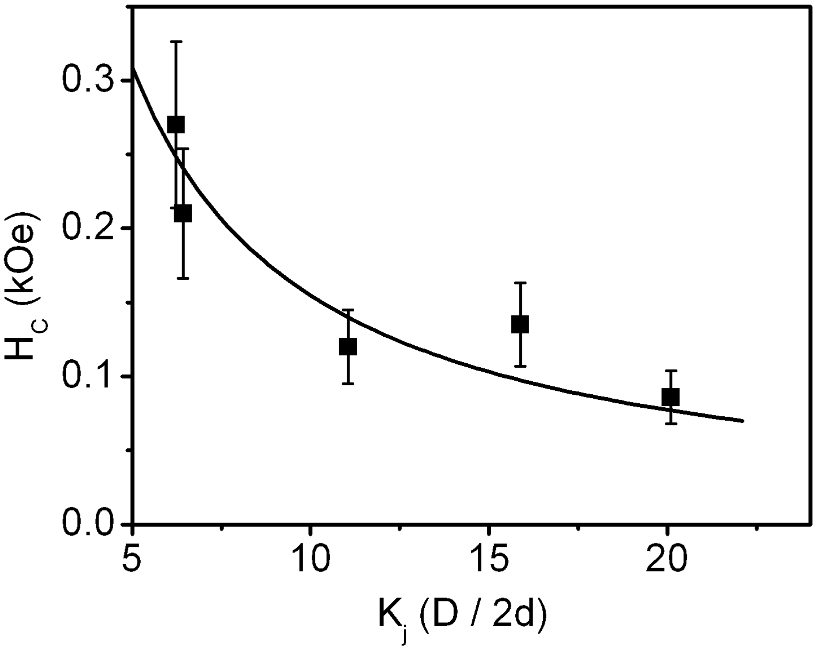

Figure 4.14 Size-enhanced H_C characterized at room temperature.

magnetization by 10% from the remanence to H_C. A squareness factor of 1 corresponds to a perfectly square loop. Another parameter that represents the squareness is the remanence ratio, R_r, which is defined as $R_r = M_r / M_S$. The loop shifts due to the zero position shifts of VSM. To find the Mr, it is needed to re-center the loops along the x-axis to get an equal Hc on both side of y-axis. Figure 4.15 shows the squareness factor and the remanence ratio as a function of size. The squareness factor decreases with grain size.

Permeability: The permeability (χ_m) was found to decrease with the decrease in size, which is consistent with the grain boundary model (NMGB)[101] as introduced in section 2.1.3. The grain size effects on the magnetic properties of Ni films are summarized in Table 4.1.

Anisotropy: The ferromagnetic thin films normally show two distinguishing magnetizations along and perpendicular to the film's surface.

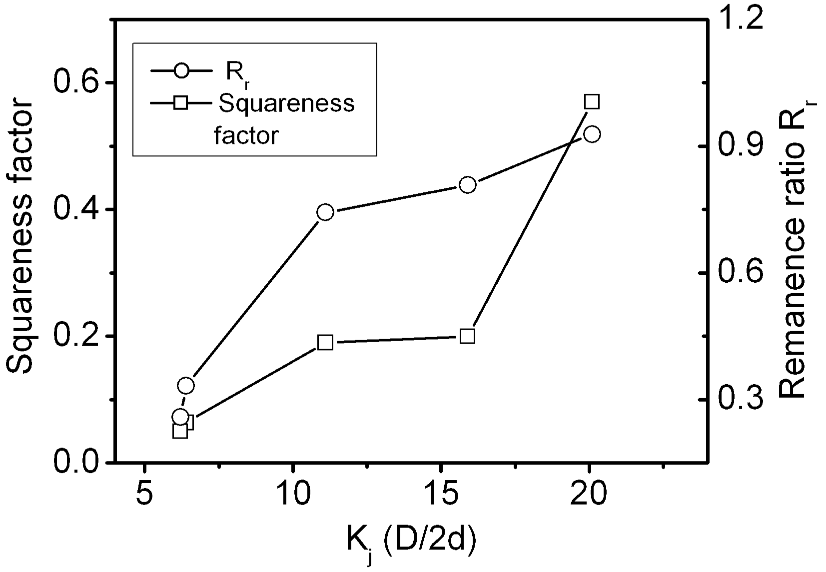

Figure 4.15 The squareness factor and remanence ratio as a function of size.

Table 4.1 Size effect on the in plane magnetic properties of Ni films.

Grain size (nm)	$4\pi M_S$ (kG)	$4\pi M_r$ (kG)	H_{Cm} (kOe)	Squareness	R_r	χ_m	μ/μ_B
Bulk	6.08	/	0.0007	/	/	/	0.6
10.0	4.2	3.9	0.078	0.57	0.93	25.88	0.41
7.9	2.6	2.1	0.135	0.20	0.81	5.59	0.26
5.5	3.5	2.6	0.12	0.19	0.74	7.70	0.34
3.2	1.05	0.35	0.27	0.064	0.33	1.16	0.10
3.1	1.35	0.35	0.21	0.050	0.26	0.69	0.13

Figure 4.16 compares the M-H loops for a field applied parallel (//) and perpendicular (⊥) to the film's surface. It can be seen that the easy magnetization direction is parallel to the film's surface. When the field is applied perpendicular to the film's surface, the remanence and squareness are much lower and the coercivity is much higher.

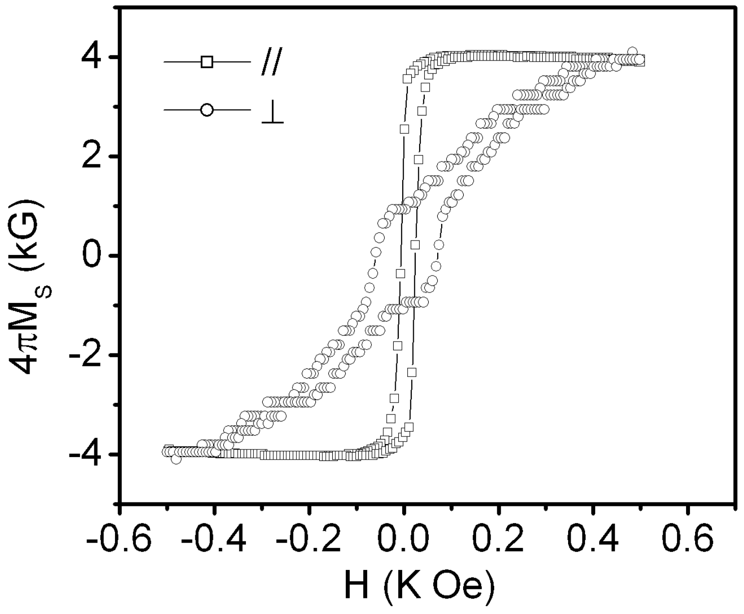

Figure 4.16 M-H loops of Ni films 148 nm thick under field applied to the direction parallel (//) and perpendicular (⊥) of the surface plane.

CHAPTER 5 RESULTS AND DISCUSSION II: NITROGEN-CATALYTIC EFFECT

5.1 BBB perdition

In the previous section, we discussed that miniaturization of a ferromagnetic solid can modify the magnetization by reducing the exchange energy and increasing the surface spin magnetic moment in the Ising model. This section shows that the chemical reaction of iron with nitrogen also modifies the magnetization by changing the angular momentum of the ferromagnetic atoms.

5.1.1 Ms

Figure 5.1 illustrates the BBB bond model for a nitride (NB_3).[194] A nitrogen atom hybridizes and interacts with an arbitrary element, B, through four directional orbitals to form a quasitetrahedron. Atoms labeled 1 are B^+; atoms labeled 2 are lone-pair induced B dipoles with an expansion in size and elevations of energy states. When a reaction takes place, all atoms change their sizes and valence states. The N-B bonds are mainly ionic or polar-covalent due to the difference in electronegativity (χ) between N and B, ($\chi_N = 3.0$, $\chi_B < 2.5$, for metal and semiconductor $\chi_B = 1.5$-1.9).[195] Formation of the nonbonding lone pair is the intrinsic feature of N and it is independent of element B being considered. However, the number of lone pairs determines the C_3 group symmetry of NB_3, and consequently, some physical properties. The symmetry may change depending on the bonding circumstance.[196,197,198]

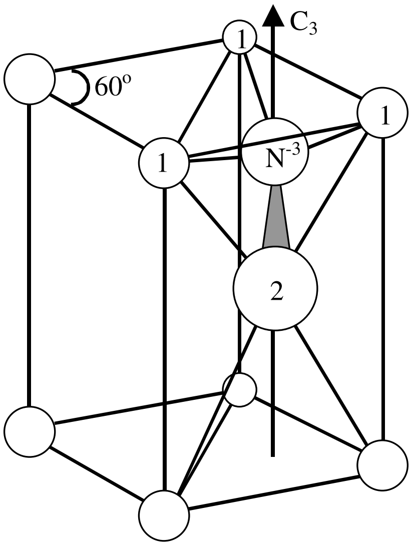

Figure 5.1 The BBB model for nitridation. N hybridizes and interacts with arbitrary element B through the bonding and nonbonding lone pair to form the quasitetrahedron: NB_3 [N^{-3} + $3B^{+1}$ (labeled 1) + B (dipole, labeled 2)]. The number and orientation of the lone pair give different geometrical symmetry as indicated.[194]

When a small amount of nitrogen is added into the Fe lattice, the energy band of Fe is modified.[194] Alternation of the Fe valences changes the magnetic moments of the Fe atoms in different ways according to Hund's law, as shown in Figure 5.2 for the possible atomic valence states. The reaction alters the atomic states of iron from Fe ($3d^64s^2$, $J = 2.22$) to Fe^+ ($3d^54s^2$, $J = 2.50$) or Fe dipole ($3d^54s^24p^1$, $J = 4.0$, or even $3d^52s^24d^1$, $J = 5.0$). In the former, Fe donates one 3d electron to the sp^3-hybrid orbital of N, while in the latter, one 3d electron jumps into the Fe's outer empty shells, 4p or 4d, with higher energy. For a (N^{-3} + $3Fe^{+1}$ + Fe (dipole)) cluster, the average J enhances from 2.22 (measurement) to 2.875 or even 3.125.[194] The possible atomic valence states and the corresponding angular momentum of an iron atom and its ions are shown in Table 5.1.

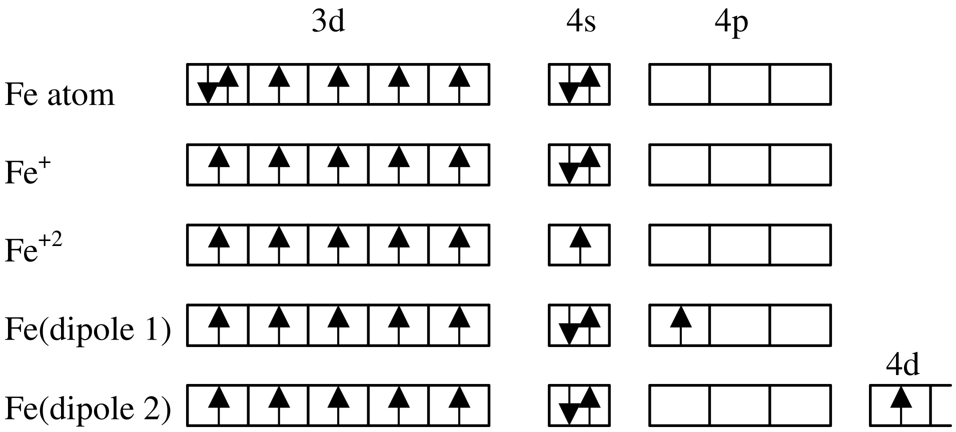

Figure 5.2 Possible distribution of 3*d* and 4*s* electrons of Fe, Fe^{+}, Fe^{+2}, and the dipoles.

Table 5.1 Variations of angular momentum of Fe with its atomic states.[152]

VALENCE STATE	CONFIGURATION	$S = \Sigma S_J$	$L = \Sigma L_J$	J= (L±S)
Fe	$3d^6 4s^2$	2(=4×1/2)	0(3d-frozen)	2(2.22)
Fe^{+}	$3d^5 4s^2$	2.5	0	2.5
Fe^{+2}	$3d^5 4s^1$	2.5+0.5	0	3.0
Fe(dipole 1)	$3d^5 4s^2 4p^1$	2.5+0.5	0+1	4.0
Fe(dipole 2)	$3d^5 4s^2 4d^1$	2.5+0.5	0+2	5.0

As an approximation, considering an Fe system of y atoms, with x nitrogen atoms introduced into the Fe lattice, the percentage of nitrogen is $a_N = x / (x + y) \times 100\%$. Suppose every nitrogen atom changes the valence states of its four neighboring Fe atoms from 4Fe to $N^{-3} + 3Fe^{+1}$ + Fe (dipole), the average magnetic moment of its four neighboring iron atoms then changes from 2.22 to 3.125. For an iron nitride system with N : Fe < 1 : 4, the average magnetic moment of the whole system can be approximately estimated as:

$$\bar{\mu} = \mu / y = \frac{4x \times 3.125\mu_B}{y} + \frac{(y-4x)\times 2.2\mu_B}{y} = 2.2\mu_B + \frac{3.7x}{y}\mu_B \qquad (5.1)$$

The relative change can then be expressed as:

$$\frac{\bar{\mu}-\bar{\mu}_{Fe}}{\bar{\mu}_{Fe}}=\frac{3.7}{2.2}\times\frac{x}{y}=1.682\times\frac{a_N}{1-a_N} \qquad (5.2)$$

which shows that the magnetic moment of the iron system increases with the percentage of nitrogen. However, Eq. (5.2) only applies when the nitrogen content is low (N : Fe < 1 : 4). With an increase in the nitrogen in the films, the degree of polarization for Fe^{dipole} will decrease. The dipole electron may even be captured by the excess nitrogen atom and form a valence state, Fe^+, with a lower magnetic moment than that of the Fe^{dipole}. As a result, the $4\pi M_S$ will decrease. The experimental result shows that when the $a_N > 0.107$ (N: Fe ≈ 3 : 25), the $4\pi M_S$ begins to decrease, indicating that the formation of a hydrogen bond like that will decrease the momentum of the Fe specimen. The tendency of the BBB predictions is consistent with the electronic structure calculations.[199] Most of the calculations use the local spin density approximation, many use the atomic spheres approximation, and some use the first-principles calculations. The calculated Fe electron structure indicates that the nearest neighbors of the nitrogen atom have a reduced spin splitting, while the more distant iron shows a deeper spin splitting (Fe dipoles), which increases the magnetic moment compared with the pure iron.[199]

5.1.2 Resistivity

The alteration of the atomic states of iron from Fe to Fe^+ or Fe dipole also change the resistivity of the material. As indicated in Figure 5.1, nitrogen interacts with atoms of iron and hybridizes its *sp* orbitals to form four directional orbitals. Nitrogen captures three electrons from iron atoms, and the 2s and 2p levels of nitrogen are fully occupied with eight electrons that will repopulate in the four directional orbitals. Therefore, three of the four hybridized orbitals are occupied by shared electron pairs (bonding orbitals). The remaining orbital is occupied by the lone electron pair of nitrogen (nonbonding orbitals).

The formation of bonds, nonbonding lone pair, and antibonding dipoles, as well as the H-like bonds, generates corresponding features that add to the DOS of the valence band and above of the host. The electrons are then more localized and hence the carrier mobility is lower. The additional DOS features of bonding << Fermi energy (E_F), holes $\leq E_F$, and antibonding dipoles $\leq E_F$. With the full occupancy of the p-orbital of nitrogen, the *sp* orbitals of the nitrogen hybridize. As a result, electronic vacancies are produced right below E_F, generating a gap between the conduction band and the valence band of Fe. Consequently, with the nitrogen catalysis, the resistivity increases.

5.2 Deposition of Fe-N films

The deposition conditions are summarized in Table 3.3. Three approaches have been used to introduce nitrogen into the films, as described in section 3.3.3. In approach I, it was found that even when the nitrogen partial pressure was increased up to 2.0×10^{-4} torr, it was hard to detect nitrogen in the films. Therefore, this approach is less effective. In approach II, nitrogen was incorporated into the films. The nitrogen concentration in the film can be controlled by changing the nitrogen partial pressure, P_N. This approach limits the nitrogen concentration in the film. In order to further increase the nitrogen concentration, approach III was implemented.

5.2.1 Deposition rate

Both the approaches and the gas pressure significantly affect the deposition rate, *R*. Figure 5.3 (a) shows the dependence of the deposition rate on the P_N in approach II. The deposition rate decreases from 39 nm/min to 15 nm/min when the P_N increases from 7×10^{-5} torr to 2.0×10^{-4} torr. Increasing P_N results in an increase in the frequency of collision between the ions and the nitrogen molecules; correspondingly, the mean free path, the energy of ion, and the plasma density decrease. As a result, the deposition rate decreases.

Figure 5.3 (b) shows the deposition rate that is affected by the P_N:P_Ar ratio in approach III. The deposition rate is affected significantly by the P_N:P_Ar ratio. The highest deposition rate in approach III is 6.4 nm/min, which is much smaller than that in approach II. When the P_N:P_Ar = 10:7, the deposition rate decreases to 0.35 nm/min, which indicates that the resputtering effect of Ar^+ becomes significant when the Ar ratio is high.

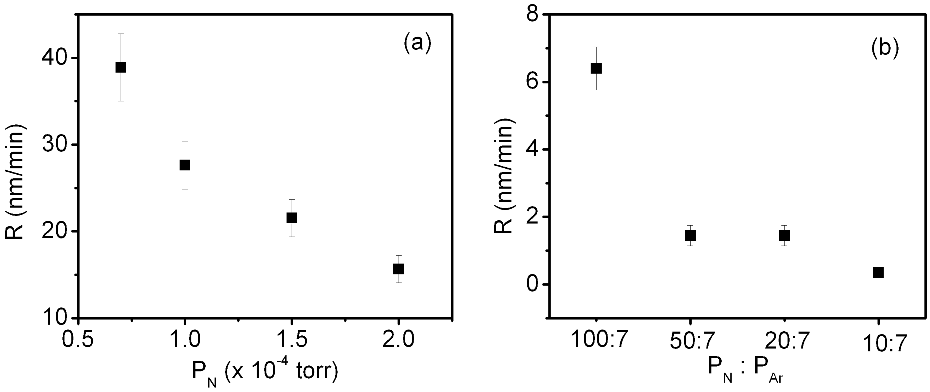

Figure 5.3 The deposition rate R varies (a) with P_N in approach II and (b) P_N:P_Ar in approach III.

5.2.2 Surface morphology

The surface morphology differs greatly between the films deposited using different approaches. Figure 5.4 (a) and (b) shows that the films deposited using approach II possess a smooth surface morphology. The RMS (<0.3 nm) of the films deposited using approach II is much lower than that of the films deposited using approach III (~1.5 nm), as shown in Figure 5.4 (c) and (d). This is because the bombardment of the energetic ion beams in approach III is more severe than that in approach II due to the introduction of an ion beam source.

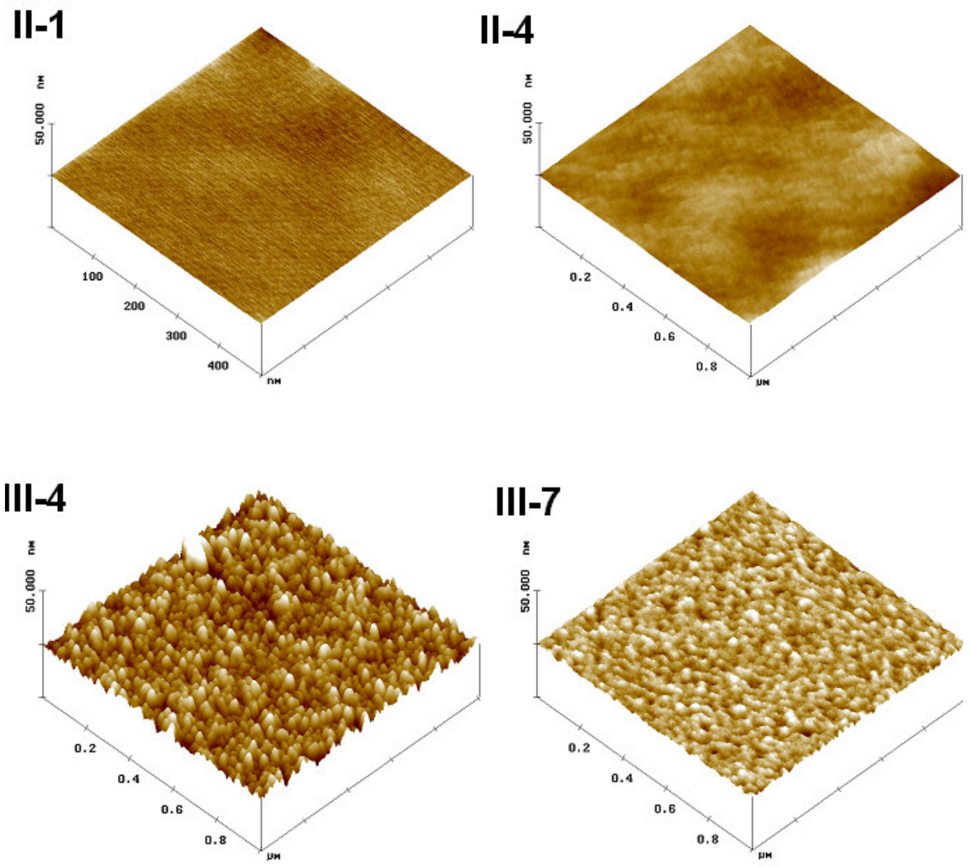

Figure 5.4 Typical AFM surface morphology of the Fe-N films deposited using approaches II and III. With an RMS value of about 0.3 nm, the films using approach II are far smoother than those with an RMS about 1.6 nm deposited using approach III. The films thickness is 75 ± 5 nm.

5.2.3 Microstructure

The XRD patterns of sample II-1 and II-4 are shown in Figure 5.5 (a). Sample II-1 consists of $\alpha + \alpha' + \alpha'' + \gamma'$ multiphases, while sample II-4 possesses nitrogen-poor phases ($\alpha + \alpha'$) due to the lower P_N. This is because the higher pressure of N_2 results in higher nitrogen ionization in the plasma area, which introduces a higher nitrogen ion dose in the plasma. Accordingly, the nitrogen concentration in the films is higher. Figure 5.5 (b) shows the XRD pattern of sample III-1 that was deposited with P_{N}:P_{Ar} = 100:7 using approach III. The pattern exhibits a clear γ''-FeN phase. When P_{N}:P_{Ar} is reduced to 80:7, multiphases including γ, ζ, and ε are exhibited in the Fe-N films, as shown in Figure 5.5 (c). With a further decrease in the P_{N}:P_{Ar}, all the samples exhibit a single ζ-Fe_2N phase, as shown in Figure 5.5 (d) and (e). Decreasing the P_{N}:P_{Ar} ratio in the ion beam source increases the bombarding and etching effect of Ar^+. As a result, a smaller grain size, poor crystallinity, and lower nitrogen concentration were obtained. When the P_{N}:P_{Ar} decreases to 20:7 and 10:7, as shown in Figure 5.5 (f), only weak α and α' peaks are observed.

5.2.4 Binding energy

Figure 5.6 shows the XPS profiles for the samples of pure Fe, II-1, III-1, III-3, and III-6. The Fe 2p XPS peak is around 707.0 eV,[37, 200] while the peaks at about 711 eV or higher in XPS Fe $2p^{3/2}$ spectra for samples III-1, III-3, and III-6 are related to Fe^{2+} and Fe^{3+} contribution.[201,202,203] The peaks of Fe $2p^{3/2}$ are significantly strong in sample III-1, which indicates that the proportion of Fe^{2+}/Fe^{3+} to Fe is larger; in other words, the nitrogen concentration is higher in the sample. This can be confirmed in the N1s spectra as well.

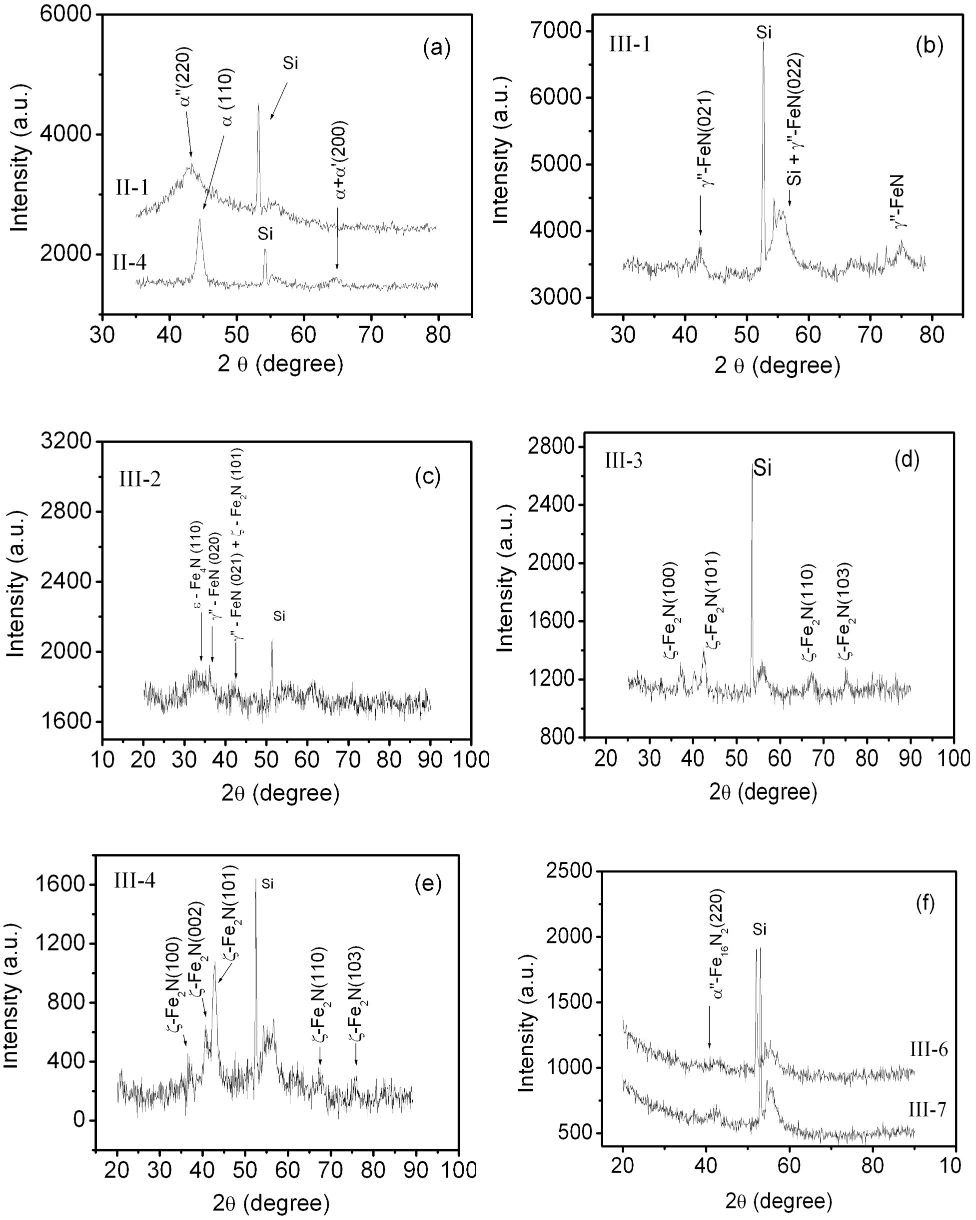

Figure 5.5 XRD profiles of the Fe-N films. (a) II-1 ($P_N = 2.0 \times 10^{-4}$ torr) & II-4 ($P_N = 0.7 \times 10^{-4}$ torr) show nitrogen-poor phases. (b) III-1 (P_N:P_{Ar} = 100:7) exhibits γ″-FeN phase. (c) II-2 (P_N:P_{Ar} = 80:7) presents ε and γ″ phases. (d) III-3 (P_N:P_{Ar} = 40:7) and (e) III-4 (P_N:P_{Ar} = 50:7) show ζ-Fe_2N phase. Only weak α and α′ peaks can be observed in (f) III-6 and III-7 (P_N:P_{Ar} = 20:7 and 10:7 respectively). (films thickness: 75 ± 5 nm)

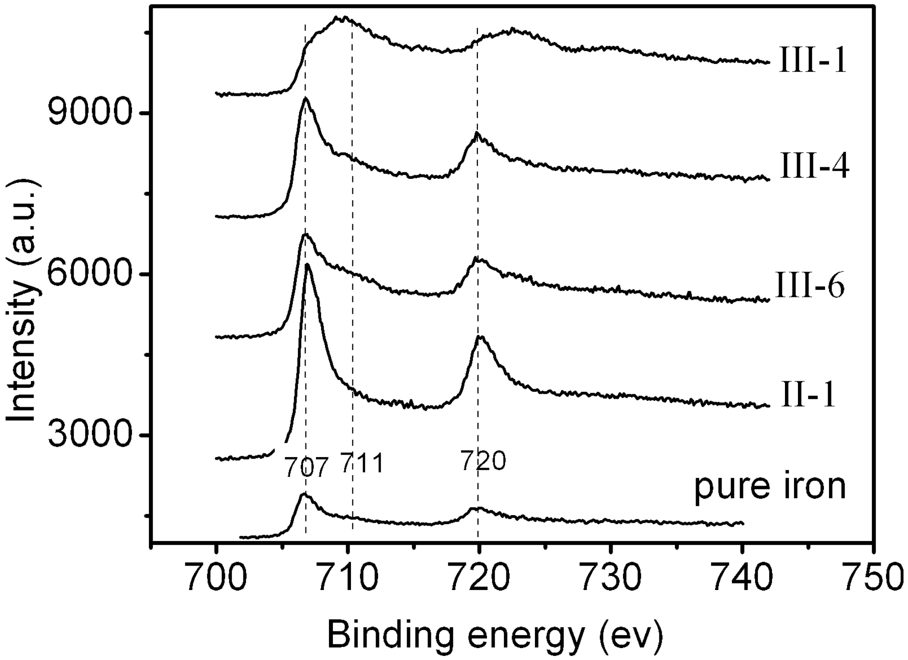

Figure 5.6 XPS binding energy of Fe, III-1, III-4, III-6, and II-1. The intensity of peak 707 decreases while peak 711 increases, which indicates the number increase of Fe^{2+} and Fe^{3+}.

The XPS N1s spectra for samples II-1, III-1, III-3, and III-6 in Figure 5.7 show a pronounced peak at 397 eV that corresponds to the typical Fe-N bond.[201-203] A small shift can be resolved in III-1, indicating a stronger Fe-N bonding state in sample II-1 than in sample III-1. The intensities of the N1s peaks of samples III-1, III-3, and III-6 are larger than those of sample II-1, which indicates that the nitrogen concentration in these samples is higher than that in sample II-1. This is because with the assistance of the ion beam source, nitrogen is easier to be incorporated into the films. The nitrogen concentrations that were calculated based on the N1s peaks are shown in Table 5.2.

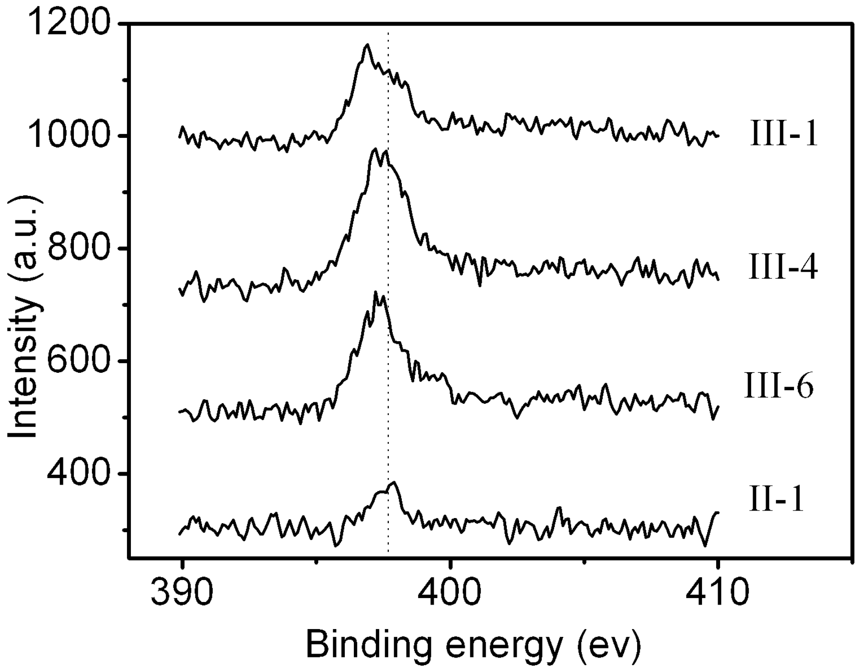

Figure 5.7 XPS binding energy of N1s in samples III-1, III-4, III-6, and II-1. The increase of the intensity indicates the increase of nitrogen concentration.

5.3 Nitrogen catalytic effect

5.3.1 M_S

Figure 5.8 (a) shows the in-plane M-H loops of the films deposited using approach II (samples II-1 to II-4) in comparison with the nitrogen-free iron film. The $4\pi M_S$ value of the pure Fe films is about 8.8 kG, which is much lower than the bulk value, 21.5 kG. This originated from the suppression effect of size reduction as discussed in section 4.1. Figure 5.8 (b) shows the in-plane M-H loops of the films deposited using approach III. The magnetization and squareness are smaller than those of the films deposited with method II. Figure 5.9 shows the $4\pi M_S$ versus the nitrogen concentration. With the increase in the nitrogen concentration, the $4\pi M_S$

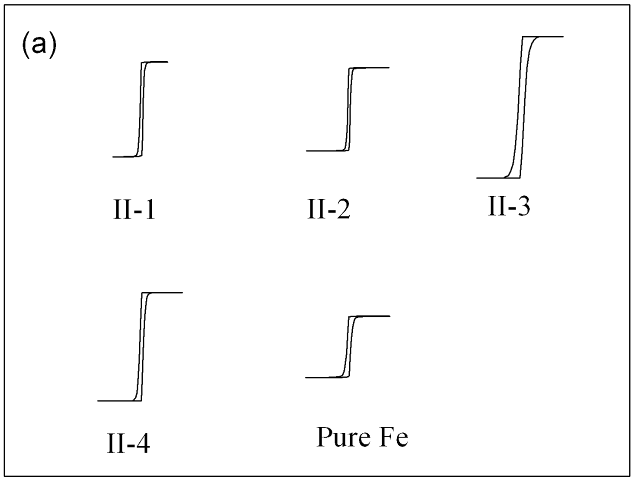

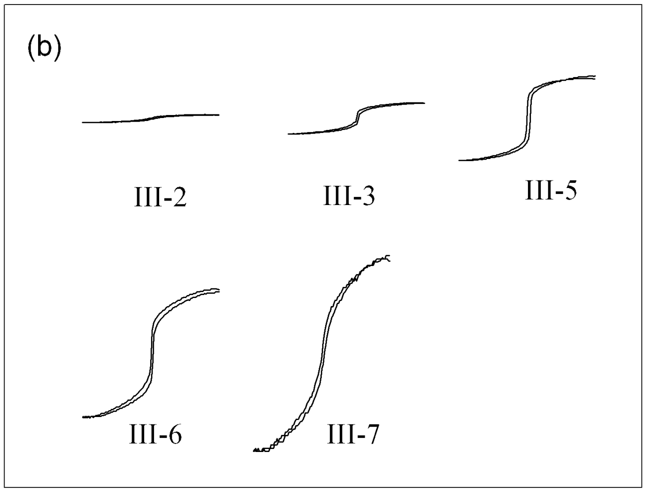

Figure 5.8 M-H loops of samples deposited with the gas introduction method of (a) I and II, and (b) III. (films thickness: 75 ± 5 nm)

firstly increases and then decreases. The highest M_S is exhibited in the II-3 sample with a nitrogen concentration of $a_N \approx 10\%$ and with multiphases of α and α', which is even higher than that of the bulk Fe. When $a_N = 10\%$, the corresponding enhancement of $4\pi M_S$ calculated by Eq (5.2) is 20%. This value is higher than that observed here (14.0%), which is due to the physical size-induced suppression of $4\pi M_S$ at ambient, as discussed in section 4.1.1.

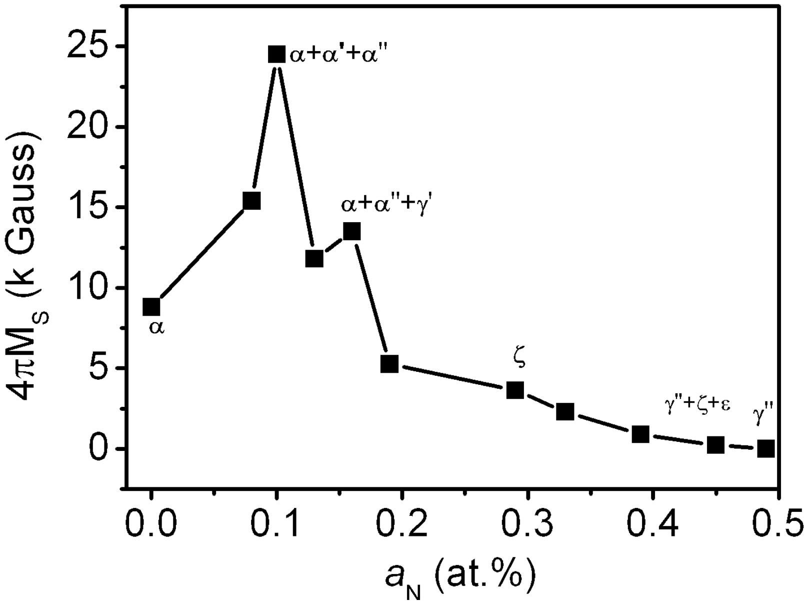

Figure 5.9 The $4\pi M_S$ of the films with different nitrogen concentration. The $4\pi M_S$ of the nitrogen-poor films are higher than those of the pure Fe film, while the $4\pi M_S$ of the nitrogen-rich films are lower.

With a further increase in the nitrogen concentration, nitrogen-rich phases such as ε and γ'' appear, and the $4\pi M_S$ decreases to a value that is even below that of the pure iron thin films. For sample III-1, which only exhibits γ'' phase in the XRD profiles, the $4\pi M_S$ is close to zero. This is consistent with the findings in regard to the Fe-N magnetic properties by Jiang *et al*[120] as well as with our theoretical prediction based on BBB correlation as described in section 5.1.

The nitrogen catalytic effect on the M_S can be summarized as follows:

(1) Poor nitrogen concentration enhances the M_S of iron films due to the change of the valance state.

(2) The M_S of the pure iron film is lower than the bulk value, which is consistent with the study on Ni thin films and the theoretical prediction for the size effect on the M_S of nanosolids as discussed in section 4.1.

(3) The physical size effect causes a drop in the M_S of a nanosolid. In contrast, the nitrogen catalytic effect enhances the M_S at low nitrogen concentration. In the thin iron films with low nitrogen concentration, joint effects of the size and nitrogen catalysis occur and the nitrogen catalytic effect becomes dominant. As a result, the M_S is enhanced to a level even higher than the bulk Fe value.

(4) If too much nitrogen is added to the iron films, the M_S decreases due to the decrease in the number of Fe^{dipole}, the formation of an H-bond-like formation, and the formation of different types of lattice with smaller exchange strength.

5.3.2 Coercivity and squareness

The H_C of the films is shown in Figure 5.10. With oscillations, the H_C tends to decrease slightly with the increase in the nitrogen concentration. Other properties such as the squareness and the remanence have no apparent dependence on the nitrogen concentration. The nitridation effects on the magnetic properties of iron films are summarized in Table 5.2.

5.3.3 Resistivity

Figure 5.11 shows the resistivity of Fe-N films as a function of the nitrogen concentration, measured using a four-point probe measuring system. With an

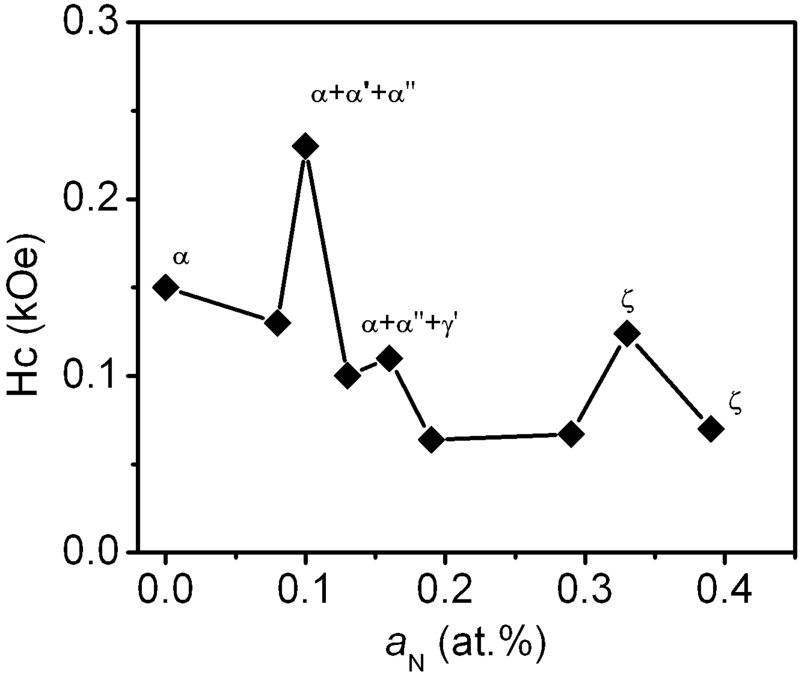

Figure 5.10 The nitrogen concentration dependence of the H_C of the Fe-N films. H_C tends to decrease with oscillation behavior when nitrogen increases.

Table 5.2 Summary of the magnetic properties of Fe-N films.[178]

Sample No.	Phases	Nitrogen concentration a_N (%)	$4\pi M_S$ (kG)	$4\pi M_r$ (kG)	H_{Cm} (kOe)	R_r	μ (μ_B)
Fe	α	0	8.8	8.5	0.15	0.97	0.9
II-1	$\alpha + \alpha'' + \gamma'$	0.16	13.5	13.1	0.11	0.97	-
II-2	$\alpha + \alpha'$	0.13	11.8	10.4	0.10	0.88	-
II-3	$\alpha + \alpha'$	0.10	24.5	15.3	0.23	0.62	2.5
II-4	$\alpha + \alpha'$	0.08	15.4	13.5	0.13	0.88	1.6
III-1	γ''	0.49	0	/	/	/	0
III-2	$\gamma'' + \zeta + \varepsilon$	0.45	0.223	0.041	-	0.18	-
III-3	ζ	0.39	0.896	0.229	0.07	0.26	0.15
III-4	ζ	-	-	-	-	-	-
III-5	ζ	0.33	2.286	1.27	0.124	0.56	-
III-6	$\alpha + \alpha''$	0.29	3.628	1.136	0.067	0.31	0.4
III-7	$\alpha + \alpha''$	0.19	5.253	2.519	0.064	0.10	0.6

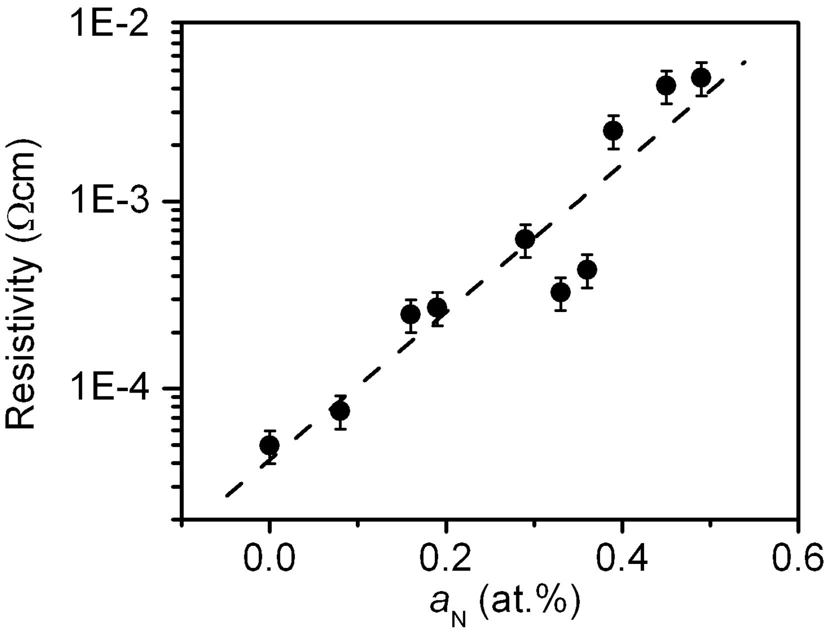

Figure 5.11 The resistivity of the Fe-N films increases exponentially with the increase of nitrogen concentration, which indicates the reduction of carrier concentration of iron and the formation of a band gap by nitriding. The dash line comes from a linear fitting.

increase of the nitrogen concentration, the resistivity of the films increases exponentially, which confirms the localization of the electrons and the formation of a band gap when nitrogen was introduced, as was discussed in section 5.1.2.

5.4 Extension: bias effect

The high ionization facilitates the control of the ion energy by biasing the substrate, which has a strong influence on the surface morphology and the microstructure of the coating.[204,205] Hence, in the case of the FCVA technique, the bias voltage is an important parameter. This section describes the study of the bias effect on the surface morphology, microstructure, and magnetic properties of the Fe-N films. The deposition details are given in section 3.3.3.

5.4.1 Deposition rate and surface morphology

The deposition rate was apparently affected by the bias voltages. At a floating potential, the deposition rate was 16.4 nm/min, but when the bias voltages were increased up to –50, –100, and –400 V, the deposition rates decreased to 16.0, 14.7, and 5.1 nm/min, respectively. The reduction of deposition rates with the increase in bias voltages indicates that the resputtering effect on the film surface is becoming intense due to the increase of ion energy. This is especially obvious in the deposition at a bias voltage of –400 V, which has a deposition rate only 31% of that at a floating potential.

The surface morphologies also change with the bias voltage. Figure 5.12 shows the AFM images of the films deposited at different substrate biases. As the bias voltage increased from 0 to –50 V, the surface remained smooth. With a further increase in bias voltage, the surface became roughened, indicating a significant coarsening of the film structure. The film deposited at a bias voltage of –100 V exhibited spherical-like clusters with a size of 15~40 nm. When deposited at a bias voltage of –400 V, the film possessed a cluster around 50 nm in size due to the coalescence. Figure 5.13 shows the influence of the bias voltage on the RMS of the films, calculated from the AFM image over an area of 500 nm × 500 nm. The roughness value first decreased to its lowest value of 0.14 nm with an increase of the bias voltage to –50 V, and then increased rapidly as the bias voltage increased up to –400 V.

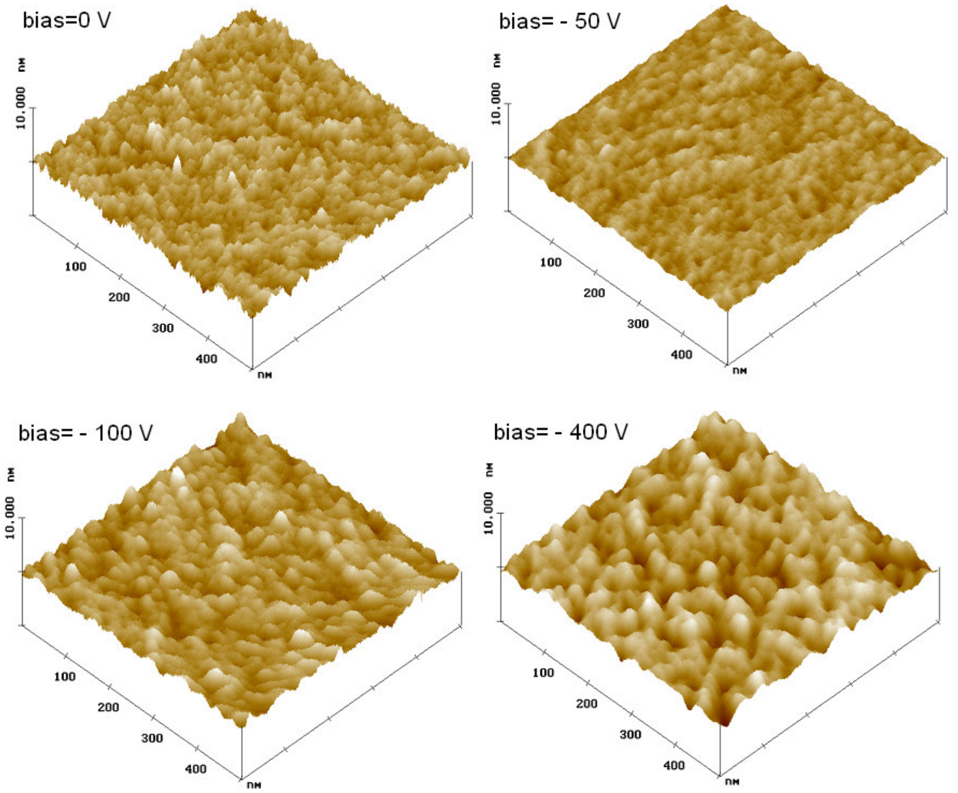

Figure 5.12 AFM images of the films deposited at various bias voltages.

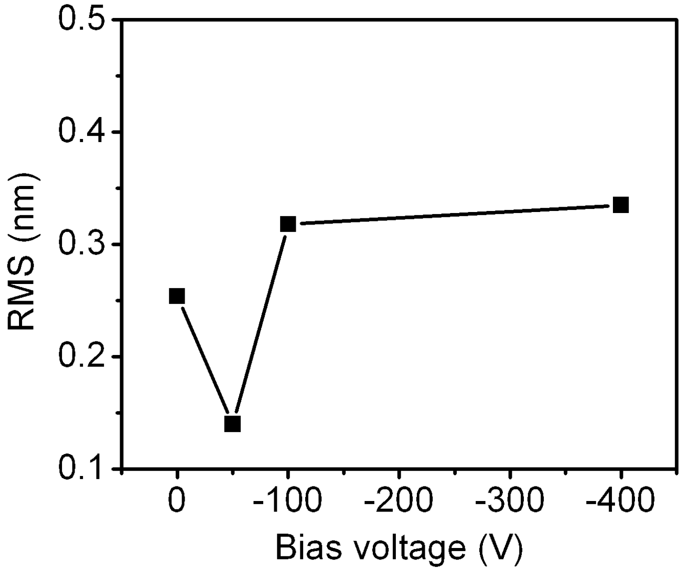

Figure 5.13 Bias dependence of surface roughness (RMS). The film deposited at –50 V bias voltage exhibits the lowest RMS value.

5.4.2 Microstructure

The XRD profiles in Figure 5.14 show three peaks at 44.3°, 64.6°, and 82.2°, corresponding to (110), (200), and (112) planes of α-Fe(N), respectively. According to the JCPDS-International diffraction database, the first three strongest peaks for pure α-Fe are at 44.8°, 65.2°, and 82.5°, respectively. The 2θ of the α-Fe(N) films shifts to a lower position, which is indicative of lattice expansion according to the Bragg equation of diffraction ($d = (\lambda/2)(1/\sin\theta)$), by incorporation of nitrogen into the α-Fe lattice.[103] The film deposited at a bias voltage of –50 V has the highest intensity for all peaks, indicating the best crystallinity among all the investigated samples. The relative peak intensities of (200) and (112) (I_{200} / I_{110} and I_{112} / I_{110}) are 46% and 54% for a randomly oriented iron according to the JCPDS-International diffraction database. However, the

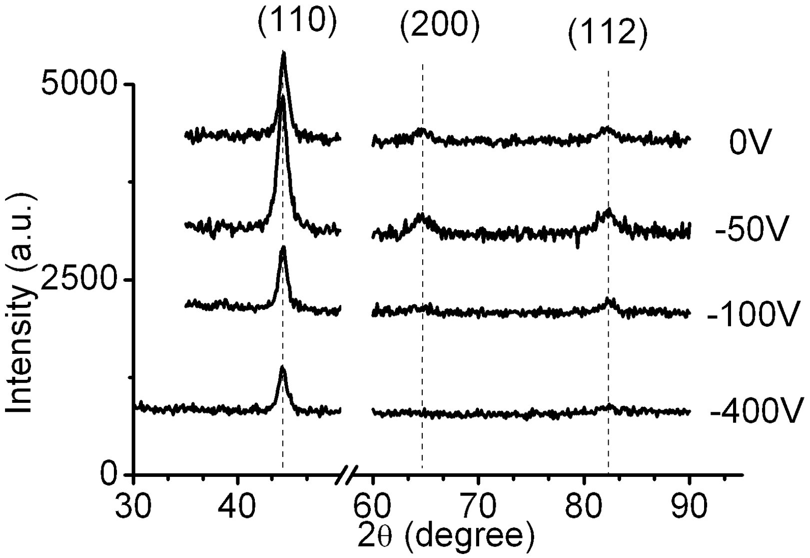

Figure 5.14 Bias dependence of the XRD profiles shows that the film deposited at –50 V bias voltage exhibits the highest intensity, indicating the best crystallinity among the samples.

values of the α-Fe(N) films in this study are much smaller: $I_{200} / I_{110} \leq 18\%$ and $I_{112} / I_{110} \leq 12\%$, indicating that the films possess a preferred orientation in the (110) plane. This is consistent with the findings of Takahashi *et al*[206] and Oda *et al*,[207] who also found the preferred (110) orientation in the Fe-N films deposited using the sputtering technique.

5.4.3 Magnetic properties

Figure 5.15 (a) shows the in-plane M-H loops of the films deposited using bias voltages of –50, –100, and –400 V. The loops exhibit a soft behavior with good squareness. The bias-voltage dependence of $4\pi M_S$ is shown in Figure 5.15 (b). The film deposited at the bias voltage of –50 V exhibits the largest value of $4\pi M_S$ (18 kG). With a further increase of the bias voltage, the $4\pi M_S$ decreases. The M_S changes according to the surface morphology and the microstructure. The highest $4\pi M_S$ of film being deposited at a bias voltage of –50 V is due to the relatively high crystallinity and low surface roughness of the film, which are consistent with those reported by Iwatsubo *et al.*[208]

5.4.4 Discussion

The mean ion charge state, q, for Fe is 1.82 and the intrinsic energy of Fe ions emitted from a cathode source E_0 is about 68 eV.[209] As the deposition pressure is relatively low (5×10^{-5} torr), the energy loss resulting from collisions between Fe ions and nitrogen gas molecules is negligible. Thus, the energy of Fe ions that reaches the substrate surface can be estimated as: $E_{\mathrm{Fe}} = E_0 - qV_b$, where V_b represents the applied substrate bias voltage. The energy of the ions that reach the substrate surface strongly affects the films quality. The energy of the ions can be

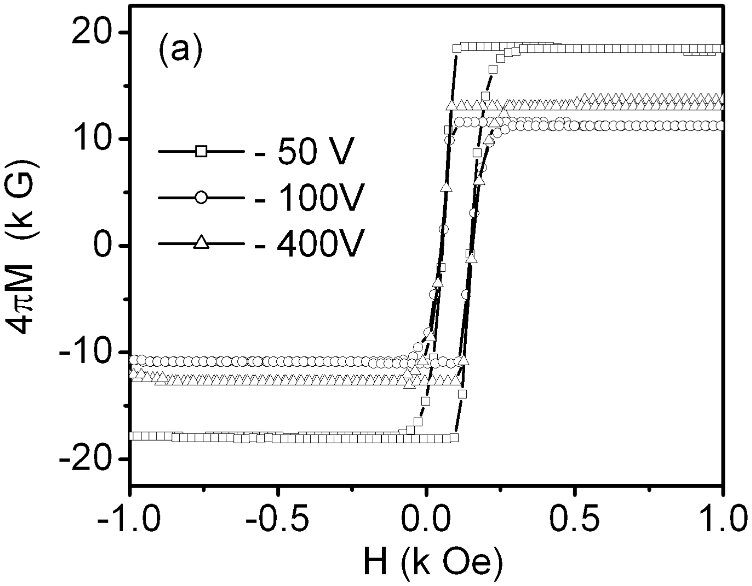

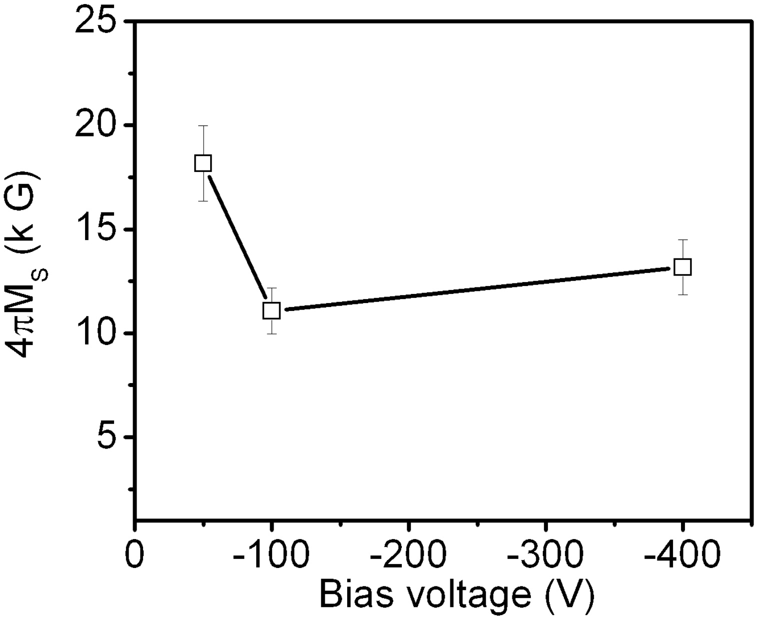

Figure 5.15 (a) The magnetic hysteresis loops of films deposited at bias voltage of –50, –100, and –400 V respectively. (b) Bias voltage effect on the $4\pi M_S$ of the films.

divided into three regions, which results in different surface morphologies and microstructures:

(1) When the bias voltage is zero, the energy of ions is low; the film grows with the ions accumulating on the surface. The resputtering effect is weak and the mobility of surface atoms is relatively low. The films hence have a rough surface and low crystallinity.

(2) When the bias voltage is −50 V, the energy of ions increases to an optimized level, the energetic ions then penetrate into the film subsurface and increase the mobility of the surface atoms. The vacancies near the surface that are produced by the bombarding ions are partially refilled by the newly arriving ions, which results in downward packing of material such that films grown in a densely packed structure have a smooth morphology, as was observed. However, the optimized bias voltage may vary from material to material. For example, instead of −50 V, as was observed in this study for Fe-N films, one study of the bias dependence of the surface of TiN films[210] found that film deposited at a bias voltage of −100 V had the lowest surface roughness.

(3) When the bias voltage is higher than –50 V, the energy of ions is too high and the bombardment and resputtering effect on the film surface become intense. The high-energy ions penetrate deeply into the films. The fast-dropping deposition rates that occur when the bias voltage increases to –100 and –400 V are evidence of the

intense resputtering effect. Ions with higher energy transfer more momentum energy to the film surface and increase the mobility of surface atoms, which leads to an increase of the surface roughness, as was observed. The intense bombardment and the deeply penetrated ions also damage the formed crystal, leading to a poor crystallinity.

CHAPTER 6 RESULTS AND DISCUSSION III: JOINT EFFECT OF PHYSICAL SIZE AND NITRODATION ON M_S

From the discussion in CHAPTER 4, we learnt that at ambient temperature, the M_S of a ferromagnetic nanosolid decreases with size, while the discussion in CHAPTER 5 indicated that nitridation could enhance the M_S of iron. This raises the question of whether the M_S enhancement of the nitridation could overcome the size-induced reduction of M_S. In this chapter, the joint effects of physical size and nitrogen catalysis on the thin Fe-N films are described. Three series of films were deposited, which were labeled Fe, Fe-(N-Poor), and Fe-(N-Rich) according to the nitrogen concentration. The detailed deposition conditions are shown in section 3.3.3.

6.1 Nitrogen-poor Fe-N films

The nitrogen concentration of the films calculated based on the XPS is about 8~10 at%. Figure 6.1 shows the XRD profiles of the samples. The profiles show three peaks at about 44.3°, 64.6°, and 82.2°, corresponding to (110), (200), and (112) planes of α-Fe(N), respectively. Figure 6.2 shows the substrate temperature's, T_S, effect on grain size, which increases with the T_S. At substrate temperatures of 110, 170, 230, 290, and 350^{o}C, the nanocrystalline grain sizes are about 4.5, 8.0, 8.3, 9.3, and 10.2 nm, respectively. This is easy to understand because a higher substrate temperature brings more energy to the deposited atoms, which benefits the grain growth.

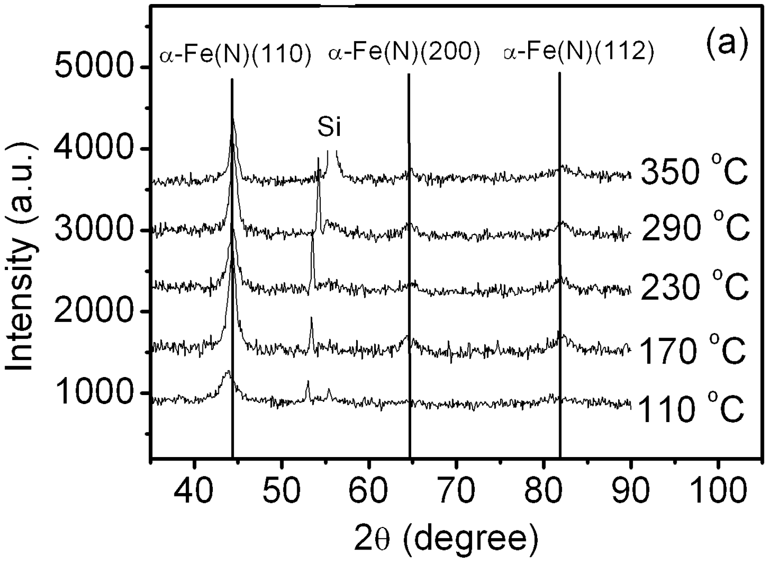

Figure 6.1 XRD profiles of Fe-(N-Poor) films with poor nitrogen concentration deposited at various substrate temperatures.

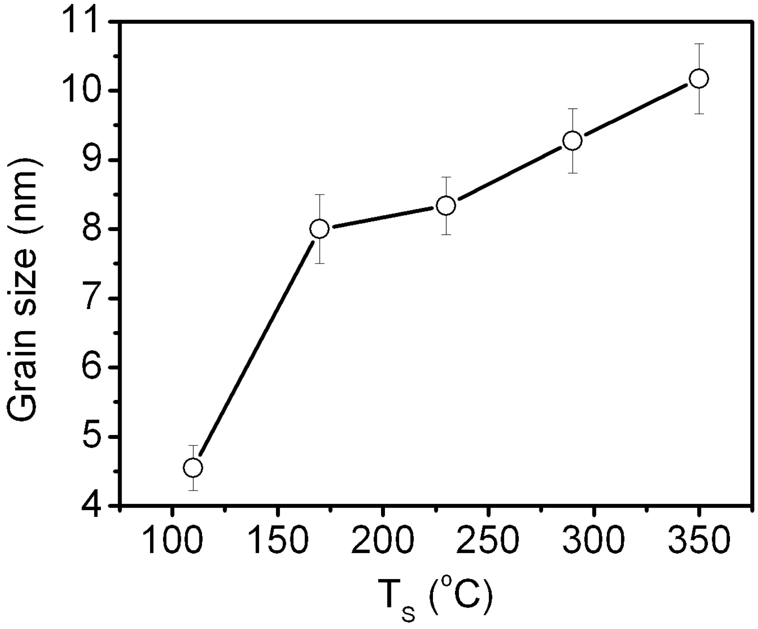

Figure 6.2 Substrate temperature T_S dependence of grain size of the Fe-(N-Poor) films.

Figure 6.3 shows the in-plane hysteresis loops of Fe-(N-Poor) films. The M_S decreases with the size, which is similar to those of Ni films, as discussed in section 4.3

6.2 Nitrogen-rich Fe-N films

Nitrogen-rich Fe-N films have a nitrogen concentration of ~30 at%. The XRD profiles in Figure 6.4 exhibit typical ζ-Fe_2N peaks such as (101), (002), and (100) at 2θ of 43.0, 40.9, and 37.0, respectively. The peaks become sharp and intense as the T_S increase. The calculated grain size shown in Figure 6.5 increases monotonically with T_S, being similar to that of the Fe-(N-Poor) films.

The grain size dependence of in-plane magnetization of Fe-(N-Rich) films at room temperature exhibits the same tendency of that in Fe-(N-Poor) films, as shown in Figure 6.6.

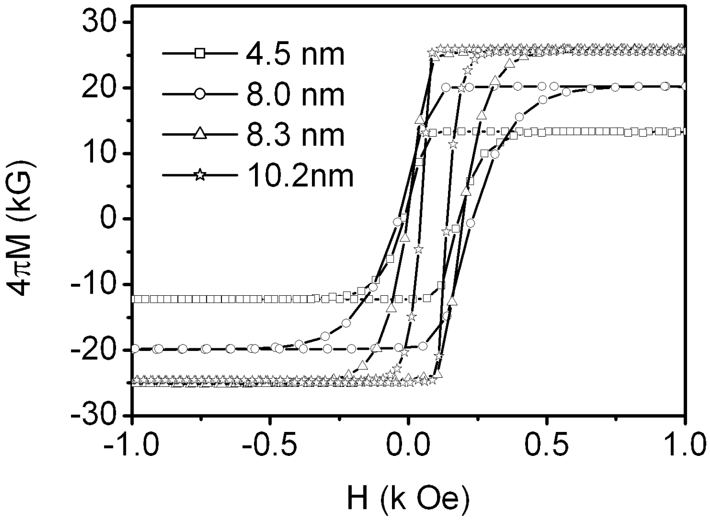

Figure 6.3 The M-H loops of low-nitrogen content films.

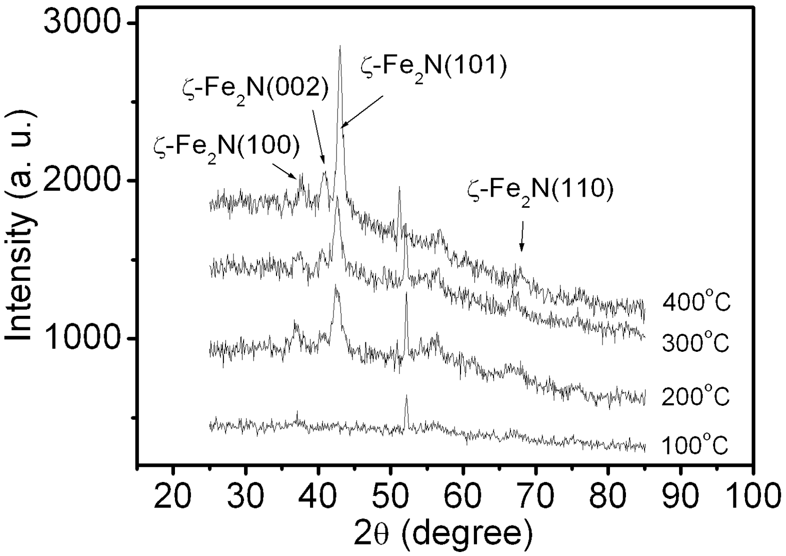

Figure 6.4 XRD profiles of Fe-N films at various substrate temperatures.

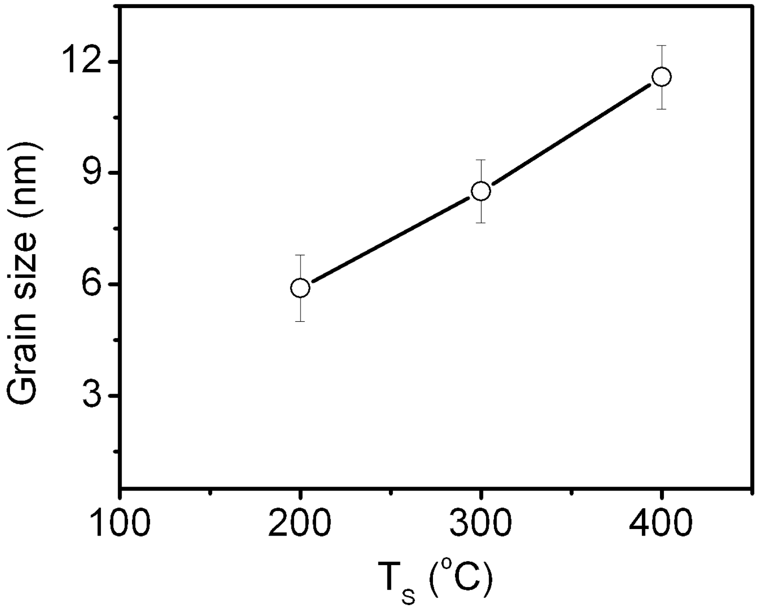

Figure 6.5 T_S dependence of the grain size of Fe-(N-Rich) films.

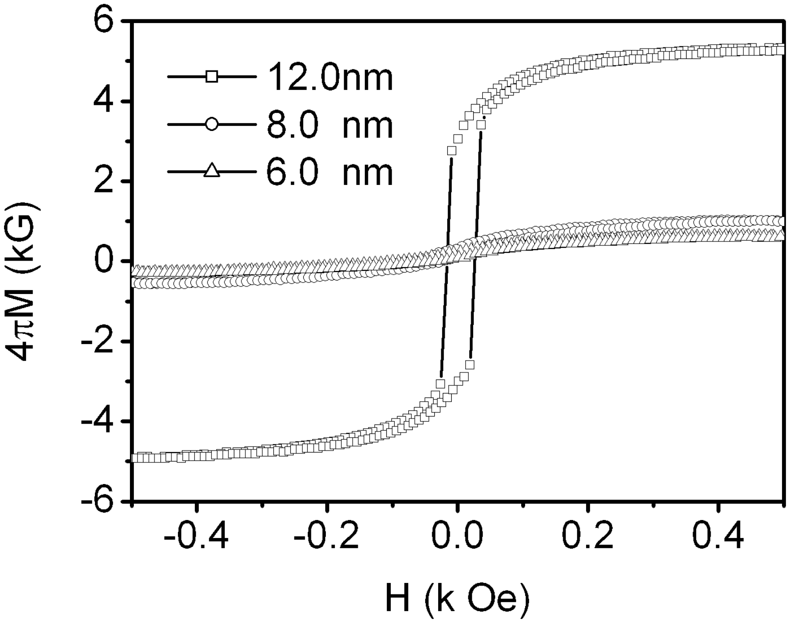

Figure 6.6 The M-H loops of Fe-(N-Rich) films of various grain sizes.

Figure 6.7 compares the size dependence of M_S for the nitrogen-poor and nitrogen-rich Fe-N films together with the pure iron thin films. The $4\pi M_S$ of all the films decrease with the grain size, which is consistent with the observations concerning Ni films as described in section 4.3. The BOLS theoretical predictions with $\alpha = 1.2$, 1.0, and 1.0 based on Eq (4.18) for Fe-(N-Poor), pure Fe, and Fe-(N-Rich) are also shown in Figure 6.7. During the theoretical calculation, the average bond lengths, d, for Fe-(N-Poor), pure Fe, and Fe-(N-Rich) were 0.251, 0.255, and 0.225 nm, respectively. The bulk $4\pi M_S(\infty)$ were 30.0, 22.2, and 8.0 kG, respectively.[103] The decrease in Ms for the Fe-(N-Rich) films with grain size of 8.0 and 6.0 nm is far from the predictions, which may be due to the sensitive of the VSM machine and the low crystallinity of the films

It can be seen that, with the same grain size, the $4\pi M_S$ of Fe-(N-Poor) films is always higher than that of the Fe films, while the $4\pi M_S$ of Fe-(N-Rich) films is always lower than that of the Fe films, indicating that poor nitrogen concentration introduced into the iron films enhances the magnetization, while an excess of nitrogen decreases it. When the grain size of Fe-(N-Poor) films is larger than 8.0 nm, the M_S is even higher than that of the bulk value of Fe ($4\pi M_S$ = 22.2 kG). This indicates that the enhancement of the M_S by nitridation can overcome the size-induced decrease of M_S at ambient. On the other hand, the $4\pi M_S$ of Fe-(N-Poor) films with a grain size below 8 nm is lower than that of the value of bulk iron; however, it is still higher than that of the Fe films with the same grain sizes, which indicates that when we investigate the nitrogen catalytic effect on the M_S of iron films, the size effect should be taken into consideration together with the nitridation effect.

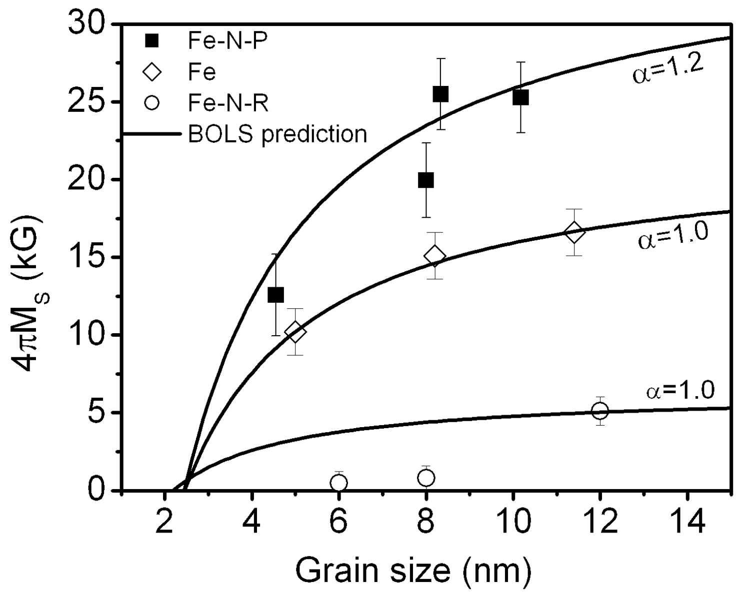

Figure 6.7 Physical size and nitrogen catalytic effect on the magnetization of iron thin films.

CHAPTER 7 Application of BOLS: T_C suppression of ferroelectric and superconducting nanosolids

This section shows that the model of T_C suppression for ferromagnetic nanosolids can be extended to the T_C suppression of ferroelectric and superconducting nanosolids, which have been widely observed.[211,212,213,214,215] For the T_C suppression of ferroelectric systems, such as $PbTiO_3$, $BaTiO_3$, $PbZrO_3$, and $BaTiO_3$, three different approaches[216] have been developed to investigate the occurrence of surface modes. They are: (1) a microscopic pseudospin theory based on the Ising model in a transverse field; (2) a classical and macroscopic Landau theory in which surface effects can be introduced phenomenologically; and (3) a polariton model appropriate for the very-long-wavelength region. Taking the surface and nonequilibrium energy into consideration, Zhong *et al*[217] extended the Landau-type phenomenologically classical theory by introducing a surface extrapolation length, δ, to the size-dependent T_C suppression of ferroelectric nanosolids. However, the model fails to explain the thermal properties of $PbTiO_3$ and $PbZrO_3$ nanosolids. Following this, Bursill *et al*[218] assumed that the phenomenological Landou-Ginzburg-Devonshire coefficients in the Gibbs energy would change with the particle size, thus solving this problem. An empirical equation widely used to fit the T_C suppression of ferroelectric nanosolids is given as:[211,213]

$$\Delta T_C(K_j)/T_C(\infty) = C/(K_j - K_C) \tag{7.1}$$

where C and the critical size, K_C, are adjustable parameters. Note that if $K_j = K_C$, Eq (7.1) corresponds to a singularity. (The correct form should be $K_j + K_C$

instead of K_j - K_C in Eq (7.1).) Zhong *et al*[219] considered the Ising model for the long-range interaction in dealing with the ferroelectric nanosolids by adjusting the σ in the exchange strength $J_{ij} = J/r_{ij}^{\sigma}$. $\sigma = 0$ corresponds to an infinite-range interaction and $\sigma = \infty$ corresponds to a nearest-neighbor interaction. More recently, Jiang *et al*[220] adapted their model for melting point suppression to the T_C suppression of the ferroelectric nanosolids, which is expressed as:

$$\frac{\Delta T_C(K_j)}{T_C(\infty)} = \exp(-\frac{2S_0}{R_s}\frac{1}{K_j/K_C - 1}) - 1 \tag{7.2}$$

where S_0 is the transition entropy and R_s is the idea gas constant. Numerical match for the T_C suppression of $BaTiO_3$ and $PbTiO_3$ nanosolids has been reached with the documented S_0 values. It was found by Jiang *et al*[220] that the larger K_C value corresponds to a smaller value of S_0.

The Curie temperature of a superconductive nanosolid is also suppressed by minimizing the particle size. The relation between the T_C and the energy-level spacing for spherical dots was suggested as follows:[221]

$$Ln\left(\frac{T_C(K_j)}{T_C(\infty)}\right) = \sum\left(\frac{2}{2M+1}\right)\left\{\tanh\left(\frac{\pi^2(2M+1)k_B T_C}{\delta}\right) - 1\right\} \tag{7.3}$$

where δ is the energy sublevel splitting in the conduction or valence band that can be estimated with the Kubo formula:[153] $\delta = 4E_F/3n \propto 1/V \propto K_j^{-3}$, where E_F is the fermi energy of the bulk materials and n is the number of valence/conduction electrons in the nanosolid. Index M is the magnetic quantum number. However, the T_C suppression of Pb embedded in the Al-Cu-V matrix measured by Tsai *et al*[215] could not fit this prediction. Instead, the trend of Pb T_C suppression follows A exp($-B/K_j$), with adjustable constants A and B. Briefly, the SSCL theory,[29] as introduced in section 2.1.2, considers the correlation length, and the CN-imperfection model[30] considers the loss of exchange bonds of atoms in the ferromagnetic surface region. A model for the T_C suppression of superconductive MgB_2 nanosolids[222,223,224] has yet to be developed. Nevertheless, all the models developed so far have contributed to the understanding of T_C suppression from various perspectives. Consistent insight and a unification of the T_C suppression of ferromagnetic, ferroelectric, and superconductive nanosolids are highly desirable. Here, we show that an extension of the BOLS correlation to high-order atomic CN in conjunction with the Ising model could solve this problem.

The same shell structure to that expressed in Eq (4.15) can be used. However, for the dipole-dipole exchange interaction in a ferroelectric material, we need to consider high-order CN imperfection. For a ferroelectric spherical dot with radius $R = K_j d$, we need to consider the interaction between the specific central atom and its surrounding neighbors within the critical volume $V_C = 4\pi K_C^3/3$, in addition to the BOLS correlation in the surface region. The ferroelectric property drops down from the bulk value to a value smaller than 5/16 (estimated from Figure 7.1 (b)) when one goes from the central atom to the edge along the radius. If the surrounding volume of the central atom is smaller than the critical V_C, the ferroelectrics of this central atom attenuate; otherwise, a bulk value remains. For an atom in the ith surface layer, the number of lost exchange bonds is proportional to the volume V_{vac}; that is, the volume difference between the two caps of the V_C-sized spheres as illustrated in Figure 7.1 (b). Therefore, the relative change of the ferroelectric exchange energy of an atom in the *i*th atomic layer compared to that of a bulk atom becomes:

$$\frac{\Delta E_{exc,i}}{E_{exc}(\infty)} = \frac{V_C - V_{vac}}{V_C} - 1 = -\frac{V_{vac}}{V_C} \tag{7.4}$$

Substituting Eq. (7.4) for the $z_{ib}c_i^{-m}$ in Eq. (4.16) and considering the BOLS correlation in the surface region, we have a universal form for ferromagnetic, ferroelectric, and superconductive nanosolids (m = 1 in the Ising model):

$$\frac{\Delta T_C(R)}{T_C(\infty)} = \frac{\Delta E_{exc}(R)}{E_{exc}(\infty)} = \begin{cases} \sum_{i\le 3} \gamma_i \left(z_{ib} c_i^{-1} - 1 \right) = \Delta_{coh} & (Ferromagnetic) \\ \sum_{i \le K_C} \gamma_i \left(\frac{-V_{vac}}{V_C} \right) + \Delta_{coh} = \Delta_{COH} & (else) \end{cases} \tag{7.5}$$

V_{vac} is the volume difference between the two spherical caps as illustrated in Figure 7.1. For the short spin-spin interaction, it is sufficient to sum over the

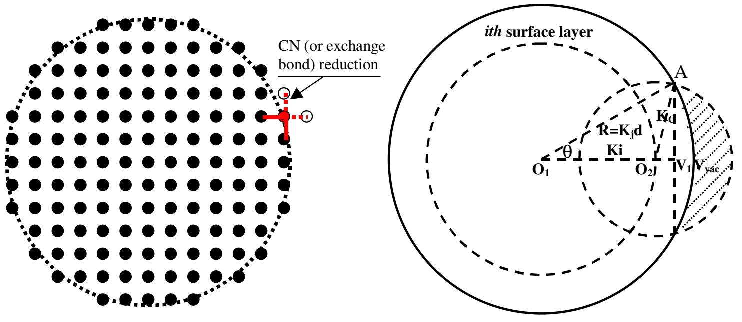

CN imperfection

High-order CN imperfection

Figure 7.1 Schematic illustration of (a) short-range exchange loss for ferromagnetic nanoparticle, where only the nearest neighbor is considered; and (b) high-order exchange bonds loss of an atom in a spherical nanosolid with radius $R = K_j d$. K_C is the critical radius; the lost V_{vac} (the shaded portion) is calculated by differencing the volumes of the two spherical caps:
$V_{vac} = \pi(K_C + K_i - K_j\cos\theta)^2(K_C - \frac{K_C + K_i - K_j\cos\theta}{3}) - \pi(K_j - K_j\cos\theta)^2(K_j - \frac{K_j - K_j\cos\theta}{3})$,
where the angle θ is determined by the triangle O_1O_2A.[90]

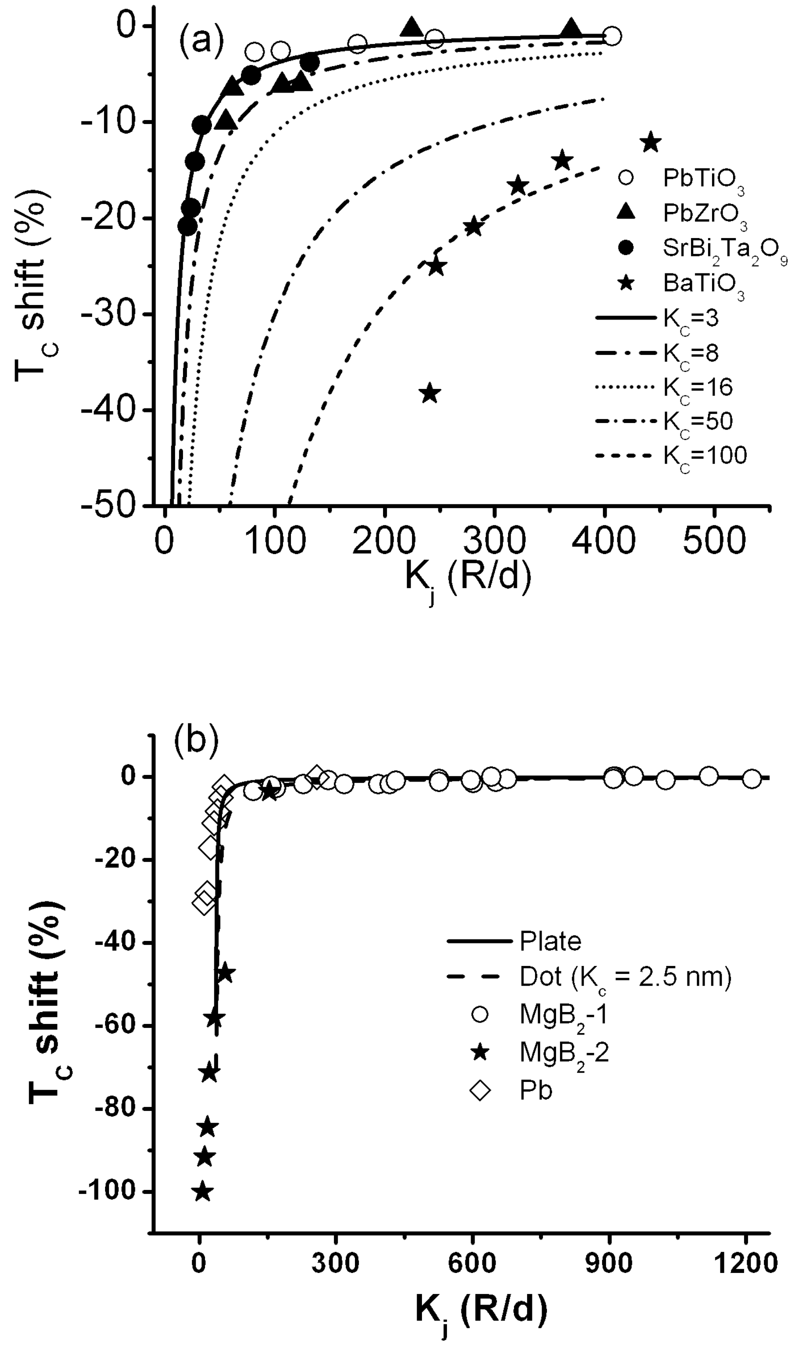

Figure 7.2 T_C suppression of (a) $PbTiO_3$,[212] $SrBi_2Ta_2O_9$,[213] $BaTiO_3$,[225] and $PbZrO_3$[226] nanosolids; and (b) superconductive MgB_2-1,[214] MgB_2-2,[227] and Pb[215] nanosolids. K_C is the critical correlation radius.[90]

outermost three atomic layers, whereas for a ferroelectric or a superconductive solid, the sum should be within the sphere of radius K_C. A C-language source code for the calculation of the loss of long-range exchange energy as in Eq (7.5) is attached in Appendix II.

Least-squares linearization of the measured size-dependent T_C represented by Eq. (7.1) gives the slope B' and an intercept that corresponds to the bulk $T_C(\infty)$. The measured data may need calibration by matching the intercept to the $T_C(\infty)$. Compared with Eq (7.5), one would find that $B' = R\Delta_{COH}$ for a ferroelectric system and then the adjustable K_C is obtained by computing optimization. For a ferromagnetic system, $B' = R\Delta_{coh}$, without needing numerical optimization. For a ferroelectric system, we need to optimize the K_C value in the computation to match the theoretical curve to the measured data. Figure 7.2 (a) shows the T_C suppression of ferroelectric $PbTiO_3$,[212] $SrBi_2Ta_2O_9$,[213] $BaTiO_3$, [225] and antiferroelectric $PbZrO_3$[226] nanosolids. Calculations of optimized K_C values for $PbTiO_3$, $PbZrO_3$, $BaTiO_3$, and $SrBi_2Ta_2O_9$ are listed in Table 7.1. For ferroelectric and superconductive nanosolids, $T_C = 0$ happens at $V_{vac} = V_C$, which means that the $K_j = K_C$ corresponds not to $T_C = 0$, but to a value that is too low to be detected. Figure 7.3 shows the K_C dependence of the T_C shift. For example, when $K_C = 5$, the bond contraction lowers the T_C by -41.1%, the volume loss contribution lowers the T_C by -53%, and the overall T_C shift is -94%. The difference in the optimized K_C using different approaches, as compared in Table 7.1, lies in that the slope (S/V ratio) in the current approach is not a constant but changes with the particle size.

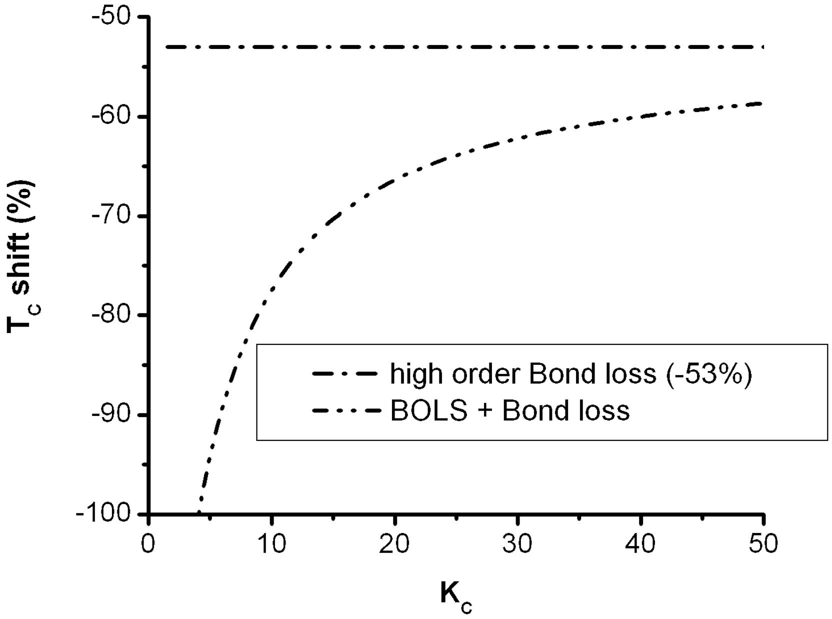

Figure 7.3 Critical correlation radius K_C dependence of the T_C shift of ferroelectric and superconductive alloying nanosolids. For the $K_C = 5$ example, the bond contraction lowers the T_C by -41.1% and the high-order bond lost (Bond lost) contribution that is a constant lowers the T_C by -53%, and the overall T_C shift is -94%. $K_C \leq 4$, $T_C = 0$.[90]

Applying the BOLS prediction to the scattered T_C suppression of superconductive MgB_2 nanosolids (Figure 7.2 (b)) leads to an estimation of the critical radius, $K_C = 3.5$, which agrees with that determined recently by Li *et al* (R_C ~1.25 nm).[227] The consistency of the BOLS prediction with the experiment data indicates that the long-range interaction dominates the superconductive T_C.

For Al-Cu-V-embedded Pb nanosolid,[215] the K_C is around 1, which is the same as that for a ferromagnetic solid. This finding provides a mechanism for the origin of the superconductive T_C suppression of MgB_2 nanosolids.

Table 7.1 Summary of information on the bulk atomic diameter, d, $T_C(\infty)$, and the critical radius K_C at which the central atom lost its ferroelectricity attenuates. $K_C \le 4$ corresponds to $T_C = 0$. The critical radius R'_C at which $T_C = 0$ is derived by other models.[90]

Materials	d/nm	T_C (∞)/K	K_C/R_C(nm)	R'_C/nm (Ref)
Fe	0.252	1043	1	0[10]
Co	0.250	1395	1	0[12]
Ni	0.248	631	1	0[85]
Fe_3O_4	0.222	860	1	0[79]
$PbTiO_3$	0.283	773	4/1.04	6.3[211], 4.5[212]
$SrBi_2Ta_2O_9$	0.270	605	4/1.0	1.3[213]
$PbZrO_3$	0.288	513	8/2.3	15[226]
$BaTiO_3$	0.243	403	100/24.3	24.5[228] 55[225]
MgB_2	0.352	41.7	3.5/1.25	1.25[227]
Pb	0.349	7.2	3.5/1.25	1.25[215]

CHAPTER 8 CONCLUSIONS and RECOMMENDATIONS

8.1 Conclusions

The physical size effect, the nitrogen catalytic effect, and their joint effect on the magnetic properties of iron nanosolids were studied using theoretical, simulative, and experimental approaches, which are summarized as follows:

- Theoretically, in the first-order approximation, using the concept of "molecular field," and incorporating the BOLS correlation mechanism into the Brillouin function, a model was developed to explain the T_C suppression and the size-induced M_S shift at various temperatures. Theoretical predictions for the size-induced H_C and nitridation effect on the M_S of iron films were also presented.
- Simulatively, the BOLS correlation premise was incorporated into the Ising model. Monte Carlo simulation was then carried out on the spin system with various cluster sizes and geometric shapes to verify the size-induced M_S shift and T_C shift.
- Experimentally, Ni, Fe, and Fe-N films were deposited using the FCVA technique, the size-induced H_C and M_S for nickel films at ambient temperature were examined as well as the nitridation effect on the M_S of iron films and the joint effect of physical size and nitridation on the M_S of Fe-N films.

The major findings include:

- Miniaturization of the ferromagnetic solid size lowers the T_C of a ferromagnetic nanosolid, in general, due to the tailoring of cohesive energy/exchange energy, which contributes to the spin order. This idea can also be applied to the T_C suppression of ferroelectric and superconducting nanosolids by extending the BOLS correlation to high-order CN imperfection.
- Incorporating the BOLS correlation premise into the Brillouin equation gives an expression for the size dependence of M_S at various temperatures. It is clarified for the first time that: (i) At very low temperatures, the M_S increases inversely with size due to the localization of the charges that contribute to the angular momentum, J, and hence the magnetic moment, μ, at the surface sites or at the sites surrounding defects. (ii) At temperatures in the vicinity of the T_C, the M_S decreases with the particle size due to the decrease in cohesive energy/exchange energy, which results in a lower level of spin order.
- The H_C of a freestanding ferromagnetic nanosolid may possess a superparamagnetic state. However, for nanocrystalline thin films, the intergrain exchange energy increases with the decrease in grain size, resulting in an increased H_C.
- When low nitrogen concentration is introduced into the iron films, the M_S is enhanced. It is even higher than that of the bulk pure iron when the nitrogen concentration is around 10%. However, excess nitrogen concentration decreases the M_S. The enhancement of the M_S originates from the formation of high magnetic moment iron valence states such as Fe^+ or even Fe^{dipole} when nitrogen is limited. If excess nitrogen is

introduced, the vanishing of Fe^{dipole} decreases the magnetization due to the electron's being captured by the nitrogen atom.

- Size-induced M_S reduction at ambient temperature may affect the applications of nanosolids; thin Fe-N films have the joint effect of the physical size and nitrogen catalysis. When the grain size is larger than ~8 nm, with low nitrogen concentration (~10 at%), the enhancement of nitridation overcomes the suppression of the physical size effect, leading to an M_S larger than that of the bulk Fe.
- Additionally, the FCVA technique has been proven to be a compatible technique for magnetic thin film deposition. It is versatile, flexible, and cost effective. By optimizing the parameters, such as bias voltages, substrate temperature, and working pressure, magnetic thin films with a smooth surface, a dense and nanocrystalline structure, and good magnetic properties can be obtained. In particular, the bias voltages that control the ions' energy affect the films' properties. –50 V is demonstrated to be an optimized deposition bias voltage for magnetic Fe-N films to obtain the smoothest surface, highest crystallinity, and, accordingly, the highest M_S.

The consistency between the theory predictions, Monte Carlo simulation, and the experimental observations not only reconciles the discrepancy of the observations but also deepens our insight into the physical origins of the size-induced M_S shift, T_C suppression, H_C shift, and the nitridation effect on M_S. The M_S and T_C relate to spin-spin exchange energy/cohesive energy, while the H_C relates to the intergrain exchange energy. The M_S also relates to the μ of individual atoms that is affected both by the charge localization due to bond contraction and by nitrogen addition, which alters the valence value of the Fe atoms. The study may prompt a more feasible mechanism for adjusting the magnetic behavior of the films by means of both physical shape and size and chemical reaction. Successful deposition of Fe-N films using FCVA technology amplifies the capacity of the FCVA technique in the reactive deposition of magnetic materials.

8.2 Recommendations for further research

Further study of the size effect of freestanding particles at various temperatures, especially very low temperatures, with precise controlling of the temperature will add to the understanding of nanomagnetism. Also, further study of magnetic nanostructural devices such as the giant magneto resistance with multilayers of Fe-N/Cr using Fe-N thin films may lead to new applications of Fe-N thin films.

The Ni and Fe-N films produced by the FCVA technique possess good magnetic properties with a smooth surface and a small crystalline size. The thin films of magnetic Ni, Fe, and Fe-N are very suitable for the seed layer of carbon nanotubes, which educes further study of the growth of carbon nanotubes and the corresponding applications based on them.

LIST OF PUBLICATIONS

1. **W. H. Zhong**, C. Q. Sun, B. K. Tay, S. Li, H. L. Bai, and E. Y. Jiang, "Curie temperature suppression of ferromagnetic nanosolids," *J. Phys. Condens. Matt.* 14, L399-L405 (2002).
2. **W. H. Zhong**, C. Q. Sun, and S. Li, "Size-effect on the magnetism of nanocrystalline Ni films at room temperature," *Solid State Commu*. 130, 603 (2004).
3. C. Q. Sun, **W. H. Zhong**, S. Li, and B. K. Tay, "Coordination imperfection suppressed phase stability of ferromagnetic, ferroelectric, and superconductive nanosolids," *J. Phys. Chem. B* 108(3) 1080 (2004).
4. **W. H. Zhong**, C. Q. Sun, S. Li, and B. K. Tay, "Monte Carlo study of size and temperature dependence of the magnetism of a ferromagnetic nanosolid with various crystal structures," *COMMUNICATED TO J. Phys. Chem. B.*
5. **W. H. Zhong**, C. Q. Sun, S. Li, H.L. Bai, and E.Y. Jiang, "Impact of bond order loss on surface and nanosolid magnetism," ACTA MATERIALIA, in press (2005).
6. **W. H. Zhong**, Y. Q. Fu, C. Q. Sun, S. P. Lau, B. K. Tay, and S. Li, "Substrate bias effect on the structural and magnetic properties of iron nitride films deposited using Filtered Cathode Vacuum Arc technique," *COMMUNICATED TO Surf. Coat. Tech.*
7. **W. H. Zhong**, B. K. Tay, S. P. Lau, X. W. Sun, S. Li, and C. Q. Sun, "Structural and magnetic properties of iron-nitride thin films deposited using a filtered cathodic vacuum arc," *Thin Solid Films,* 478, 61-6 (2005).

8. **W. H. Zhong**, S. P. Lau, B. K. Tay, S. Li, and C.Q. Sun, "Iron-nitride thin films deposited using filtered cathodic vacuum arc technique," Proceedings of the Symposium F (ISBN 981-238-372-7), *Int. Conf. Mater. Adv. Technol.*, 251-254, (2003).

Bibliography

---

[1] D. D. Awschalom, D. P. DiVincenzo, and J. F. Smyth, Science 258, 414 (1992). Macroscopic quantum effects in nanometer-scale magnets.

[2] N. M. White and J. D. Turner, Meas. Sci. Technol. 8, 1 (1997). Thick-film sensors: past, present and future.

[3] A. P. Ramirez, J. Phys.: Condens. Matter 9, 8171 (1997). Colossal magnetoresistance.

[4] R. F. Ziolo, U. S. Patent Specification, 4, 474, 866 (1984).

[5] R. H. Marchessault, S. Richard, and P. Rioux, Carbohydrate Res. 224, 133 (1992). In situ synthesis of ferrites in lignocellulosics.

[6] R. D. McMichael, R. D. Shull, L. J. Swartzendruber, L. H. Bennett, and R. E. Watson, J. Magn. Magn. Mater. 111, 29 (1992). Magnetocaloric effect in superparamagnets.

[7] F. G. Himpsel, J. E. Ortega, G. J. Mankey, R. F. Willis, Adv. in Phys. 47, 511-587 (1998). Magnetic nanostructures.

[8] A. Hernando, Eds., Nanomagnetism, 247 Series, E. Kluwer Academic, Dordrecht, Boston (1993).

[9] W. A. de Heer, Rev. Mod. Phys. 65, 611 (1993). The physics of simple metal clusters: Experimental aspects and simple models.

[10] Z. Q. Qiu, J. Person, and S. D. Bader, Phys. Rev. Lett. 70, 1006 (1993). Asymmetry of the spin reorientation transition in ultrathin Fe films and wedges grown on Ag(100).

[11] C. M. Schneider, P. Bressler, P. Schudter, and J. Kirschner, Phys. Rev. Lett. 64, 1059 (1990). Curie temperature of ultrathin films of fcc-cobalt epitaxially grown on atomically flat Cu(100).

[12] F. Huang, M. T. Kief, G. J. Mankey, and R. F. Willis, Phys. Rev. B 49, 3962 (1994). Magnetism in the few-monolayers limit: A surface magneto-optic Kerr-effect study of the magnetic behavior of ultrathin films of Co, Ni, and Co-Ni alloys on Cu(100) and Cu(111).

[13] J. T. Ou, F. Wang, and D. L. Lin, Phys. Rev. E 56, 2805 (1997). Critical behavior of magnetic films in the Ising model.

---

[14] Y. Li and K. Baberschke, Phys. Rev. Lett. 68, 1208 (1992). Dimensional crossover in ultrathin Ni(111) films on W(110).

[15] M. Tischer, D. Arvanitis, T. Yokoyanma, T. Lederer, L. Troger, and K. Baberschke, Surf. Sci. 307-309, 1096 (1994). Temperature dependent MCXD measurements of thin Ni films on Cu(100).

[16] L. H. Tjeng, Y. U. Idzerda, P. Rudolf, F. Sette, and C. T. Chen, J. Magn, Magn. Mater. 109, 288 (1992). Soft-X-ray magnetic circular dichroism: A new technique for probing magnetic properties of magnetic surfaces and ultrathin films.

[17] J. S. Jiang and C. L. Chien, J. Appl. Phys. 79, 5615 (1996). Magnetization and finite-size effects in Gd/W multilayers.

[18] J. S. Jiang, D. Davidovic, D. H. Reich, and C. L. Chien, Phys. Rev. Lett. 74, 314 (1995). Oscillatory superconducting transition temperature in Nb/Gd multilayers.

[19] G. G. Kenning, J. M. Slughter, and J. A. Cowen, Phys. Rev. Lett. 59, 2596 (1997). Finite-size effects in a CuMn spin-glass.

[20] W. A. De Heer, P. Milani, and A. Chatelain, Phys. Rev. Lett. 65, 488 (1990). Spin relaxation in small free iron clusters

[21] M. Guzman, J. L. Delplancke, G. J. Long, J. Delwiche, M. J. H. Franskin, and F. Grandjean, J. Appl. Phys. 92, 2634-2640 (2002). Morphologic and magnetic properties of $Pd_{100-x}Fe_x$ nanoparticles prepared by ultrasound assisted electrochemistry.

[22] T. Taniyama, E. Ohta, T. Sato, and M. Takeda, Phys. Rev. B 55, 977 (1997). Magnetic properties of Pd–2.9 at.% Fe fine particles.

[23] C. N. Chinnasamy, A. Narayanasamy, N. Ponpandian, K. Chattopadhyay, and M. Saravanakumar, Mater. Sci. & Eng. A 304, 408 (2001). Order-disorder studies and magnetic properties of mechanically alloyed nanocrystalline Ni_3Fe alloy.

[24] G. M. Cox, D. J. Trevor, R. L. Whetten, E. A. Rohifing, and A. Kaldor, Phys. Rev. B 32, 7290 (1985). Magnetic behavior of free-iron and iron oxide clusters.

[25] C. Y. Yang, K. H. Johnson, D. R. Salahub, J. Kaspar, and R. P. Messmer, Phys. Rev. B 24, 5673 (1981). Iron clusters: Electronic structure and magnetism.

[26] G. M. Pastor, J. Dorantes-Dvaila, and K. H. Benneman, Phys. Rev. B 40, 7642 (1989). Size and structural dependence of the magnetic properties of small 3d-transition-metal clusters.

[27] S. Ohnishi, A. J. Freeman, and M. Weinert, Phys. Rev. B 28, 6741 (1983). Surface magnetism of Fe(001).

[28] M. E. Fisher and M. N. Barber, Phys. Rev. Lett. 28, 1516 (1972). Scaling theory for finite-size effects in the critical region.

[29] D. S. Richie and M. E. Fisher, Phys. Rev. B 7, 480 (1973). Finite-size and surface effects in Heisenberg films.

[30] V. I. Nikolaev and A. M. Shipilin, Phys. Solid State 45, 1029-30, (2003). The influence of breaking of exchange bonds on the Curie temperature.

[31] J. Merikoski, J. Timonen, and M. Manninen, Phys. Rev. Lett. 66, 938 (1991). Ferromagnetism in small clusters.

[32] J. M. D. Coey, J. Appl. Phys. 76, 6632 (1994). The magnetization of bulk alpha $Fe_{16}N_2$.

[33] K. H. Jack, Proc. Royal Soc. London, Ser. A 208, 216 (1951).

[34] T. K. Kim and M. Takahashi, Appl. Phys. Lett. 20A, 492 (1972). New magnetic material having ultrahigh magnetic moment.

[35] W. Kiriake, K. Kuwahara, and H. Fujiyama, Surf. Coat. Tech. 98, 1293-1297 (1998). Preparation of iron nitride thin films by magnetron sputtering under surface magnetic field on substrates.

[36] S. K. Chattopadhyay, A. K. Meikap, K. Lal, D. Biswas, S. K. Chatterjee, M. Ghosh, K. Baba, and R. Hatada, Solid State Commun. 108, 977-982 (1998). Transport properties of iron nitride films prepared by ion beam assisted deposition.

[37] L. Rissanen, M. Neubauer, K. P. Lieb, and P. Schaaf, J. Alloy. Compd. 274, 74 (1998). The new cubic iron-nitride phase FeN prepared by reactive magnetron sputtering.

---

[38] A. Morisako, M. Matsumoto, and M. Naoe, J. Appl. Phys. 69, 5619 (1991). Magnetic anisotropy and soft magnetism of iron nitride thin films prepared by facing-target sputtering.

[39] J. F. Bobo, H. Chatbi, M. Vergnat, L. Hennet, O. Lenoble, P. Bauer, and M. Piecuch, J. Appl. Phys. 77, 5309 (1995). Magnetic and structural properties of iron nitride thin films obtained by argon-nitrogen reactive radio-frequency sputtering.

[40] D. C. Sun, C. Lin, E. Y. Jiang, and S. W. Wu, Thin Solid Film 260, 1 (1995). Multiphase iron nitride gradient films.

[41] K. Sumiyama, T. Sato, and G. M. Graham, Solid State Commun. 19, 403 (1976). Thickness dependence of magnetization in Fe-Ni Invar alloy film.

[42] G. Wedler and H. Schneck, Thin Solid Films 47, 147 (1977). Galvanomagnetic and magnetic properties of evaporated thin nickel films. II. Thickness dependence of the Hall coefficients, the magnetoresistivity and the saturation magnetization.

[43] S. Ohta, A. Terada, Y. Ishii, and S. Hattori, Transactions of the Institute of Electronics and Communication Engineers of Japan, Section E (English) E68, 173 (1985). Thickness dependence of magnetic properties and read-write characteristics for iron oxide thin films.

[44] J. P. Bucher, D. C. Douglass, and L. A. Bloomfield, Phys. Rev. Lett. 66, 3052 (1991). Magnetic properties of free cobalt clusters.

[45] L. A. Bloomfield, J. Deng, A. J. Cox, J. W. Emmert, F. K. Fatemi, H. Zhang, D. B. Haynes, J. G. Louderback, D. C. Douglass, J. P. Bucher, and A. M. Spencer, Conference: Magn. Electro. Correl. Local-Moment Sys.: Rare-Earth Elements and Comp. 16-18 Mar. 1998, Berlin, Germany, 153 (1998). Magnetic properties of isolated rare earth clusters.

[46] M. Konno, J. Phys. Soc. Japan 49, 1185 (1980). Anomalous thickness dependence of the saturation magnetization in Fe-Ni Invar alloy films.

[47] J. P. Chen, C. M. Sorensen, K. J. Klabunde, and G. C. Hadjipanayis, Phys. Rev. B 51, 11527 (1995). Enhanced magnetization of nanoscale colloidal cobalt particles.

[48] S. E. Apsel, J. W. Emmert, J. Deng, and L. A. Bloomfield, Phys. Rev. Lett. 76, 1441 (1996). Surface-enhanced magnetism in nickel clusters.

---

[49] D. H. Han, J. P. Wang, and H. L. Luo, J. Magn. Mang. Mater. 136, 176 (1994). Crystallite size effect on saturation magnetization of fine ferrimagnetic particles.

[50] I. Billas, A. Chatelain, W. A. de Heer, Science 265, 1682 (1994). Magnetism from the atom to the bulk in iron, cobalt, and nickel clusters.

[51] A. J. Freeman and R. Wu, Progress of Theoretical Physics Supplement 106, 397 (1991), Enhanced magnetic moment and magnetic ordering in MnNi and MnCu surface alloys.

[52] V. D. G. Laan, M. A. Hoyland, M. Surman, C. F. J. Flipse, and B. T. Thole, Phys. Rev. Lett. 69, 3827 (1992). Surface orbital magnetic moment of ferromagnetic nickel studied by magnetic circular dichroism in Ni 3p core level photoemission.

[53] A. Ney, P. Poulopoulos, and K. Baberschke, Europhysics Letters 54, 820 (2001). Surface and interface magnetic moments of Co/Cu(001).

[54] M. Albrecht, U. Gradmann, T. Furubayashi, and W. A. Harrison, Europhysics Letters 20, 65 (1992). Magnetic moments in rough Fe surfaces.

[55] U. Gradmann, T. Duerkop, and H. J. Elmers, J. Magn. & Magn. Mater. 165, 56 (1997). Magnetic moments and anisotropies in smooth and rough surfaces and interfaces.

[56] W. T. Geng, A. J. Freeman, and R. Q. Wu, Phys. Rev. B 63, 064427 (2001). Magnetism at high-index transition-metal surfaces and the effect of metalloid impurities: Ni(210).

[57] W. T. Geng, M. Kim, and A. J. Freeman, Phys. Rev. B 63, 245401 (2001). Multilayer relaxation and magnetism of a high-index transition metal surface: Fe(310).

[58] F. Liu, M. R. Press, S. N. Khanna, and P. Jena, Phys. Rev. B 39, 6914 (1989). Magnetism and local order: Ab initio tight-binding theory.

[59] P. J. Jensen and K. H. Bennemann, Z. Phys. D 35, 273 (1995). Theory for the atomic shell structure of the cluster magnetic moment and magnetoresistance of a cluster ensemble.

[60] J. Zhao, X. Chen, and G. Wang, Phys. Rev. B 50, 15424 (1994). Critical size for a metal-nonmetal transition in transition-metal clusters.

[61] J. Zhao, X. Chen, Q. Sun, E. Liu, and G. Wang, Phys. Lett. A 205, 308 (1995). A simple d-band model for the magnetic property of ferromagnetic transition-metal clusters.

[62] F. Aguilera-Granja, J. M. Montejano-Carrizales, and J. L. Morán-López, Phys. Lett. A 242, 255 (1998). Magnetic moments of iron clusters: A simple theoretical model.

[63] F. Liu, S. N. Kbanna, and P. Jena, Phys. Rev. Lett. 67, 742 (1991). Magnetic behavior of clusters of ferromagnetic transition metals.

[64] J. M. Montejano-Carrizales, F. Aguilera-Granja, and J. L. Moran-Lσpez. Nanostruct. Mat. 8, 269 (1997). Direct enumeration of the geometrical characteristics of clusters.

[65] K. Kempter, I. Maurer, and H. Harms, Applied Physics 7, 7-9 (1975). Saturation magnetization of MnBi films with different thicknesses and composition.

[66] P. Morrall, F. Schedin, S. Langridge, J. Bland, M. F. Thomas, and G. Thornton, J. Appl. Phys. 93, 7960 (2003). Magnetic moment in an ultrathin magnetite film.

[67] I. L. M. Billas, J. A. Becker, A. Châtelain, and W. A. de Heer, Phys. Rev. Lett. 71(24), 4067 (1993). Magnetic moments of iron clusters with 25 to 700 atoms and their dependence on temperature.

[68] I. M. L. Billas, A. Châtelain, and W. A. de Heer, J. Magn. Magn. Mater. 168, 64-84 (1997). Magnetism of Fe, Co and Ni clusters in molecular beams.

[69] Y. Qiang, R. F. Sabiryanov, S. S. Jaswal, Y. Liu, H. Haberland, and D. J. Sellmyer, Phys. Rev. B 66, 064404 (2002). Manetism of Co nanocluster films.

[70] R. H. Kodama, A. E. Berkowitz, E. J. McNiff, Jr., and S. Foner, Phys. Rev. Lett. 77 394 (1996). Surface spin disorder in $NiFe_2O_4$ nanoparticles.

[71] R. H. Kodama, A. E. Berkowitz, E. J. McNiff, Jr., and S. Foner, J. Appl. Phys. 81, 5552 (1997). Surface spin disorder in ferrite nanoparticles (invited).

[72] R. H. Kodama and A. E. Berkowitz, Phys. Rev. B 59, 6321 (1999). Atomic-scale magnetic modeling of oxide nanoparticles.

[73] N. Morita and N. Tanivama, J. Phys. Soci. Jap. 27, 1438 (1969). Curie temperature of nickel films evaporated in ultra-high vacuum.

---

[74] W. Durr, M. Taborelli, O. Paul, R. Germar, W. Gudat, D. Pescia, and M. Landolt, Phys. Rev. Lett. 62, 206 (1989). Magnetic phase transition in two-dimensional ultrathin Fe films on Au(100).

[75] Z. Q. Qiu, J. Person, and S. D. Bader, Phys. Rev. Lett. 67, 1646 (1991). Magnetic phase transition of ultrathin Fe films on Ag(111).

[76] R. Bergholz and U. Gradmann, J. Magn. Magn. Mater. 45, 389 (1984). Structure and magnetism of oligatomic Ni(111)-films on Re(0001).

[77] Y. Li, M. Farle, and K. Banerschke, Phys. Rev. B 41, 9596 (1990). Critical spin fluctuations and Curie temperatures of ultrathin Ni(111)/W(110): A magnetic-resonance study in ultrahigh vacuum.

[78] M. Farle, K. Baberschke, U. Setter, A. Aspelmeier, and F. Gerhardter, Phys. Rev. B 47, 11571 (1993). Thickness-dependent Curie temperature of Gd(0001)/W(110) and its dependence on the growth conditions.

[79] B. Sadeh, M. Doi, T. Shimizu, and M. J. Matsui, J. Magn. Soc. Jpn. 24, 511 (2000). Dependence of the Curie temperature on the diameter of Fe_3O_4 ultra-fine particles.

[80] D. Michels, C. E. Krill III, and R. Birringer, J. Magn. Magn. Mater. 250, 203-211 (2002). Grain-size-dependent Curie transition in nanocrystalline Gd: The influence of interface stress.

[81] W. G. Chu, G. H. Rao, H. F. Yang, G. Y. Liu, and J. K. Liang, J. Alloy. Compd. 335, 16 (2002). Formation, structure and magnetic properties of $GdFe_{11}Re$.

[82] W. Cai, M. Zhang, S. Arajs, and H. F. Helbig, J. Phys. Chem. Solid. 57, 175 (1996). Finite-size effects in thin gadolinium films.

[83] M. N. Barber, Phase Transitions and Critical Phenomena, C. Domb and J. Lebowita, Eds., Academic, New York (1983), Vol. 8.

[84] K. Binder and P. C. Hohenberg, Phys. Rev. B 9, 2194 (1974). Surface effects on magnetic phase transitions.

[85] F. Huang, G. J. Mankey, M. T. Kief, and R. F. Willis, J. Appl. Phys. 73, 6760 (1993). Finite-size scaling behavior of ferromagnetic thin films.

[86] R. J. Zhang and R. F. Willis, Phys. Rev. Lett. 86, 2665 (2001). Thickness-dependent Curie temperatures of ultrathin magnetic films: Effect of the range of spin-spin interactions.

[87] A. Manaf, R. A. Buckley, H. A. Davies, and M. Leonowicz, J. Magn. Magn. Mater. 101, 360 (1991). Enhanced magnetic properties in rapidly solidified Nd-Fe-B based alloys.

[88] M. S. Seehra and A. Punnoose, Solid State Commu. 128, 299 (2003). Particle size dependence of exchange-bias and coercivity in CuO nanoparticles.

[89] K. V. P. M. Shafi, A. Gedanken, R. Prozorov, A. Revesz, and J. Lendvai, J. Mater. Res. 15, 332 (2000). Preparation and magnetic properties of nanosized amorphous ternary Fe-Ni-Co alloy powders.

[90] C. Q. Sun, W. H. Zhong, S. Li, and B. K. Tay, J. Phys. Chem. B 108(3), 1080 (2004). Coordination imperfection suppressed phase stability of ferromagnetic, ferroelectric, and superconductive nanosolids.

[91] J. Degauque, B. Astié, J. L. Porteseil, and R. Vergne, J. Magn. Magn. Mater. 26, 261 (1982). Influence of the grain size on the magnetic and magnetomechanical properties of high-purity iron.

[92] G. Herzer, IEEE Trans. Magn. 26, 1397 (1990). Grain size dependence of coercivity and permeability in nanocrystalline ferromagnets.

[93] F. Sato, N. Tezuka, T. Sakurai, and T. Miyazaki, IEEE Translation Journal on Magnetics in Japan 9, 100 (1994). Grain diameter and coercivity of Fe, Ni, and Co metals.

[94] R. Alben, J. J. Becker, and M. C. Chi, J. Appl. Phys. 49, 1653 (1978). Random anisotropy in amorphous ferromagnets.

[95] J. Sort, B. Dieny, M. Fraune, C. Koenig, F. Lunnebach, B. Beschoten, and G. Güntherodt, Appl. Phys. Lett. 84, 3696 (2004). Perpendicular exchange bias in antiferromagnetic-ferromagnetic nanostructures.

[96] K. Kondo, T. Chiba, and S. Yamada, J. Magn. Magn. Mater. 254, 541 (2003). Effect of microstructure on magnetic properties of Ni-Zn ferrites.

[97] J.C Tang, A.H. Wu, X.Y.. Mao, S.D.. Li, W.L.. Gao, and Y.W. Du, J. Phys. D: Appl. Phys. 37, 151 (2004). Effects of hot isothermal pressing on the microstructures and soft magnetic properties of nanocrystalline $Fe_{86}Zr_7B_6Cu_1$ ribbons.

[98] S. H. See, H. L. Seet, X. P. Li, J. Y. Lee, K. Y. T. Lee, S. H. Teoh, and C. T. Lim, Materials Science Forum 437, 53 (2003). Effect of nanocrystalline electroplating of NiFe on the material permeability.

---

[99] M. Guyot, M. Rouabhi, R. Krishnan, M. Porte, H. Niedoba, and V. Cagan, J. Appl. Phys. 73, 5604 (1993). Domain wall pinning in amorphous CoZrNb films.

[100] D. Nuetzel, G. Rieger, J. Wecker, J. Petzold, and M. Mueller, J. Magn. Magn. Mater. 196-197, 327 (1999). Nanocrystalline soft magnetic composite-cores with ideal orientation of the powder-flakes.

[101] F. Mazaleyrat, V. Leger, R. Lebourgeois, R. Barrue, IEEE Transactions on Magnetics 38, 3132 (2002). Permeability of soft magnetic composites from flakes of nanocrystalline ribbon.

[102] P. Schaaf, Prog. Mater. Sci. 47, 1 (2002). Laser nitriding of metals.

[103] J. M. D. Coey and P. A. I. Smith, J. Magn. Magn. Mater. 200, 405 (1999). Magnetic nitrides.

[104] M. A. Russak, C. V. Jahnes, E. Klokholm, J.-W. Lee, M. E. Re, and B. C. Webb, J. Magn. Magn. Mater. 104-107, 1851 (1992). Magnetic and structural characterization of sputtered FeN multilayer films.

[105] H. Takahashi, H. Shoji, and M. Takahashi, J. Magn. Magn. Mater. 174, 57 (1997). Structure and magnetic moment of $Fe_{16}N_2$ sputtered film.

[106] S. Wang and M. H. Kryder, J. Appl. Phys. 67, 5134 (1990). rf-diode-sputtered iron nitride films for thin-film recording head materials.

[107] T. Ohgai, R. Shimono, H. Saitoh, and Y. Hayashi, Mater. Trans. Jpn. Inst. Met. 38, 503 (1997). Structure and soft magnetic properties of Fe-N thin films RF-sputtered on heated substrate.

[108] N. Terada, Y. Hoshi, and S. Yamanaka, IEEE Trans. Magn. 20, 1451 (1984). Synthesis of iron-nitride films by means of ion beam deposition.

[109] M. Q. Huang, W. E. Wallace, S. Simizu, and S. G. Sankar, J. Magn. Magn. Mater. 135, 226 (1994). Magnetism of α-FeN alloys and α-($Fe_{16}N_2$) Fe nitrides.

[110] Y. Sugita, H. Takahashi, M. Komuro, K. Mitsuoka, and A. Sakuma, J. Appl. Phys. 76, 6637 (1994). Magnetic and Mössbauer studies of single-crystal $Fe_{16}N_2$ and Fe-N martensite films epitaxially grown by molecular beam epitaxy (invited).

[111] M. A. Brewer, C. J. Escher, K. M. Krishnan, T. Kobayashi, and A. Nakanishi, J. Appl. Phys. 81, 4128 (1997). Magnetic and physical microstructure of $Fe_{16}N_2$ films grown epitaxially on Si(001).

[112] S. Okamoto, O. Kitakami, and Y. Shimoda, J. Appl. Phys. 79, 1678 (1996). Characterization of epitaxially grown Fe-N films by sputter beam method.

[113] H. Tanaka, S. Nagakura, Y. Nakamura, and Y. Hirotsu, Acta Mater. 45, 1401 (1997). Electron crystallography study of tempered iron-nitrogen martensite and structure refinement of precipitated α-$Fe_{16}N_2$.

[114] L. Rissanen, K. P. Lieb, M. Niederdrenk, O. Schulte, and P. Schaaf, Conference Proceedings: V50 International Conference on the Application of the Mossbauer Effect. ICAME-95, Ortalli, I.-Boloogna, Italy, 595 (1996).

[115] Y. Kong, J. Phys.: Cond. Matt. 12, 4161 (2000). Electronic structure and magnetism of equiatomic FeN.

[116] M. Komuro, Y. Kozono, M. Hanazono, and Y. Sugita, J. Appl. Phys. 67, 5126 (1990). Epitaxial growth and magnetic properties of $Fe_{16}N_2$ films with high saturation magnetic flux density (invited).

[117] K. Nakajima and S. Okamoto, Appl. Phys. Lett. 56(1), 92 (1990). Large magnetization induced in single crystalline iron films by high-dose nitrogen implantation.

[118] M. Takahashi and H. Shoji, J. Magn. Magn. Mater. 208, 145 (2000). α''-$Fe_{16}N_2$ problem – giant magnetic moment or not.

[119] K. Shiiki, H. Nakajima, and Y. Ohashi, J. Magn. Magn. Mater. 167, 259 (1997). Effect of N atom and lattice constant on electronic structures and magnetic properties of $Fe_{16}N_2$ calculated by band structure calculation based on local-density approximation.

[120] E. Y. Jiang, C. Q. Sun, J. E. Li, and Y. G. Liu, J. Appl. Phys. 65(4), 1659 (1989). The structures and magnetic properties of FeN films prepared by the facing targets sputtering method.

[121] J. Q. Xiao and C. L. Chien, Appl. Phys. Lett. 64, 384 (1994). Radio frequency reactive sputtered iron nitrides using ammonia gas: Structure and magnetic properties.

---

[122] Y. Utsushikawa and K. Niizuma, J. Alloy. Compd. 222, 188 (1995). The saturation magnetization of Fe-N films prepared by nitriding treatment in N_2 plasma.

[123] M. Niederdrenk, P. Schaaf, K. P. Lieb, and O. Schulte, J. Alloy. Compd. 237, 81 (1996). Characterization of magnetron-sputtered εiron-nitride films.

[124] O. Alvarez-Fregoso, E. Camps, J. L. García, J. A. Chávez-Carvayar, and J. A. Juárez-Islas, Surf. Coat. Tech. 94-95, 255 (1997). FeN and FeN-H thin films prepared by ECR microwave plasma nitriding.

[125] L. Guibin, L. Guoqing, L. Minkai and L. Bangzhi, Surf. Coat. Tech. 96, 34 (1997). Formation of nanometer magnetic iron nitride film by IBED.

[126] X. Z. Ding, F. M. Zhang, J. S. Yan, H. L. Shen, X. Wang, X. H. Liu, and D. F. Shen, J. Appl. Phys. 82(10), 5154 (1997). Synthesis and magnetic properties of iron nitride films deposited on Ge(100) by reactive ion beam sputtering.

[127] X. Z. Ding, F. M. Zhang, Y. L. Sun, Z. Y. Zhou, J. S. Yan, H. L. Shen, X. Wang, X. H. Liu, and D. F. Shen, Surf. Coat. Technol. 103-104, 156 (1998). Soft magnetic properties of ion beam reactively sputtered Fe-N thin films on Ge(100).

[128] I. Paseka, P. Bezdička, A. Kláriková, and K. Závěta, J. Alloy. Compd. 274, 248-253 (1998). Structure and magnetic properties of ball-milled iron nitride powders.

[129] A. Lančok, K. Závěta, S. Vratislav, P. Bezdika, and I. Paseka, J. Magn. Magn. Mater. 215-216, 30 (2000). Dependence of the magnetic moment of iron nitrides on the presence of defect phase.

[130] T. Yamaguchi, M. Sakita, M. Nakamura, and T. Kobira, J. Magn. Magn. Mater. 215-216, 529 (2000). Synthesis and characteristics of Fe_4N powders and thin films.

[131] Y. Jirásková, S. Havlíček, O. Schneeweiss, V. Peřina, and C. Blawert, J. Magn. Magn. Mater. 234, 477 (2001). Characterization of iron nitrides prepared by spark erosion, plasma nitriding, and plasma immersion ion implantation.

[132] S. Iwatsubo and M. Naoe, Vacuum 66, 251 (2002). Characteristics of Fe-N films deposited by a reactive ion beam sputtering using adsorptive and ionized nitrogen.

[133] S. Yu. Grachev, D. M. Borsa, and D. O. Boerma, Surf. Sci. 515, 359 (2002). On the growth of magnetic Fe_4N films.

[134] S. R. Kappaganthu and Y. Sun, Surf. Coat. Technol. 167, 165 (2003). Effect of nitrogen partial pressure and temperature on RF sputtered Fe-N films.

[135] X. Wang, W. T. Zheng, and L. J. Gao, Mater. Chem. Phys. 82, 254 (2003). The universality classes in growth of iron nitride thin films deposited by magnetron sputtering.

[136] H. B. Nie, S. Y. Xu, C. K. Ong, Q. Zhan, D. X. Li, and J. P. Wang, Thin Solid Films 440, 35 (2003). In-plane magnetic anisotropy in RF sputtered Fe-N thin films.

[137] J. S. He, Y. M. Zhou, W. Y. Lai, and C. Y. Pan, Phys. Rev. B 52, 6193 (1995). Electronic structure and enhancement of magnetic moments in the ferromagnetic nitride $Fe_{16}N_2$.

[138] A. Sakuma, J. Magn. Magn. Mater. 102, 127 (1991). Self-consistent calculations for the electronic structures of iron nitrides, Fe_3N, Fe_4N and $Fe_{16}N_2$.

[139] B. I. Min, Phys. Rev. B 46, 8232 (1992). Enhancement of Fe magnetic moments in ferromagnetic $Fe_{16}N_2$.

[140] S. Ishida and K. Kitawatase, J. Magn. Magn. Mater. 104, 1933 (1991). Electronic structures and magnetic properties of iron nitrides.

[141] M. Sifkovits, H. Smolinski, S. Hellwig, and W. Weber, J. Magn. Magn. Mater. 204, 191 (1999). Interplay of chemical bonding and magnetism in Fe_4N, Fe_3N and ζ-Fe_2N.

[142] J. M. D. Coey, K. O'Donnel, Q. Qi, E. Touchain, and K. H. Jack, J. Phys.: Condens. Matter 6, L23 (1994). The magnetization of alpha$Fe_{16}N_2$.

[143] P. Bezdicka, A. Klarikova, I. Paseka, and K. Zaveta, J. Alloy. Compd. 274, 10 (1998). Magnetic properties of α-FeN_x and α-$Fe_{16}N_2$ nitrides.

[144] M. Komura, H. Hoshiya, M. Mitsuoka, Y. Kozono, M. Hanazono, and Y. Sugita, J. Appl. Phys. 67, 5126 (1990). Epitaxial growth and magnetic

properties of $Fe_{16}N_2$ films with high saturation magnetic flux density (invited).

[145] Y. Sugita, M. Mitsuoka, M. Komura, H. Hoshiya, Y. Kozono, and M. Hanazono, J. Appl. Phys. 70, 5977 (1991). Giant magnetic moment and other magnetic properties of epitaxially grown $Fe_{16}N_2$ single-crystal films (invited).

[146] Y. Sugita, H. Takahashi, M. Komuro, M. Igarashi, R. Imura, and T. Kambe, J. Appl. Phys. 79, 5576 (1996). Magnetic and electrical properties of single-phase, single-crystal $Fe_{16}N_2$ films epitaxially grown by molecular beam epitaxy (invited).

[147] H. Shinno and K. Saito, Surf. Coat. Technol. 103-104, 129 (1998). Effects of film thickness on formation processes of $Fe_{16}N_2$ in nitrogen ion-implanted Fe films.

[148] K. Nakajima and S. Okamoto, J. Appl. Phys. 65, 4357 (1989). Formation of ferromagnetic iron nitrides in iron thin films by high-dose nitrogen ion implantation.

[149] S. Okamoto, O. Kitakami, and Y. Shimada, J. Appl. Phys. 79, 5250 (1996). α-$Fe_{16}N_2$ phase epitaxially grown by sputter beam method.

[150] Z. Y. Yao, H. Jiang, Z. K. Liu, D. D. Huang, F. G. Qin, S. C. Zhu, and Y. X. Sun, J. Magn. Magn. Mater. 177-181, 1291 (1998). Formation and magnetic properties of $Fe_{16}N_2$ films prepared by ion-beam-assisted deposition.

[151] D. M. Borsa, S. Grachev, J. W. J. Kerssemakers, and D. O. Boerma, J. Magn. Magn. Mater. 240, 445 (2002). Development of an all-nitride magnetic tunnel junction.

[152] C. Q. Sun, Prog. Mater. Sci. 48(6), 521 (2003). Oxidation electronics: Bond-band-barrier correlation and its applications.

[153] C. Q. Sun, Phys. Rev. B 69, 045105 (2004). Surface and nanosolid core-level shift: Impact of atomic coordination number imperfection.

[154] Z. Wen, M. Zhao, and Q. Jiang, J. Phys. D.: Cond. Matt. 12, 8819 (2000). The melting temperature of molecular nanocrystals at the lower bound of the mesoscopic size range.

[155] N. F. Mott and W. D. Twose, Adv. Phys. 10, 107 (1961).

---

[156] C. Q. Sun, H. L. Bai, B. K. Tay, S. Li, and E. Y. Jiang, J. Phys. Chem. B 107, 7544 (2003). Dimension, strength, and chemical and thermal stability of a single C-C bond in carbon nanotubes.

[157] C. Q. Sun, Y. Wang, B. K. Tay, S. Li, H. Huang, and Y. Zhang, J. Phys. Chem. B 106, 10701 (2002). Correlation between the melting point of a nanosolid and the cohesive energy of a surface atom.

[158] W. H. Zhong, C. Q. Sun, B. K. Tay, S. Li, H. L. Bai, and E. Y. Jiang, J. Phys.: Condens. Matt. 14, L399 (2002). Curie temperature suppression of ferromagnetic nanosolids.

[159] H. T. Huang, C. Q. Sun, T. S. Zhang, and H. Peter, Phys. Rev. B 63, 184112 (2001). Grain-size effect on ferroelectric Pb(Zr1-xTix)O-3 solid solutions induced by surface bond contraction.

[160] C. Q. Sun, S. Li, B. K. Tay, and T. P. Chen, Acta. Materialia 50, 4687 (2002). Upper limit of blue shift in the photoluminescence of CdSe and CdS nanosolids.

[161] C. Q. Sun, L. K. Pan, H. L. Bai, Z. Q. Li, P. Wu, and E. Y. Jiang, Acta Mater. 51, 4631 (2003). Effects of surface passivation and interfacial reaction on the size-dependent 2p-level shift of supported copper nanosolids.

[162] C. Q. Sun, S. Li, and B. K. Tay, Appl. Phys. Lett. 82, 3568 (2003). Laser-like mechanoluminescence in ZnMnTe-diluted magnetic semiconductor.

[163] C. Q. Sun, B. K. Tay, X. T. Zeng, S. Li, T. P. Chen, H. L. Bai, and E. Y. Jiang, J. Phys.: Condens. Matter 14, 7781 (2002). Bond-order – bond-length – bond-strength correlation mechanism for the shape-and-size dependency of a nanosolid.

[164] P. J. Feibelman, Phys. Rev. B 53, 13740 (1996). Relaxation of hcp(0001) surfaces: A chemical view.

[165] C. Q. Sun, T. P. Chen, B. K. Tay, S. Li, H. Huang, Y. B. Zhang, L. K. Pan, S. P. Lau, and X. W. Sun, J. Phys. D 34, 3470 (2001). An extended quantum confinement theory: Surface-coordination imperfection modifies the entire band structure of a nanosolid.

[166] C. Q. Sun, X. W. Sun, B. K. Tay, S. P. Lau, H. Huang, and S. Li, J. Phys. D 34, 2359 (2001). Dielectric suppression and its effect on photoabsorption of nanometric semiconductors.

[167] C. Q. Sun, H. Q. Gong, P. Hing, and H. T. Ye, Surf. Rev. Lett. 6, L171 (1999). Behind the quantum confinement and surface passivation of nanoclusters.

[168] http://www.sandia.gov/media/NewsRel/NR2000/ising.htm.

[169] J. Crangel, Solid State Magnetism, Van Nostrand Reinhold, New York (1991).

[170] D. Mattis, Theory of Magnetism, Springer-verlag Berlin (1985).

[171] G. Rado and H. Suhl, Eds., Magnetism, Academic Press, New York (1963).

[172] L. Gunther and B. Barbara, Eds., Quantum Tunneling of the Magnetization, Vol. 301, Kluwer Academic, Dordrecht, Boston (1995).

[173] C. Sangregorio, T. Ohm, C. Paulsen, T. Sessoli, and D. Gatteschi, Phys. Rev. Lett. 78, 4645 (1997). Quantum tunneling of the magnetization in an iron cluster nanomagnet.

[174] N. Metropolis, A. Rosenbluth, M. Rosenbluth, A. Teller, and E. Teller, J. Chem. Phys. 21, 1087 (1953). Equation of state calculation by fast computing machines.

[175] W. H. Zhong, C. Q. Sun, S. Li, H.L. Bai, and E.Y. Jiang, “Impact of bond order loss on surface and nanosolid magnetism,” ACTA MATERIALIA, in press (2005).

[176] J. S. Chen, S. P. Lau, Y. B. Zhang, Z. Sun, B. K. Tay, and C. Q. Sun, Thin Solid Films 443, 115 (2003). Deposition of permalloy films by filtered cathodic vacuum arc.

[177] W. H. Zhong, S. P. Lau, B. K. Tay, S. Li, and C. Q. Sun, Proceedings of the Symposium F (ISBN 981-238-372-7), Int. Conf. Mater. Adv. Technol. 251-254 (2003). Iron-nitride thin films deposited using filtered cathodic vacuum arc technique.

[178] W. H. Zhong, B. K. Tay, S. P. Lau, X. W. Sun, S. Li, and C. Q. Sun, *Thin Solid Films,* 478, 61-6 (2005). Structural and magnetic properties of iron-nitride thin films deposited using a filtered cathodic vacuum arc.

[179] D. S. Dai and K. M. Qian, Ferromagnetism, , Science. Press Beijing (2000).

[180] A. J. Freeman, C. L. Fu, S. Ohnish, and M. Weinert, in Polarized Electrons in Surface Physics, R. Feder, Ed., World Scientific, Singapore (1985), pp. 3-66.

[181] X. Qian and W. Hübner, Phys. Rev. B 60, 16192 (1999). First-principles calculation of structural and magnetic properties for Fe monolayers and bilayers on W(110).

[182] C. Q. Sun, B. K. Tay, Y. Q. Fu, S. Li, T. P. Chen, H. L. Bai, and E. Y. Jiang, J. Phys. Chem B. 107, 411 (2003). Discriminating crystal bonding from the atomic trapping of a core electron at energy levels shifted by surface relaxation or nanosolid formation.

[183] M. E. Fisher, S. K. Ma, and B. G. Nickel, Phys. Rev. Lett. 29, 917 (1972). Critical exponents for long-range interactions.

[184] H. E. Stanley, Introduction to Phase Transition and Critical Phenomena, Oxford University Press, New York (1971).

[185] A. Kara and T. S. Rahman, Phys. Rev. Lett. 81, 1453 (1998). Vibrational properties of metallic nanocrystals.

[186] M. Sakurai, K. Watanabe, K. Sumiyama, and K. Suzuki, J. Chem. Phys. 111, 235 (1999). Magic numbers in transition metal (Fe, Ti, Zr, Nb, and Ta) clusters observed by time-of-flight mass spectrometry.

[187] D. Reinhard, Phys. Rev. Lett. 79, 1459 (1997). Size-dependent icosahedral-to-fcc structure change confirmed in unsupported nanometer-sized copper clusters.

[188] W. H. Zhong, C. Q. Sun, and S. Li, Solid State Commu. 130, 603 (2004). Size-effect on the magnetism of nanocrystalline Ni films at room temperature.

[189] G. Bertotti, Hysteresis in Magnetism, Academic Press, San Diego (1998).

[190] Y. Yamamoto, H. Tanaka, and T. Kawai, J. Magn. Magn. Mater. 261, 263 (2003). Appearance of magnetic blocking temperature in zinc magnesium ferrite thin films.

[191] C. Kittel, Phys. Rev. 70, 965 (1946). Theory of the structure of ferromagnetic domains in films and small particles.

[192] J. G. Kim, K. H. Han, S. H. Song, and A. Reilly, Thin Solid Films 440, 54 (2003). Magnetic properties of sputtered soft magnetic Fe-Ni films with a uniaxial anisotropy.

[193] Y. M. Kim, D. Choi, K. H. Kim, J. Kim, S. H. Han, and H. J. Kim, J. Magn. Magn. Mater. 254-255, 419 (2003). Thickness effects on magnetic

properties and ferromagnetic resonance of Co–Ni–Fe soft magnetic thin films.

[194] C. Q. Sun, Appl. Phys. Lett. 72, 1706 (1998). A model of bonding and band-forming for oxides and nitrides.

[195] L. Pauling, The Nature of Chemical Bond. 3rd ed. Cornell University Press, New York (1960).

[196] C. Q. Sun, Mod. Phys. Lett. B 11, 81 (1997). What effects in nature the two-phase on the O-Cu(001)?

[197] C. Q. Sun, Mod. Phys. Lett. B 11, 1115 (1997). Nature of the O-fcc(110) surface-bond networking.

[198] C. Q. Sun. Surf. Sci. Lett. 398, L320 (1998). On the nature of the O-Rh(110) multiphase ordering.

[199] R. Coehoorn, G. H. O. Daalderop, and H. J. F. Jansen, Phys. Rev. B 48, 3830 (1993). Full-potential calculations of the magnetization of $Fe_{16}N_2$ and Fe_4N.

[200] E. J. Miola, S. D. de Soua, P. A. P. Nascente, M. O. Dionysio, C. A. Olivieri, and D. Spinelli, Appl. Surf. Sci. 144-145, 272 (1999). Surface characterisation of plasma-nitrided iron by X-ray photoelectron spectroscopy.

[201] D. L. Cocke, M. J. Rajman, and S. Veprek, J. Electrochem. Soc. 136, 3655 (1989). Surface properties and reactivities of plasma-nitrided iron and their relation to corrosion passivation.

[202] W. Diekmann, G. Panzner, and H. J. Grabke, Surf. Sci. 218, 507 (1989). The bonding state of nitrogen segregated on Fe(100) and on iron nitrides Fe_4N and Fe_2N.

[203] H. Jacobs, D. Rechenbach, and U. Zachwieja, J. Alloy. Compd. 227, 10 (1995). Structure determination of γ-Fe_4N and ε-Fe_3N.

[204] S. P. Lau, X. L. Xu, J. R. Shi, X. Z. Ding, Z. Sun, and B. K. Tay, Mater. Sci. & Eng. B 85, 20 (2001). Dependences of amorphous structure on bias voltage and annealing in silicon-carbon alloys.

[205] J. P. Zhao, X. Wang, Z. Y. Chen, S. Q. Yang, T. S. Shi, and X. H. Liu, J. Phys. D: Appl. Phys. 30, 5 (1997). Overall energy model for preferred growth of TiN films during filtered arc deposition.

[206] M. Takahashi, H. Shoji, M. Abe, H. Komaba, and T. Wakiyama, IEEE Trans. J. Magn. Jap. 6(2), 102 (1991). Soft magnetic properties of Fe-N thin films sputtered in Ar+N_2 plasma.

[207] K. Oda and T. Yoshio, J. Mater. Sci. 25, 2557 (1990). Preparation of Fe-N films by RF sputtering.

[208] S. Iwatsubo, T. Takahashi, and M. Naoe, Thin Solid Films 343-344, 67 (1999). Effect of surface roughness on magnetic properties of Fe films deposited by dual ion beam sputtering.

[209] A. Anders, Phys. Rev. E 55, 969 (1997). Ion charge state distributions of vacuum arc plasmas: The origin of species.

[210] Y. H. Cheng, B. K. Tay, and S. P. Lau, J. Vac. Sci. Technol. A 20(4), 1327 (2002). Substrate bias dependence of the structure and internal stress of TiN films deposited by the filtered cathodic vacuum arc.

[211] K. Ishikawa, K. Yoshikawa, and N. Okada, Phys. Rev. B 37, 5852 (1988). Size effect on the ferroelectric phase transition in $PbTiO_3$ ultrafine particles.

[212] W. L. Zhong, B. Jiang, P. L. Zhang, J. M. Ma, H. M. Cheng, Z. H. Yang, and L. X. Li, J. Phys.: Condens. Matt. 5, 2619 (1993). Phase transition in $PbTiO_3$ ultrafine particles of different sizes.

[213] T. Yu, Z. X. Shen, W. S. Toh, J. M. Xue, and J. Wang, J. Appl. Phys. 94, 618 (2003). Size effect on the ferroelectric phase transition in $SrBi_2Ta_2O_9$ nanoparticles.

[214] A. V. Pogrebnyakov, J. M. Redwing, J. E. Jones, X. X. Xi, S. Y. Xu, L. I. Qi, V. Vaithyanathan, and D. G. Schlom, Appl. Phys. Lett. 82, 4319 (2003). Thickness dependence of the properties of epitaxial MgB_2 thin films grown by hybrid physical-chemical vapor deposition.

[215] A. P. Tsai, N. Chandrasekhar, and K. Chattopadhyay, Appl. Phys. Lett. 75, 1527 (1999). Size effect on the superconducting transition of embedded lead particles in an Al–Cu–V amorphous matrix.

[216] M. G. Cottam, D. R. Tilley, and B. Zeks, J. Phys. C 17, 1793 (1984). Theory of surface modes in ferroelectrics.

[217] W. L. Zhong, Y. G. Wang, P. L. Zhang, and B. D. Qu, Phys. Rev. B 50, 698 (1994). Phenomenological study of the size effect on phase transitions in ferroelectric particles.

[218] B. Jiang and L. A. Bursill, Phys. Rev. B 60, 9978 (1999). Phenomenological theory of size effects in ultrafine ferroelectric particles of lead titanate.

[219] C. L. Wang, Y. Xin, X. S. Wang, and W. L. Zhong, Phys. Rev. B 62, 11423 (2000). Size effects of ferroelectric particles described by the transverse Ising model.

[220] Q. Jiang, X. F. Cui, and M. Zhao, Appl. Phys. A 76, 1 (2002). Size effects on Curie temperature of ferroelectric particles.

[221] B. Muhlschlegel, D. J. Scalapino, and R. Denton, Phys. Rev. B 6, 1767 (1972). Thermodynamic properties of small superconducting particles.

[222] M. Strongin, R. S. Thompson, O. F. Karnmerer, and J. E. Crow, Phys. Rev. B. 1, 1078 (1970). Destruction of superconductivity in disordered near-monolayer films.

[223] R. Coswami, S. Banerjee, K. Chattopadhyay, and A. K. Raychaudhuri, J. Appl. Phys. 73, 2934 (1993). Superconductivity in rapidly quenched metallic systems with nanoscale structure.

[224] F. Braun and J. V. Delft, Phys. Rev. B 59, 9527 (1999). Superconductivity in ultrasmall metallic grains.

[225] K. Uchino, Y. Sadanaga, and T. Hirose, J. Am. Ceram. Soc. 72, 1555 (1989). Dependence of the crystal structure on particle size in barium titanate.

[226] S. Chattopadhay, P. Ayyub, V. R. Palkar, A. V. Gurjar, R. M. Wankar, and M. Multani, J. Phys.: Condens. Matt. 9, 8135 (1997). Finite-size effects in antiferroelectric PbZrO/sub 3/nanoparticles.

[227] S. Li, T. While, and C. Q. Sun, Communicated.

[228] S. Schlag, H. F. Eicke, and W. B. Stern, Ferroelectrics 173, 351 (1995). Size driven phase transition and thermodynamic properties of nanocrystalline $BaTiO_3$.

Appendix I

C language program of Monte Carlo simulation

```
/*
  ising.c
  Monte Carlo simulation of the 3-D Ising model of magnetic materials
*/

#include <stdio.h>
#include <stdlib.h>
#include <math.h>
#include <string.h>
#include <ctype.h>

#include "RanGen.h"

#define  L_MAX  80

int D;                                  /*Number of spins in one direction,
                                        diameter of the particle */
int N = 0;                              /* total number of spins  */
int layernumber=20;                     /* global variable, layer number is
                                        determined by the shell number */


int spin[L_MAX][L_MAX][L_MAX];
                                        /* spin values */
                                        /* The value is 0,-1,or 1. 0 indicates that
                                        there is no atom in the sites, -1 means the
                                        spin down, and 1 means spin up
                                        */

int S=6;                                /*shell number of the system*/
int diametersquare[L_MAX*L_MAX];

                                        /*The square of the radius of the system
                                        with every shell number */

double radia[L_MAX][L_MAX][L_MAX];
                                        /*To store the radius of each atoms */

int center=0;                           /* the center of the particle:
(center,center,center)*/

int next[L_MAX], prev[L_MAX];
int Neighbors[13];
                                        /* Indices of neighbors with periodic */

double J = 1.0;                         /* coupling +1=ferro, -1=antiferro */
double T = 2.4;                         /* temperature */

double w[49][3];                        /* pre-computed Boltzmann factors */

int SS;                                 /* sum of s_i*s_j */
double E;                               /* current energy */
double M;                               /* current magnetization */

int MonteCarloSteps;                    /* number of Monte Carlo steps per spin
*/
```

```
int flips;                                      /* spin flips in current sweep of lattice */

unsigned long randomSeed = 200;


int hotStart = 0;
double H = 1.2;                                 /* applied magnetic field */


int thermalizationSteps = 5000;
int productionSteps = 5000;
int stepsPerBlock = 500;
int blocks;

int measurements;
double E_sum, E_sqd_sum, M_sum, M_sqd_sum, abs_M_sum, acceptance_sum;
double E_block, E_block_sum, E_block_sqd_sum;

void calculateDofshell(void);
void printBoltzmannFactors(FILE *file);
void printDofshell(FILE *file);
void computeBoltzmannFactors(void);
void particleestablish (void);
void printparticle (FILE *file);
void initialize(FILE *file);
void measureProperties(void);
void oneMonteCarloStep(FILE *file);
void printHeader(FILE *file);
void printProperties(FILE *file);
void printBlockProperties(FILE *file);
void zeroProperties(void);

int main (int argc, char *argv[]) {
    int i, step, block,TT,HH;
            FILE *fp;

    for (i = 1; i < argc; i++) {
             if (strchr(argv[i], '='))
                switch (toupper(*argv[i])) {
                case 'S':
                         sscanf(argv[i] + 2, "%d", &S);
                         break;
                case 'T':
                         sscanf(argv[i] + 2, "%lf", &T);
                         break;
                default:
                         break;
                }
    }
             fp=fopen("Formal-TSH.txt","w");
                                                /* file for output */
             calculateDofshell();
             printDofshell(fp);
             fprintf(fp,"Monte Carlo Simulation of the 3-D Ising Model\n");

           fprintf(fp,"========================================================
           =====\n");
           fprintf(fp,"Temperature| shell |   N  |   H       |        | (|M|/N)  |  (E/N)   |      Sus/N  |
           (C/N)   |accept ratio|\n");
```

```
        for (S=2; S<6; S++)
                {
                        for (TT=0; TT<16; TT+=2)
                                {
                                 for (HH=0;HH<=0;HH++)
                                        {
                                         H=HH/10.0;
                                         if (TT==0)
                                         T=TT+0.1;
                                         else T=TT;

                                         if (T<6)
                                                 hotStart=0;
                                         else
                                                 hotStart=1;

                                         layernumber=(int)(sqrt(diametersquare[S]))+1;
                                         fprintf(fp,"  %6.2f   %5d    ",T,S);
                                           /*output the temperature and the shell number of
                                           the particle*/

                                         N=0;
                                         particleestablish();

                                         initialize(fp);

                                         printparticle(fp);

                                         fprintf(fp,"  %d  ", N);
                                         /*output the total spin number of the particle*/

                                         fprintf(fp," %f  ", H);
                                         /*output the applied magnetic field*/

                                        printf("\nPerforming %d thermalization steps ...",
                                        thermalizationSteps);

                                         printBoltzmannFactors(fp);

                                  for (step = 0; step < thermalizationSteps; step++)
                                        oneMonteCarloStep(fp);
                                                                              }
                                  printf(" done thermalization steps\n");
                                  zeroProperties();
                                  printf("Performing %d production steps\n",
productionSteps);

                                         /*printHeader(fp);*/

                                         for (step = 0; step < productionSteps; step++)
                                         {
                                          oneMonteCarloStep(fp);
                                          measureProperties();
                                          if (MonteCarloSteps % 500 = = 0)
                                         printProperties(stdout);
                                         }
                                         printProperties(fp);
                                         /*fprintf(fp,"\n");*/
                                         zeroProperties;
                                         printBlockProperties(stdout);
```

```
                                        }/*end of for*/

                                } /*end of for*/
                        }/*end of for*/

                fclose(fp);

    return 0;
}

void computeBoltzmannFactors (void)
{
    int i;

    for (i = -24; i <= 24; i += 2)
   {
              w[i + 24][0] = exp( - (i*J + 2 * H) / T);
              w[i + 24][2] = exp( - (i*J - 2 * H) / T);
    }
}


void printBoltzmannFactors(FILE *file)
{
            int i;
            for (i = 0; i <= 48; i += 4)
                        fprintf(file, "SumOfNeighbors: %d,  BoltzmannFactors: %9.6f\n", (i-24)/2,
w[i][0]);
            for (i = 0; i <= 48; i += 4)
                        fprintf(file, "Index: %d, SumOfNeighbors: %d,  BoltzmannFactors: %9.6f\n",
                        i, (i-24)/2, w[i][2]);
}


void particleestablish (void)
{

            int i,j,k;

            D=2*layernumber+3;

            /* D should be always smaller than L_MAX */

            for (i=0;i<L_MAX;i++)
                        for (j=0;j<L_MAX;j++)
                                    for (k=0;k<L_MAX;k++)
                                                spin[i][j][k]=0;


            for (i=0;i<=layernumber;i++)
                        for (j=0;j<=layernumber;j++)
                                    for (k=0;k<=layernumber;k++)
                                                {
                                                            spin[i+i][j+j][k+k]=1;
                                                            spin[2*i+1][2*j+1][2*k]=1;
                                                            spin[2*i+1][2*j][2*k+1]=1;
                                                            spin[2*i][2*j+1][2*k+1]=1;
                                                }
```

```
            if (spin[layernumber][layernumber][layernumber]= =0)
                        center=layernumber+1;
            else
                        center=layernumber;

            for (i=0;i<=D+2;i++)
                        for (j=0;j<=D+2;j++)
                                    for (k=0;k<=D+2;k++)
                                                if (spin[i][j][k]!=0)
                                                            {if (((i-center)*(i-center)+(j-center)*(j-center)
                                                              +(k-center)*(k-center))>diametersquare[S])
                                                                        spin[i][j][k]=0;
                                                            else
                                                                        N++;
                                                            }


}


void initialize ( FILE *file)
{
    int i, x, y, z;

   qad_init(1,randomSeed);

    if (hotStart)
             {
              for (x = 0; x <= D; x++)
                        for (y = 0; y <= D; y++)
                                    for (z = 0; z <= D; z++)
                                                {
                                                if (spin[x][y][z] != 0)
                                                            {   /*fprintf (file,"flag1");*/
                                                                        if (qad_rand(0)<0.5)
                                                                                {
                                                                                spin[x][y][z] = 1;
                                                                                /*fprintf(file,"%10.5f\n",
qad_rand(0));*/}
                                                                                else spin[x][y][z] = -1;
                                                                                }
                                                            }
                                                }
 else
            {
             for (x = 0; x <= D; x++)
                         for (y = 0; y <= D; y++)
                                    for (z = 0; z <= D; z++)
                                                if (spin[x][y][z] != 0)
                                                            {
                                                             if (J < 0 && (x + y + z) % 3)
                                                                     spin[x][y][z] = -1;
                                                             else
                                                                        spin[x][y][z] = 1;
                                                            }
            }

    /* arrays for periodic boundary conditions */
    for (i = 0; i <= D; i++)
   {
```

```
             next[i] = i + 1;
             prev[i] = i - 1;
    }

 /*
    next[D - 1] = 0;
    prev[0] = D - 1;
*/

    /* compute spin sums */
    M = SS = 0;
    for (x = 0; x <= D; x++)
             for (y = 0; y <= D; y++)
                         for (z = 0; z <= D; z++)
                                   {
                                      if (spin[x][y][z] != 0)
                                      {
                                                M += spin[x][y][z];
                                                    Neighbors[1]=spin[2*center-x][2*center-y][z];

                                                            Neighbors[2]=spin[x][2*center-y][2*center-z];

                                                            Neighbors[3]=spin[2*center-x][y][2*center-z];

                                                            Neighbors[4]=spin[x][y][2*center-z];

                                                            Neighbors[5]=spin[2*center-x][y][z];

                                                            Neighbors[6]=spin[x][2*center-y][z];

                                                  SS +=
                                                  spin[x][y][z]*(Neighbors[1]+Neighbors[2]+Neighbors[3]
                                                  +Neighbors[4]+Neighbors[5]+Neighbors[6]);


                                                }
                                   }
    E = - J * SS - H * M;

    computeBoltzmannFactors();

    MonteCarloSteps = 0;
}

void oneMonteCarloStep (FILE *file)
{
    int x, y,z, sum_of_neighbors, delta_SS;
    double ratio_of_Boltzmann_factors,temp;

    flips = 0;
    delta_SS=0;
    /* sweep the lattice */
    for (x = 0; x <= D; x++)

             for (y = 0; y <= D; y++)

                         for (z=0; z <= D; z++)
                                    if (spin[x][y][z]!=0)
                                    {
                                                            Neighbors[1]=spin[2*center-x][2*center-y][z];
```

```
                                        Neighbors[2]=spin[x][2*center-y][2*center-z];

                                        Neighbors[3]=spin[2*center-x][y][2*center-z];

                                        Neighbors[4]=spin[x][y][2*center-z];

                                        Neighbors[5]=spin[2*center-x][y][z];

                                        Neighbors[6]=spin[x][2*center-y][z];

                                        Neighbors[7]=spin[x][y][2*center-z];

                                        Neighbors[8]=spin[2*center-x][y][z];

                                        Neighbors[9]=spin[x][2*center-y][z];

                                        Neighbors[10]=spin[x][2*center-y][2*center-z];

                                        Neighbors[11]=spin[2*center-x][y][2*center-z];

                                        Neighbors[12]=spin[2*center-x][2*center-y][z];


                                 sum_of_neighbors=
                                 Neighbors[1]+Neighbors[2]+Neighbors[3]+Neighbors[4]+
                                 Neighbors[5]+Neighbors[6]+Neighbors[7]+Neighbors[8]+
                                 Neighbors[9]+Neighbors[10]+Neighbors[11]+Neighbors[1
                                 2];

                                  delta_SS = 2*spin[x][y][z] * sum_of_neighbors;
                                  ratio_of_Boltzmann_factors = w[delta_SS +
24][spin[x][y][z] + 1];

                                  if ((temp=qad_rand(0)) < ratio_of_Boltzmann_factors)
                                        {
                                              spin[x][y][z] = -spin[x][y][z];
                                              M +=2*spin[x][y][z];
                                              SS -= delta_SS;
                                              ++flips;

                                        }
                         }

  E = - J * SS - H * M;
  ++MonteCarloSteps;
}

void zeroProperties (void)
{
  E_sum = E_sqd_sum = M_sum = M_sqd_sum = abs_M_sum = 0;
  E_block = E_block_sum = E_block_sqd_sum = 0;
  acceptance_sum = 0;
  measurements = 0;
  blocks = 0;
}

void measureProperties (void)
{
  M_sum += M;
  M_sqd_sum += M * M;
```

```
    abs_M_sum += fabs(M);
    E_sum += E;
    E_sqd_sum += E * E;
    acceptance_sum += flips;
    ++measurements;

    if (MonteCarloSteps % stepsPerBlock == 0) {
            double avg = E_block / stepsPerBlock;
            E_block_sum += avg;
            E_block_sqd_sum += avg * avg;
            ++blocks;
            E_block = 0;
    } else {
            E_block += E;
    }
}

void printHeader (FILE *file) {
    int i;
    fprintf(file, "   MC Step ");
    fprintf(file, "    |M| /N  ");
    fprintf(file, "     E /N   ");
    fprintf(file, "    Sus/N   ");
    fprintf(file, "    C /N    ");
    fprintf(file, "   accept ratio\n");
    for (i = 0; i < 6; i++)
            fprintf(file, "-----------");
    fprintf(file, "\n");
}

void printProperties (FILE *file) {
    double norm, avg;

    /* measurement number */
    fprintf(file, "  % 8d  ", measurements);
    norm = N;
    if (measurements > 0)
            norm *= measurements;
    /* average |magnetization| per spin */
    fprintf(file, "% 9.6f  ", abs_M_sum / norm);
    /* average energy per spin*/
    fprintf(file, "% 9.6f  ", E_sum / norm);
    /* average susceptibility per spin */
    avg = M_sum / norm;
    avg = (M_sqd_sum / norm - N * avg * avg) / T;
    fprintf(file, "% 9.6f  ", avg);
    /* average heat capacity per spin */
    avg = E_sum / norm;
    avg = (E_sqd_sum / norm - N * avg * avg) / (T * T);
    fprintf(file, "% 9.6f  ", avg);
    /* average acceptance ratio */
    fprintf(file, "% 9.6f\n", acceptance_sum / norm);


   /*fprintf(file, "norm:%5d,N:%5d,M:%5d\n",norm,N,M);*/

            /*================================================*
            fprintf(file, "\n absM_sum: % 9d  norm: % 9d   N:% 9d\n", abs_M_sum, norm, N);
            /*================================================*/
}
```

```
void printBlockProperties (FILE *file)
{
    double avg, std_dev;

    avg = E_sum / measurements;
    std_dev = E_sqd_sum /measurements;
    std_dev = sqrt(std_dev - avg * avg);
    avg /= N;
    std_dev /= N;
    fprintf(file,"printblockproperties\n");
    fprintf(file," = %f +- %f\n", avg, std_dev / sqrt(measurements));
    avg = E_block_sum / blocks;
    std_dev = E_block_sqd_sum / blocks;
    std_dev = sqrt(std_dev - avg * avg);
    avg /= N;
    std_dev /= N;
    fprintf(file,"Number of blocks = %d\n", blocks);
    fprintf(file," = %f +- %f\n", avg, std_dev / sqrt(blocks));

}


void printparticle (FILE *file)
{
            int x,y,z;
            fprintf(file, "spin system of the particle:\n");
            for (x=0;x<=D;x++)
                        {
                        fprintf(file, "section %6d\n",x);
                        for (y=0;y<=D;y++)
                                    {
                                    for (z=0;z<=D;z++)
                                                fprintf(file, "%3d",spin[x][y][z]);
                                    fprintf(file,"\n");
                           }

                        }
}


void calculateDofshell (void)
{
            int i,j,k,x,y,z,LMAXLMAX,shellnumber;
            short int sp[L_MAX][L_MAX][L_MAX];

            for (i=0;i<L_MAX;i++)
                        for (j=0;j<L_MAX;j++)
                                    for (k=0;k<L_MAX;k++)
                                                sp[i][j][k]=0;

            for (i=0;i<L_MAX/2-1;i++)
                        for (j=0;j<L_MAX/2-1;j++)
                                    for (k=0;k<L_MAX/2-1;k++)
                                                {
                                                            sp[i+i][j+j][k+k]=1;
                                                            sp[2*i+1][2*j+1][2*k]=-1;
                                                            sp[2*i+1][2*j][2*k+1]=-1;
                                                            sp[2*i][2*j+1][2*k+1]=-1;
                                                }
```

```
            LMAXLMAX=L_MAX*L_MAX;
            shellnumber=1;


            for (x=1;x<LMAXLMAX;x++)
                        {
                                    y=0;
                                    for (i=0;(i<L_MAX-1)&&(y==0);i++)
                                                for (j=0;(j<L_MAX-1)&&(y==0);j++)
                                                            for (k=0;(k<L_MAX-1)&&(y==0);k++)
                                                                        if (sp[i][j][k]!=0)
                                                                        {
                                                                        z=i*i+j*j+k*k;
                                                                        if (z==x)
                                                                                    y=1;
                                                                        }

                                    if (y==1)
                                                {
                                                shellnumber++;
                                                diametersquare[shellnumber]=z;
                                                }
                        }
            }/*there is an atom in the center in this situation */


void printDofshell (FILE *file)
{
            int i,LMAXLMAX;
            double d;
            LMAXLMAX=L_MAX*L_MAX;
            fprintf(file, "the shell diameter of each shell:");
            for (i=0;i<L_MAX;i++)
                        {
                                    d=sqrt(diametersquare[i]);
                                    fprintf(file, "%4d:%8.4f  ", i, d);
                                    if (i%5==0)
                                                fprintf(file,"\n");
                        }
}


/* RanGen.h
 * Quick And Dirty Random Number Generator
 * Based on the quick and dirty generator in "Numerical Recipes"
 * Parallelized using a simple leapfrog algorithm
 */

#ifndef _QADRNG_H_
#define _QADRNG_H_ 1

#include <stdio.h>
#include <stdlib.h>

#define QAD_MODULUS      4294967296.0
#define QAD_MULTIPLIER   1664525L
#define QAD_INCREMENT    1013904223L
#define QAD_MAX_PROCS    256

static unsigned long qad_seed[QAD_MAX_PROCS];
```

```
static unsigned long qad_mult;
static unsigned long qad_incr;
static int qad_procs = 1;

static void qad_init (int processes, unsigned long seed)
{
   int i;

   if (processes < 1 || processes > QAD_MAX_PROCS)
       {
             fprintf(stderr, "qad_init: numprocs = %d ", processes);
             fprintf(stderr, " must be in range [1, %d]\n", QAD_MAX_PROCS);
             exit(1);
       }
  else qad_procs = processes;

  for (i = 0; i < processes; i++)
       {
           qad_seed[i] = seed;
           seed = QAD_MULTIPLIER * seed + QAD_INCREMENT;
       }

   qad_mult = QAD_MULTIPLIER;
   qad_incr = QAD_INCREMENT;
   for (i = 1; i < processes; i++)
           qad_mult *= QAD_MULTIPLIER;
   qad_incr = QAD_INCREMENT * (qad_mult - 1) / (QAD_MULTIPLIER - 1);
}

static unsigned long qad_get_seed (void)
{
   return qad_seed[0];
}

static double qad_rand (int process)
{
   qad_seed[process] = qad_mult * qad_seed[process] + qad_incr;
   return qad_seed[process] / QAD_MODULUS;
}

#define QAD_RAND(process) \
   ( (qad_seed[(process)] = \
      qad_mult * qad_seed[(process)] + qad_incr ) / QAD_MODULUS )

#endif /* _QADRNG_H_ */



/*END*/
```

Appendix II

C language program for the calculation of long-range exchange energy loss

```
#include <stdio.h>
#include <stdlib.h>
#include <math.h>
#include <string.h>
#include <ctype.h>

int main ()
{
        int i, ShellNumber, RangeOfExchange, K;
        double DeltaShift, VOfLost, Shift, SToVRatio;
        double s, sinr, cosr, h1, V1, V2,R,d,r;

        FILE *fp;
        fp=fopen("tempout.txt","w");

        //initialize:
        RangeOfExchange=100;

        for (ShellNumber=1; ShellNumber<=400; ShellNumber++)
        {
        //ShellNumber=50;
        Shift=0;
        for (i=1; i<=RangeOfExchange; i++)
        {
                if ((K=ShellNumber-i)<=0)
                        break;
                else
                {
                        //calculate one shell
                        SToVRatio=3.0/ShellNumber*(1-(i-0.5)/ShellNumber)*(1-(i-
                                    0.5)/ShellNumber);

                        //calculate the lost volume ratio of exchange
                        R=ShellNumber;
                        d=K;
                        r=RangeOfExchange;

                        s=(R+d+r)/2;
                        sinr=sqrt(s*(s-R)*(s-d)*(s-r))/(R*d/2);
                        cosr=sqrt(1-sinr*sinr);
                        h1=R-R*cosr;
                        V1=3.14*h1*h1*(R-h1/3);
                        V2=3.14*(r+d-R*cosr)*(r+d-R*cosr)*(r-(r+d-R*cosr)/3);
                        VOfLost=(V2-V1)/(4*3.14*r*r*r/3);

                        DeltaShift=SToVRatio*(-VOfLost);

                        Shift=Shift+DeltaShift;

                }
        }
        fprintf(fp,"  %d    %f\n", ShellNumber,Shift*100);
```

```
            }

            fclose(fp);
   return 0;
}
```